Design of a mechatronic system for postural control analysis

Doctoral Dissertation
Doctoral Program in Mechanical Engineering (32° cycle)

Design of a mechatronic system for postural control analysis

Carlo De Benedictis

* * * * * *

Supervisor
Prof. Carlo Ferraresi

Politecnico di Torino
May 20, 2020

I hereby declare that, the contents and organisation of this dissertation constitute my own original work and does not compromise in any way the rights of third parties, including those relating to the security of personal data.

Carlo De Benedictis
Turin, May 20, 2020

Summary

Balance control is necessary to perform any basic activity in every day life. With aging, the skill of a person to keep balance is altered and can lead to serious hazards especially for elderly people, since falls represents the second leading cause of injury deaths worldwide. To assess the ability of a patient to keep or regain balance, posturographic analyses are performed in many clinical environments by skilled operators. A posturographic clinical test can be performed in a static (unperturbed) or in a dynamic (perturbed) condition. The definition of such perturbation is related to the desired outcome of the specific test to perform. For instance, recovery mechanisms are far more evident if a mechanical perturbation is exerted on the body of the subject. On the other hand, elderly people with a compromised physical condition might be not eligible for a test in perturbed condition. The multiplicity of solutions available regarding perturbation systems and of methodologies for the interpretation of postural responses represents the main reason for the lack of standard procedures in dynamic posturography. The possibility to exert different mechanical perturbations to the body of the subject, e.g. by shifting the base of support or directly applying pulling or pushing forces, leads to the wide scenario of solutions available. The selection of the mechanical interaction and of amplitude, direction, point of application of the stimuli represents the foundation for the design of any postural analysis systems. The aim of these systems is to identify significant correlations between single or multiple perturbations and the entity of the responses.

This work has the objective to present a novel system for postural perturbation, able to exert force stimuli directly to the body of a subject with predefined waveform, amplitude and duration. This perturbation must be scalable and adaptable. The former refers to the possibility to vary its amplitude in order to evoke responses with different entity. The scalability is also necessary to allow for testing subjects with different constitution and health conditions. Adaptability refers to the opportunity to select different points of application and directions of the stimuli. This feature is relevant to guarantee the unpredictability of perturbations. To improve usability, the perturbation device should be directly maneuvered by the operator by means of appropriate handles. The perturbation system must be eventually expandable to provide multiple stimuli at the same time. This feature

can be comfortably achieved by design of simple perturbation devices, based on low cost and compact architectures, which can be eventually replicated and coordinated to perform simultaneously. Several prototypes of perturbation devices have been tested, and an experimental test-bench for the evaluation of different components and control solutions has been designed. An analytical model of the system has been developed and validated by trials performed in laboratory. The system, in its final architecture, has shown good accuracy and repeatability with high dynamics. The devices have been tested on different samples of healthy subjects, showing a relevant correlation between the impulse (time integral) of the contact force and the Center of Pressure displacement over the base of support that had not been reported earlier in the literature. The relationship between perturbation and response data has been discussed also by means of analytical modeling of postural control, that includes single and two-links inverted pendulum models as well as frequency domain techniques.

Contents

List of Tables

List of Figures

Chapter 1

Introduction

The control of balance in humans is a fundamental functionality which is necessary to perform any basic activity in every day life. This process is rather complex, since it involves many sensory inputs, brain activity and it is influenced relevantly from external factors. With aging, the skill of a human being to keep balance is altered and can lead to serious hazards for the person. Nowadays, the risk of falling in elderly people cannot be neglected, since falls are the second leading cause of injury deaths worldwide, as stated by the World Health Organization in 2018 [1]. Among prevention strategies, it is relevant to understand the basic principles of human balance control and to develop experimental techniques able to estimate the risk of falling of patients. In the following sections, the methodologies used by clinician and researchers to tackle this problem are presented and discussed.

1.1 Posturography

To assess the ability of a patient to keep or regain balance when subjected to an external perturbation, posturographic analyses are performed in many clinical environments by skilled operators, e.g. physiotherapists. These analyses are focused on the identification of patients with increased risk of falling, but they are also aimed to document the effects of a therapy as well as to provide a deep understanding of the mechanisms leading to several postural disorders. In that case, the patient is often dealing with neurological diseases related to stroke or congenital causes.

A clinical test in posturography (stabilometry) can be performed in a static (unperturbed) or in a dynamic (perturbed) condition. Of course, the definition of such perturbation, if any, is related to the desired outcome of the specific test to perform. For instance, recovery mechanisms are far more evident if a mechanical perturbation is exerted on the body of the subject. On the other hand, elderly people with a compromised physical situation might be not eligible for a test in perturbed condition. However, dynamic posturography is frequently needed when

the clinician wants to assess the ability of a subject to maintain balance. In such framework, the safety of the patient must be considered to avoid any dangerous situation. Most applications involve short lasting and unexpected perturbations [2, 3], in order to evaluate the postural reaction occurring briefly after the perturbation, but some studies also present periodic (or quasi-periodic) perturbations to evaluate other physiological mechanisms, such as adaptation [4]. In clinics, as well as in the research literature, several methodologies for postural control analysis are discussed, and they will be presented in the next section. Among the forms of interaction available, this dissertation will only focus on mechanical perturbations thus neglecting visual, auditive and electrical stimuli. In such condition, any additional disturbance exerted on the subject is considered noise from the environment.

1.1.1 Methodologies for dynamic posture analysis

A dynamic stabilometry analysis involves a perturbation system, able to exert a certain number of stimuli to the patient, and a response acquisition and analysis system, dedicated to the measurement and interpretation of the body response after the occurrence of the perturbation. Since several embodiments of such systems exist, an actual standardization of clinical procedures dealing with posture assessment is still lacking and represents one of the driving factors of the research activity presented in this dissertation.

Most of the systems for dynamic posturography presented in the literature or available on the market (e.g. NeuroCom® EquiTest system, Natus Newborn Care, Fig. 1.1) implement a movable platform device as the perturbation system. This platform, acting as the Base of Support (BoS) of the standing subject, is shifted in one or more directions with a selected reference of displacement, velocity or acceleration, in order to exert the desired perturbation to the body of the subject [2, 3, 5, 6, 7]. Therefore, in such systems, the mechanical stimulus is not provided by straightforward application of a force to the body of the subject, which would represent the most direct form of mechanical interaction between the perturbation device and the patient. Nonetheless, this methodology is currently one of the most frequently selected by the clinicians and researchers, mainly due to the ease of regulating the motion of the BoS with common linear actuators with respect to the control of the contact force exerted by a perturbation device on the body of the subject. In other embodiments, the movement of the platform is conveyed by robotic systems such as Stewart platforms [8], allowing for complex 6 Degrees of Freedom (DoF) motion. In some works, the BoS is not shifting but there are obstacles placed on the path that disturb the normal walking of the subject [9, 10]. This method is rather different from the one presented above, since it involves walking rather than static stance condition for the subject. Therefore, this kind of perturbation might be not appropriate for people with relevant deficiencies in walking. Moreover, such perturbation cannot be easily customized and adapted to

Figure 1.1: NeuroCom® EquiTest system, Natus Newborn Care.

the specific subject since the clinician does not have the possibility to effectively control the magnitude and duration of the stimulation.

A third way to design a perturbation is given by the application of a force stimulus directly to the body of the subject, e.g. by pushing or pulling. With respect to the shifting BoS solution, this methodology theoretically allows for less limitations in the choice of direction, magnitude and waveform of the perturbation but it is subjected to additional difficulties regarding the accurate control of the stimulation, especially when sudden perturbations are considered. Few studies showed applications considering this kind of perturbation method, such as the ones based on pendulum-like structures used to impact the body of the patient [2, 11, 12] or on systems using cables and pulleys [13, 14, 15] to exert a traction force on a specific body part, in general trunk or hands (see Fig. 1.2). For both kinds of perturbation system, the magnitude of the stimulus depends on the physical characteristics of the perturbation device: in former studies, it depends on the mass or initial position of the pendulum, whereas in the latter it is related, for instance, to the mass of a suspended weight linked to the subject's body through a cable. In such systems, a preloading device may be included to regulate the initial trunk positioning during a trial [16]. However, these solutions lack the possibility to easily vary the amplitude, as well as the duration or time course, of the disturbance. To overcome such limitations, a possible solution could be represented by a closed-loop feedback system, able to perform the monitoring and real time control of the contact force. This solution presents many difficulties regarding the regulation of the interaction force, typical of mechatronic systems dealing with biological structures such as the human

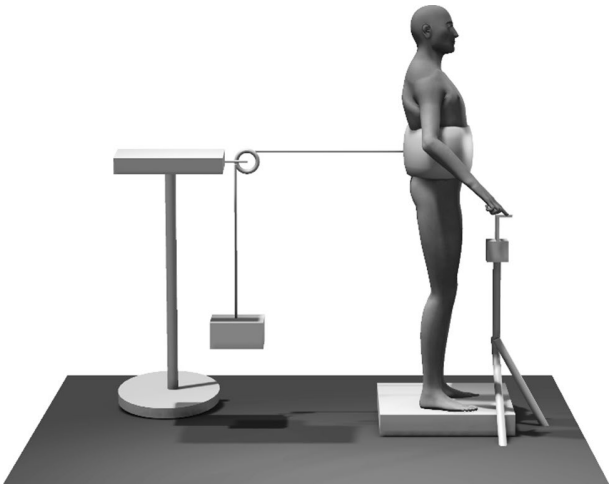

Figure 1.2: Perturbation system based on pulling [14].

body. A work presented by Boonstra TA et al. [17] shows a system combining a shifting platform and a "pusher" for antero-posterior perturbations, able to generate torques about the ankle joint (magnitude lower than 50 Nm). In that study the perturbation was described as a multi-sine force, even though the Authors did not provide any details on the actual control of the contact force. Similar solutions have been presented in the literature [7, 18], where a pseudorandom ternary sequence (PRTS, [19]) has been used. In all of these works, the disturbance (as a force or a BoS displacement) is not designed as a short lasting perturbation, rather it is applied for several seconds to the patient. For this reason, a system similar to the one presented above [17] might not be appropriate to investigate the postural reaction to sudden perturbations, which represent the main focus of this study. Sudden perturbations were instead considered in [20], in which the operator provided small magnitude pushes (less than 30 N) to the back of the subject. However, the contact force was not controlled at all, therefore it depended only on the skill of the operator. In [21] a pendulum-like structure as the one presented in [2, 11] has been used not to impact the subject, but to be handled and pushed by the patient in order to investigate the ability of elderly people to keep balance in pushing tasks. However, similarly to the aforementioned applications, the Authors in [21] do not perform any control of the magnitude or of duration of the disturbance.

Although the design of the perturbation device is critical in a system for dynamic posturographic analysis, the interpretation of the human body response, which has to be recorded through appropriate systems of transducers, is equally fundamental. Generally speaking, it involves finding some consistent and significant relationship between the measured response and the entity of the stimulation. In the following, the main types of response measurement systems shared by most of posturographic devices are briefly described.

1.1.2 Measurement of the postural response

The measurement of the response can be performed with several instruments, depending on the aspects that clinicians choose to focus on. Three main fields of analysis can be identified: kinetics, kinematics and electromyography (see Fig. 1.3).

Figure 1.3: Postural response measurement systems: (a) kinetic; (b) kinematic; (c) electromyography.

Kinetic measurements involve the use of force plates, instrumented insoles, treadmills or baropodometric platforms (Fig.1.3a). Therefore, they enable to measure the position of the Center of Pressure (CoP) on the BoS, the distribution of pressures on the soles, the ground reaction force and torque components. The latter are useful to perform an inverse dynamics calculation, which also requires information about body kinematics. CoP measurements are probably the most common in studies regarding postural analysis, both in static [22, 23] and in dynamic condition [2, 5, 15, 21, 24].

Kinematic measures are generally performed by motion capture (stereophotogrammetry) which still represents the golden standard for such measurements [8, 17]. However, other solutions are nowadays available, such as low cost scanners (e.g. Microsoft Kinect) or Inertial Measurement Units (IMUs), that is wearable sensors equipped with accelerometers and gyroscopes. Such sensors can be really effective in the assessment of human kinematics during balance analysis trials [25, 26, 27, 28], since they can be implemented without the need for costly laboratories dedicated to human motion analysis. These instruments allow the measurement of segments' linear and angular motion, of joints' rotations, of body sway or Center of

Mass (CoM) displacement. For instance, the studies reported in [29] about the use of wearable sensors to assess postural stability in people with Parkinson's disease, show that inertial sensors, 3D accelerometers and gyroscopes can be effectively used to collect parameters such as body mean acceleration and RMS acceleration in antero-posterior and medio-lateral directions, length of sway, sway velocity, step and stride variability and many other variables regarding human motion, both in quiet stance and during gait. As presented above, such kinematic data are fundamental to perform the inverse dynamics calculation, hence to calculate forces and torques at each joint.

The third kind of postural response measurement deals with electromyography (EMG), thus with the direct measuring of the muscle activity of the patient. This process can be performed with electrodes placed on the skin (surface EMG, sEMG) or with needle electrodes, which are far more invasive but allow for better quality of the EMG signal. Nevertheless, the first solution is typically considered more acceptable than the second one. EMG has been used to evaluate reciprocal activation and co-activation of muscles belonging to trunk and low limb segments [2, 21] by calculation of indexes based on the integral of EMG signal over time. Normalization of EMG signals is generally performed by evaluation of muscle activity in quiet standing. To improve the quality of sEMG signals, skin is generally shaved and abraded before any experimentation, however it is not easy to get always the same level of quality in each subject because of different constitution, sweat and different positioning of the electrodes. Monitoring of muscle activity can be relevant to evaluate reflexive response latency too [16, 24].

1.1.3 Interpretation of the response

Given the possibility to measure and gather data about the postural response of the subject, some kind of interpretation of these data is fundamental to understand the underlying physiological mechanisms. In traditional clinical practice, the clinician usually performs a visual inspection of the subject by qualitatively checking his or her posture and estimating the latency between the occurrence of the perturbation and the complete regain of equilibrium. Instrumental data can be used to measure accurately any parameter relevant to postural control: for instance, CoP displacement [23] or EMG signal onset time [21] can be used to assess the duration of the postural response. Such physical quantities, then, must be interpreted and put in correlation with the characteristics of the perturbation to finally assess the quality of postural control system in a subject.

To improve the understanding of the measured response, models of the human postural control system have been developed and are currently studied by many researchers in the fields of rehabilitation, neurology and physiology. Of course, these models can be rather complex since so it is the balance control. The control of posture is a continuous and dynamic process involving many input channels:

eyes, inner ear, sensory receptors, tactile perception provide significant information about the current state of the subject and his or her positioning with respect to the surrounding environment. These data are collected by the Central Nervous System (CNS) which performs the sensorimotor integration, a process needed to generate the motor response. The latter, handled by the musculoskeletal system, represents the output of the balancing process, since it affects the current posture by means of correcting movements of the subject, but it also is responsible for generating new inputs to the sensors placed all over the human body, e.g. Golgi tendon organ, a proprioceptive sensor located at the insertion of skeletal muscle fibers in tendons. Therefore, posture is continuously adjusted by means of neuromuscular activity. However, in both static condition and when an external perturbation is exerted on the body of the subject, there is not only an active (muscular) response involved to keep balance, but also a passive response acting simultaneously. This mechanism is related to the mechanical impedance of the subject body, including the overall mass and the visco-elasticity of human tissues, bones, muscles and joints. Passive response is immediately evoked by the perturbation. On the contrary, active response presents a latency of the order of 100 ms producing the delayed activation of muscles. The combination of the two responses acting in parallel results in the postural response. A general scheme of postural control system when external perturbations are exerted on the body of a subject is presented in Fig. 1.4. In this picture, feed-forward control mechanism is also shown. This part of postural control deals with pre-defined ways to react that are implemented by CNS and that are modulated by knowledge rather than error (as in feedback control path).

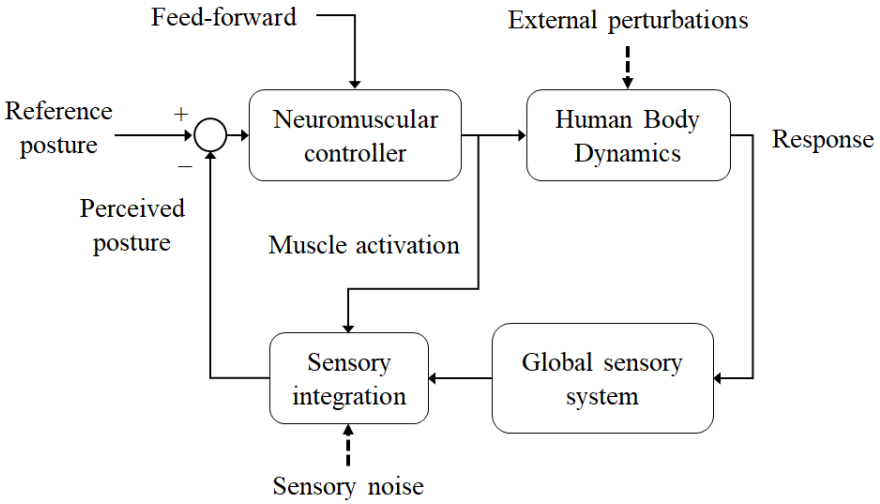

Figure 1.4: Postural control system under external perturbations.

Depending on the characteristics of the subject and of the entity of the perturbation, the response can be related to three different strategies, that is ankle

strategy, hip strategy and step strategy. The first one involves a significant contribution of the muscles at the ankle joint, and it is generally more relevant in young subjects. Hip strategy is typically highlighted in elderly and also in young people when subjected to high magnitude perturbations. It consists of the anti-phase rotation of trunk and lower limb segments, which enables large motion of the hip to regain balance and keep CoM as steady as possible. This strategy is mostly selected by elderly people because of minor muscular strength requirements, since it acts directly on the positioning of the human body CoM. Step strategy involves the actual step of the subject, so it is generally selected by people with stability problems or under perturbations with very-high magnitude. However, any subject response is generally given by a combination of ankle and hip strategies.

Models of human balance control try to replicate the main aspects of this complex process, and have constantly increased in complexity since the beginning. One of the first model was from Winter DA [30] in 1998, in which human body was represented by two segments, i.e. the foot (fixed on the ground) and a single rigid link to model the rest of the body. In this simple inverted pendulum model, the only joint taken into account was the ankle, and the movement was restricted to the sagittal plane. This simplified model was useful to develop some knowledge about the passive torque required at the ankle to stabilize the system under natural body sway in standing condition. Later on, Morasso PG introduced an active control scheme of balance in the model (based on *internal models* [31]), since it became obvious that the passive response is not strong enough for the human body to keep balance under significant perturbations of equilibrium. Nowadays, the models of postural control system have become even more complex, since they include multi-segment systems (e.g. [32] for thigh and trunk segments model, [33] for upper body, thigh and shank segments model), the combination of passive and active (delayed) response [34], sensory noise [18] and models of the CNS control strategy, which often is represented by a Proportional-Derivative (PD) logic [12, 34]. In addition, predictive elements are included too, in order to compensate time delays due to the active response [35]. However, in each model different solutions of sensory integration are implemented [19, 36]. In this complex scenario, it is particularly difficult to identify such parameters required to match the model with actual postural response data obtained from a human subject. Several model parameters identification techniques are implemented in order to estimate the unknown parameters of these complex model starting from experimental data collected during experimentation. Several Authors have worked on the application of techniques for non-parametric identification of linear systems to postural control system modeling. For instance, researchers in [7] have tried to identify postural control dynamics through calculation of cross-spectral densities of perturbation signals and of CoP/CoM displacements. In addition to kinetic and kinematic measurements as sources of information about postural control system response, [37] showed that EMG can also provide significant data for the model parameters identification, improving the accuracy of the

estimation and allowing for distinction between neural delays and electromechanical delays in muscle activity. Extended outlines of different methods to evaluate unknown parameters in balance control system models are presented in [38, 39].

1.1.4 Limitations of the state-of-the-art systems for posturography

The possibility to exert different mechanical stimuli leads to a complex scenario in which the characterization of the perturbations becomes really challenging itself. Similarly to the stimuli, postural response should be also assessed and characterized in an objective and indisputable way. The multiplicity of measurement data available about postural response allows for multiple observations but negatively affects the possibility to compare patients tested with different protocols. The lack of homogeneity in the results of stabilometry trials represents a serious limitation of these clinical practices, since it is still unknown which parameters are the most significant to describe the postural response. In conclusion, the multiplicity of solutions regarding perturbation systems and of methodologies for the interpretation of postural response represents the main reason for the lack of standard procedures in dynamic posturography.

In addition to the lack of standards, to improve the adoption of posturography in clinic, the equipment should be also designed to be easily accessible without any need for high skilled operators. For instance, typical perturbation systems in the research literature, such as movable platforms, lack the possibility to easily adapt the stimuli to the features of the specific patient, such as age, anthropometry, health condition.

Moreover, the significance of perturbation's features is discussed. For instance, minimum and maximum acceptable magnitudes of the stimuli, with respect to the risk of falls or step strategy to occur, are still questioned. Such circumstance not only depends on the amplitude but also on the energy, momentum and point of application of the perturbation, as well as on the constitution and health conditions of the patient.

Furthermore, the high cost and complexity of the systems available (both in the market and in the research literature) also represents a critical aspect of such technology, preventing its wide adoption in clinical facilities interested in postural analysis. For these reasons, even the clinical utility of posturography has been questioned recently and the discussion is still ongoing [40].

In conclusion, given the aforementioned limitations, clinicians would benefit from systems able to provide simple but repeatable and accurate perturbations, supported by relatively low cost instrumentation with high usability. In this framework, a simple and straightforward form of mechanical interaction with the subject is represented by a push with limited amplitude (to avoid step strategy as well as dangerous conditions for the patient) and short duration, resulting in an impulsive

and unpredictable stimulation. Since the control of such perturbation is fundamental to allow for non operator dependent trials, the interaction between a machine (i.e. a mechatronic perturbator) and a human subject must be investigated. In the following section, this theme is discussed and some applications are presented.

1.2 Interaction between human and machine

Human-machine interaction represents one of the main interests in robotics nowadays, due to the wide range of applications in which mechanical or mechatronic systems interact with human beings. Depending on the application, this interaction can take several shapes. For instance, in safety applications it is usually represented by undesired contact between an operator and the machine, while in tele-manipulation tasks it is related to an operator maneuvering an external device through a mechanical (sometimes haptic) interface. In both situations, it is essential to study such interaction to avoid any unsafe condition for the human subject and to match the requirements of the application. The ease to control the machine during impact and its entity are also related to the type of actuation these systems are based on. Depending on the relevance of human-machine interaction, even a system with simple architecture might require complex logics to keep such interaction under control.

1.2.1 Applications

One of the most relevant research themes dealing with human-machine interaction concerns safe contacts. Especially in industry, the presence of both robots and workers sharing the same space highlighted the need for safety measures in the control of machines to avoid any dangerous situation for people. The identification of safety requirements in such environments is an important aspect of this research [41, 42], as well as the study of the effects of unsafe and safe contacts on the human body [43, 44, 45]. In many industrial environments it is also relevant to develop new control strategies for collaborative robots [46, 47, 48], that is robots and workers working together, and not simply in the same room. Cooperation between robots and human operators can be useful to simplify many tasks, as lifting heavy loads or to enhance the skills of an operator during frequent and demanding operations[49, 50].

With respect to the aforementioned examples, robots for clinical applications are usually subjected to an even more urgent attention for accuracy, reliability and safety of human-machine interaction. Some applications such as robot aided surgery [51] or tele-manipulation require high precision in the interaction with a human operator, while mechatronic devices for rehabilitation [52, 53, 54] must be programmed in order to avoid unsafe conditions for the patient who is under

physiotherapy while they support the subject providing the required forces and torques with precision.

The works cited above represent only a limited part of the most relevant applications in which human-machine interaction is critical. In all of them, the monitoring of contacts and the control of this interaction, are crucial. In the following section, some examples of control logics developed to regulate the interaction between humans and machines are presented.

1.2.2 Control of the contact force

The design of the control logic is relevant and represents the main focus of many studies dealing with human-machine interaction. To regulate the contact forces raising from a collision between a machine and a person, passive or active control methodologies have been developed. The former techniques refer directly to the design of systems' architecture, endowed with devices able to avoid unsafe or jamming conditions, e.g. by means of compliant elements. An example is given by Remote Center of Compliance (RCC) for grippers, used to correct misalignments and centering errors in assembly tasks.

On the other hand, it is possible to focus on the active control of the contact by means of monitoring devices and servo-actuators. Among such techniques, hybrid force/position or impedance/admittance controllers have been widely implemented in the literature. In the first solution, the system can be controlled to track a desired trajectory while forces (or torques) at the joints are monitored and remain below specific thresholds [55]. When motion is restricted, e.g. when a contact is detected, the system switches its reference and starts regulating the contact force. In this way, both force and position constraints are respected during the operation of the robot. As pointed out in [55], hybrid control requires priority strategies, in order to solve conflicting situations, and measurement devices always to be available, in order to run simultaneously both controllers in parallel. While the case studies presented in [55] showed applications of hybrid control in rather simple environment, more recently, such control logic has been also tested in flexible mechanisms, both in planar [56] and in 3D environment [57]. These studies have highlighted the accuracy of hybrid position/force control in trajectory tracking and force regulation, though showing larger position errors for high magnitude contact forces in deformable environments [56]. Impedance control consists in the regulation of equivalent mechanical impedance parameters (mass, stiffness and damping) of the system while a desired trajectory is tracked by the control system. In this way, the plant (physical system) can exhibit several equivalent behaviors towards the environment, without changing its actual architecture. Admittance control instead is focused on the tracking of a force reference, hence the resulting motion of the system depends on the choice of the aforementioned parameters [58]. Applications of impedance control in robots for rehabilitation are presented in [59, 60], showing the

ability of such systems to assist patients with different characteristics by modulating equivalent damping and stiffness of the robot, e.g. exhibiting high stiffness for subjects with low ability, thus providing larger forces to guide the patient to track the desired trajectory. More complex control schemes, such as force-impedance [61], hybrid impedance [62], frequency-shaped impedance [63] control logics have been developed to overcome the limitations of basic formulations of hybrid position/force and impedance control, that is the effect of manipulator drift in presence of errors in modeling of the environment (in hybrid control) and the impossibility to follow a desired force trajectory or to consider high order impedances (in traditional impedance control).

While linear controllers are still currently used in many applications due to their simplicity and effectiveness, control of such complex interactions between humans and machines can really benefit from the implementation of non-linear controllers such as predictive control [64] and robust (model-based) control, e.g. sliding mode [65]. Non-linear controllers share the possibility to overcome the main limitations of linear controllers, hence they can take into account non-linear phenomena such as friction directly into the design of control logic. For these reasons, the performance of non-linear control systems are often much more accurate than the one provided by simple linear control schemes, especially if they are implemented where many modeling uncertainties and non-linear phenomena are highlighted such as pneumatic systems [66, 67, 68, 69]. The main drawbacks are given by a rather complex formulation of the controller, an increase of computational demand and the request for additional data about the current state of the plant, e.g. requiring transducers to monitor physical quantities useful for control logic design. For this reason, some Authors developed new methodologies to estimate unknown parameters of a plant, e.g. to evaluate pressures inside the chambers of linear pneumatic actuators [70].

In applications similar to the one presented in this dissertation, i.e. when the force to regulate results from an impulsive interaction, direct force control performed by minimization of the error between the reference and the measured signal must take into account several critical aspects regarding the assessment of contact phase, which cannot be usually determined a priori.

1.3 The aim of this work

Given the aforementioned limitations of current devices, this work of dissertation has the objective to present a novel system for dynamic posturography (named Perturbation Generation and Analysis System, PGAS), able to exert stimuli with predefined waveform, amplitude and length and to detect postural responses. In particular, the study will focus on the development of an automatic perturbator used to apply impulsive stimuli to the patients. Each perturbation must be scalable, hence its amplitude has to be easily configurable by the operator in order to

evoke responses with different entity. The scalability is also fundamental to allow for testing subjects with different constitution and health conditions. Furthermore, the perturbation must be adaptable, in terms of point of application and direction. This feature is relevant because it allows for unexpected stimulation of the patient. Such regulation has to be performed by the clinician in the easiest and most straightforward way, thus the perturbation device should be directly maneuvered by the operator by means of appropriate handles. The perturbation system must be eventually expandable to provide multiple stimuli at the same time. This feature can be comfortably achieved by design of simple perturbation devices which can be eventually replicated and coordinated to perform simultaneously. To this purpose, the architecture of the perturbation device must take into account low cost and compact solutions, hence simplifying its adoption in clinical facilities.

The research activity presented in this dissertation was carried out in a collaboration framework between the Department of Mechanical and Aerospace Engineering (DIMEAS) of Polytechnic of Turin (Italy), the Department of Neuroscience, University of Turin (Italy), and the Department of Physical Therapy, Faculty of Medicine, Tel Aviv University (Israel).

The dissertation will present the preliminary research activity conducted on healthy subjects (chapter 2) that helped defining the main specifications of the perturbation system (reported in [71]). In chapter 3 the PGAS is presented and a first version of the automatic perturbator is shown (presented in [72]). Chapter 4 presents the formulation of a PGAS model and a discussion about control logics, then an experimental test-bench aimed to the improvement of the perturbator's architecture is shown in chapter 5 [73, 74]. The final prototype of perturbation device is presented in chapter 6. Chapter 7 shows some insights on the interpretation of postural responses and on the models used to describe the behavior of human body subjected to external perturbations. Finally, conclusions and suggestions for future work are presented in chapter 8.

Chapter 2

Preliminary trials on healthy subjects with a manual perturbator

In this section, the outcomes of a preliminary analysis performed on 10 healthy subjects are presented. This step was fundamental to investigate:

- how to define the perturbation in a standardized way;
- how to measure postural response with reliability;
- the possibility to find a correlation between the perturbation and the postural response, hence to provide a preliminary clinical evaluation of subjects.

In the following sections, the device used to manually apply the perturbations (at thoracic and lumbar levels) is presented. The setting of the trials and the sensors used to detect the response are outlined in details. The outcomes of the trials are then discussed, providing relevant information for the design of an automatic perturbation device.

2.1 Manual perturbation device

The perturbations were applied directly to the body of subjects by means of a manual perturbator (MP) device (see Figs. 2.1 and 2.2). This device was realized at the Department of Mechanical and Aerospace Engineering of Politecnico di Torino, and consisted of the following parts:

- a 3D printed handle (in ABS) used to maneuver the device;
- an aluminum plate fixed to the handle and used to support a

- uniaxial load cell (Dacell Co. Ltd., Korea, UMM, rated capacity 50 kgf);
- 3 screws used to create a prismatic joint between the aluminum plate and the striker;
- a striker, used to contact the body of the patient hence to exert the impact force on the load cell;
- a deformable pad made of synthetic foam and used to uniform the contact pressure between the perturbator and the body of the subject.

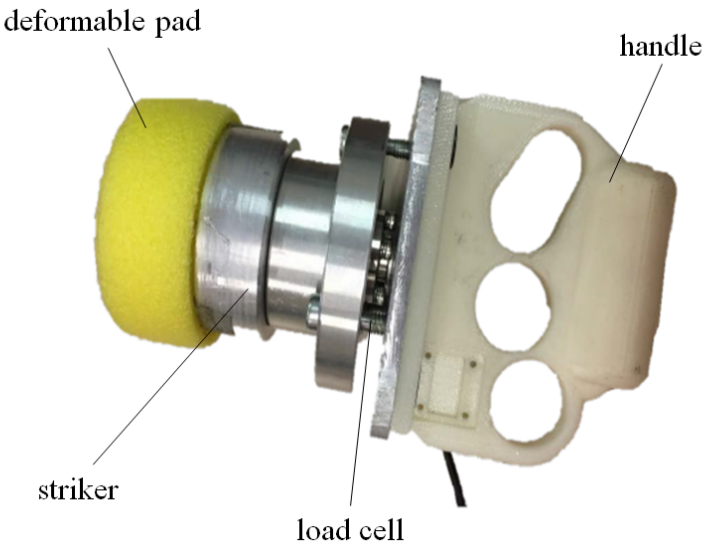

Figure 2.1: The Manual Perturbator.

A 3D printed handle allowed easy maneuvering of the device even for low skilled operators (see Fig. 2.3). The aluminum plate, screwed on the handle, provided support for the uniaxial load cell implemented to measure the contact force, as highlighted in Fig. 2.4. Surrounding the load cell, a cylindrical component, covered by a deformable pad and used to contact the body of the subject, was guided to slide by means of 3 screws realizing a prismatic joint (see Fig. 2.2). The screws were tightened enough to avoid plays between the sliding component and the load cell. In this way, the sensor was always kept in a pre-loaded condition in order to measure contact (compression) force with reliability. The pre-tensioning load was always subtracted from the actual measurement before each trial. The prismatic guide allowed the force sensor to be loaded only along its longitudinal axis. In this way, the radial components, that may arise when the perturbator is not directed perpendicular to the contact surface, could not exert any bending moment on the load cell. However, the operator was asked to orient the perturbator as much as

perpendicular to the body of the subject. The deformable pad, located at the far extremity of the perturbator, was necessary to distribute the contact force over a large circular surface area in order to avoid pain for the subject.

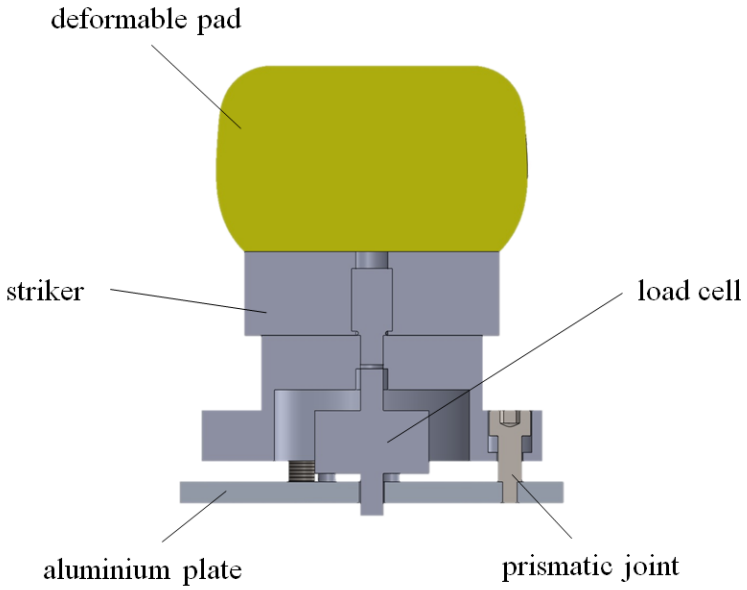

Figure 2.2: Cross-section view of the MP.

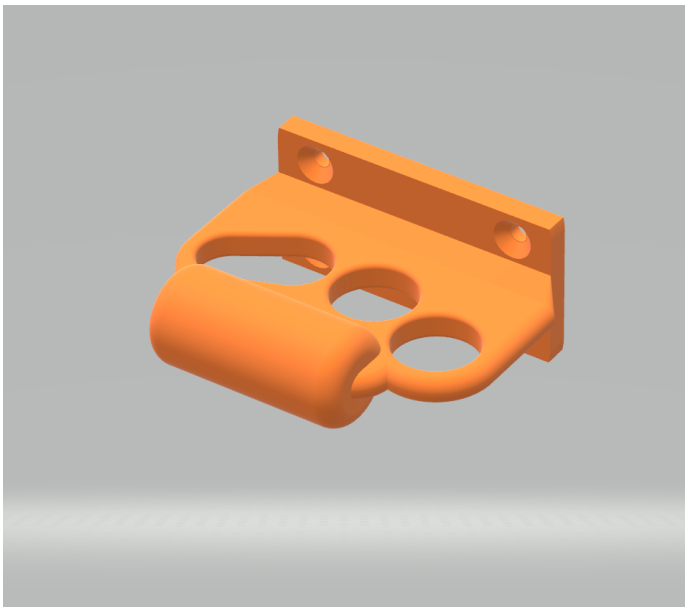

Figure 2.3: Render of the MP handle.

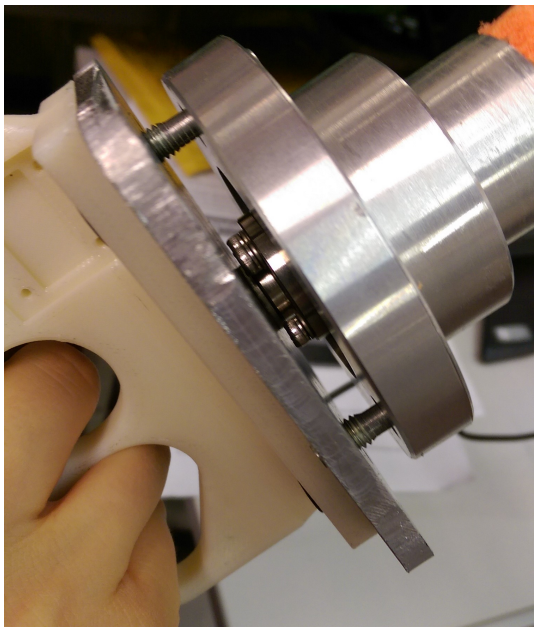

Figure 2.4: Particular of load sensor arrangement in the MP.

2.2 Instrumentation used to measure the response

The main objective of the preliminary trials was to evaluate the relationship between the response and the perturbation magnitude. In a first embodiment of the task protocol, the response was evaluated by means of EMG signals (gastrocnemius and tibialis anterior were considered, both limbs), linear acceleration of the trunk (L5 level) and CoP displacement. Linear acceleration was measured with a small, low power, three-axial MEMS accelerometer (ADXL325, Analog Devices, Inc., USA) that was mounted inside a custom made 3D printed box and fixed to the body of the patient at L5 level with an elastic stripe. However, only CoP measurements were considered in the final embodiment of the protocol. The EMG and acceleration signals were discarded since they did not provide relevant and reliable information about the subjects' response because of low Signal-to-Noise ratio (SNR). In particular, EMG signals were noisy probably due to poor conditioning of the subject's skin. Moreover, subjects with various body structures showed very different results regarding the quality of the signals, which is quite typical for surface EMG. Accelerometer measurements were instead discarded for their limited accuracy and significance. In particular, the acceleration measured during impact reflected the output of the load cell used to measure the contact force between the perturbator and the body of the subject. This result was clearer for lumbar perturbations rather than for thoracic ones, probably due to the proximity with the accelerometer. Theoretically, the acceleration of the trunk should provide relevant information about actual postural response only after the perturbation, i.e. during

the recovery of balance. However, mainly due to the small amplitude response and low SNR of the signal, the measurement did not provide any significant result.

On the other hand, CoP-related measurements provided better results and were considered in the following for the investigation of a relationship between the response and the perturbation. Nonetheless, it should be clear that EMG as well as cinematic measurements (IMUs, motion capture) would likely provide, as pointed out in many other studies, relevant information about postural response also for the specific methodology presented in this work. However, given the preliminary nature of this study, only CoP was considered for the sake of simplicity. It was measured by means of a modified Shekel (Beit Keshet, Israel) force platform. Originally, such device consisted of 4 independent plates, each one connected to a different uniaxial load cell (TEDEA, model 1042, rated capacity 100 kgf, Israel). The platform was modified in order to have a single plate simultaneously loading all 4 load cells, and two separate load cells were added to measure the antero-posterior (tangential) component of the ground reaction force (GRF). However, only the vertical component of GRF was considered for the analysis, since tangential forces provided by load cells did not affect significantly CoP estimation. The latter was calculated taking into account separately the antero-posterior and medio-lateral displacements.

The output of load cell embedded in the perturbation device was conditioned and amplified by a full Wheatstone bridge-based device, and then it was sampled by a 16-bit A/D converter (Micro1401-mkI, CED, UK). The sampling frequency was set at 1000 Hz, which was considered as a sufficient compromise between dynamic response and SNR of the force signal. Force signal was then filtered numerically with a low pass IIR (Butterworth) filter, fourth order, cut-off frequency of 150 Hz, after verification of the relevant frequency content by means of spectral analysis. The signals from load cells embedded in the force platform were sampled similarly with the same instrumentation. The A/D board was programmed with Spike II acquisition software (CED, UK). The setting of the trials as well as the instrumentation implemented are reported in Fig. 2.5.

2.3 Trials protocol

The trials were performed at the Laboratory of Integrative Physiology of the Department of Neuroscience, University of Torino, which also provided the instrumentation for data acquisition that has been outlined in the previous section. A group of 10 healthy subjects, males, with mean age of 27.3 $\pm$ 6.1y, were recruited. All of them did not present orthopedic nor neurological disorders. The research was approved by the institutional review board of the University of Torino (number 360583, November, 2017), and all procedures were performed in accordance with Helsinki declaration.

Since the perturbation device did not control the intensity of the stimuli, the

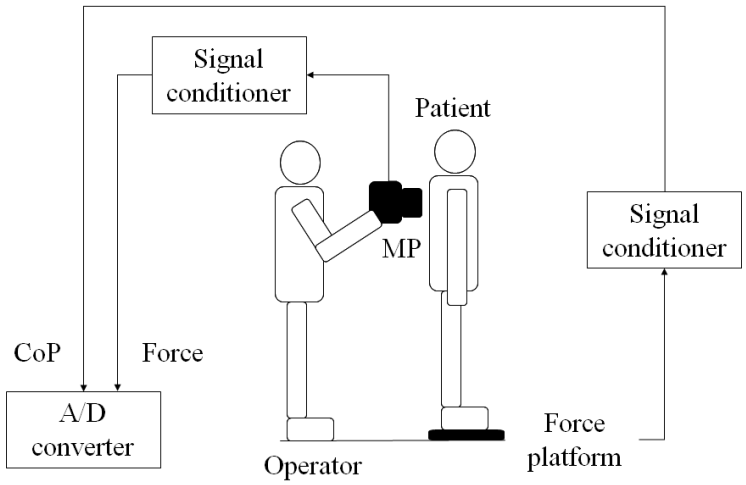

Figure 2.5: A scheme of a trial performed with MP.

operator was trained to deliver perturbations with limited duration and magnitude, in order to avoid step strategy to occur. Two locations for the stimuli were selected and highlighted with adhesives on the back of each subject. Since the operator stood behind the subjects, both to avoid eye contact and to ensure that each perturbation would be unpredictable, the two locations selected were inter-scapular (IS) level and mid-lumbar (L) level. Each subject stood barefoot on the force platform and familiarized with the protocol before the actual measurements were carried out. A total of 40 perturbations were exerted during the same session to the trunk of each subject, divided in two sets of 20 perturbations each. A break of 5 min was ensured between each set. After each perturbation, a time interval of 10 s was allowed to ensure that a following relaxed stance condition would be reached by the subject. Each sets consisted of 10 IS stimuli and 10 L stimuli, with the intensity self-regulated by the operator within the range of 20 - 60 N. The same random sequence of inter-scapular and mid-lumbar perturbations was used for all the subjects. The same protocol was repeated for each subject in two separate sessions, few days later. Each session lasted about 15 min. A picture from a trial in laboratory is presented in Fig. 2.6.

2.4 Output data

The output data refer to the variables used to characterize both the perturbation and the postural response. The stimuli were characterized in terms of:

- peak force (PF, expressed in N): maximum value of the contact force recorded during the perturbation;

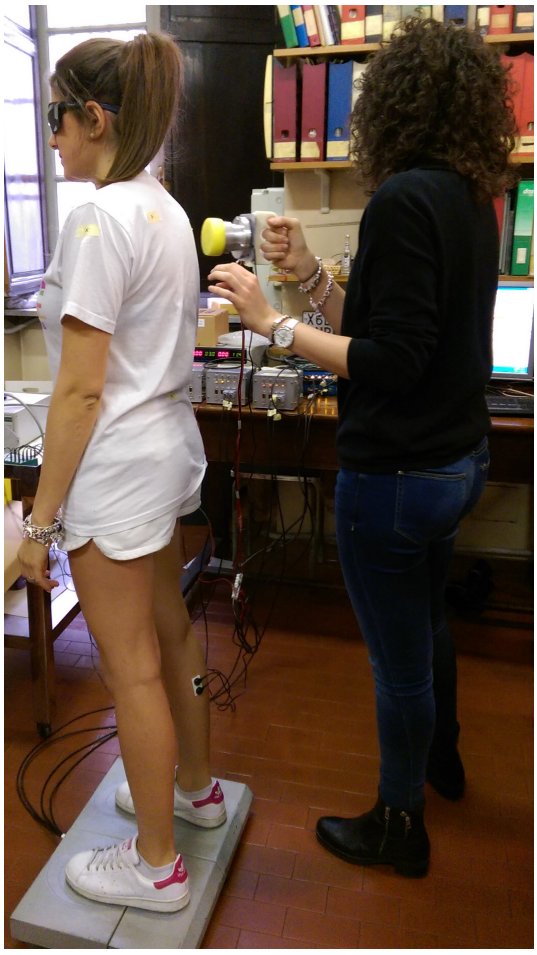

Figure 2.6: A trial performed with MP.

- duration (in s): time interval between the start and the end of the perturbation;
- impulse (I, expressed in N s): time integral of the contact force exerted during the perturbation.

The duration and the impulse refer to the same time interval, that was delimited by the time instants at which the contact force exceeded a constant threshold equal to 5% of the desired PF. While PF only provides information about the maximum of the intensity of each perturbation, I is directly related to the linear momentum of the body subjected to the impact. Since momentum depends on the change of the stricken body's speed, it provides a straightforward lecture of the energy related to the perturbation.

The CoP displacement occurring after the perturbation was calculated considering the low pass filtered (Butterworth, fourth order, 20 Hz of cut-off frequency)

antero-posterior (AP_c) and medio-lateral (ML_c) coordinates of CoP. The latter were calculated based on the signals provided by the load cells embedded in the force platform. For each stimulus, initial antero-posterior ($\overline{AP_c}$) and medio-lateral ($\overline{ML_c}$) positions were obtained by average of the coordinates during a time interval of 3 s preceding the perturbation. Then, CoP displacement CoP_{dis} was computed as:

$$CoP_{dis} = \sqrt{(AP_c - \overline{AP_c})^2 + (ML_c - \overline{ML_c})^2} \tag{2.1}$$

Given the CoP signal, the postural response was characterized as follows:

- latency(in ms): time interval from the beginning of the perturbation to the start of the postural response, that corresponds to the time instant at which CoP displacement exceeds a threshold equal to its mean value + 2 times the standard deviations;
- ΔCoP (expressed in cm): maximum of CoP_{dis} during the first second succeeding the perturbation;
- time to peak (in ms): time interval between the start of postural response and the peak of CoP_{dis};
- duration (in s): time interval from the start of postural response to the first CoP minimum occurring after the peak value.

An example of perturbation and response signals is presented in Fig. 2.7. Statistical analysis was performed with a two-way repeated-measures analysis of variance (ANOVA) on every variables related to the perturbation and to the response. Pearson's r coefficient was calculated for each subject to evaluate the correlation between stimuli and responses.

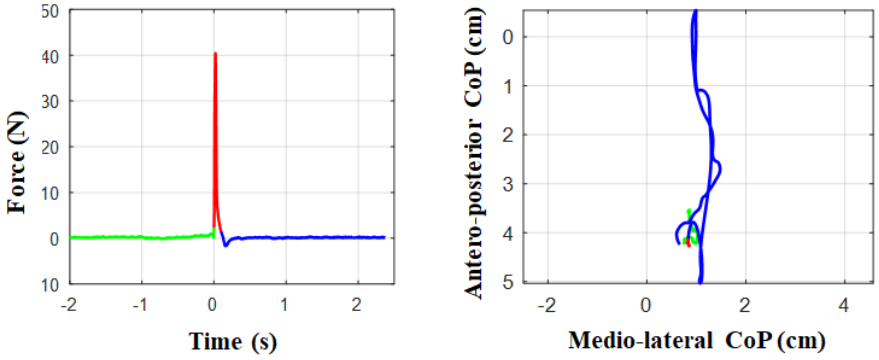

Figure 2.7: Force and CoP signals obtained for a subject with MP.

The intra-class correlation coefficient ($ICC_{3,k}$), based on a mean rating ($k = 20$), absolute agreement, 2-ways mixed effects model was used to evaluate the reliability

in both sessions of CoP response. Then, a mixed model analysis was used, that integrates the data points of all subjects into a single model. A random intercept and slope model was applied to study the relationship between ΔCoP and the perturbation. The fixed effects were I, PF, Site (IS vs. L), Day (day 1 vs day 2 of the tests), the interaction between Site and I and the interaction between Site and PF. ΔCoP was log-transformed to obtain a normal distribution prior to the application of the mixed model analysis.

2.5 Results and discussion

The mean values for the parameters used to define the perturbation were:

- PF: 42.0 N [19 - 88 N];
- duration: 139 ms [45 - 353 ms];
- I: 2.1 N s [0.6 - 5.5 N s].

For each value the range has been reported. A limited part of the stimuli (about 7%) were not included in the target PF range (20 - 60 N), however they were not removed from the analysis. The parameters did not depend on the specific session or level of the perturbation. The operator gave a positive feedback about the usage of MP, thanks to its low weight and grip. The quality of the contact force signal was good thanks to the assembly of the device that avoided any radial load on the force sensor. Moreover, the subjects did not report any pain related to the application of the stimuli. The main limitation of the MP was the difficulty to exert perturbations that would fall in limited ranges of PF, I and duration. Even if the operator trained herself in the usage of the device, it was not feasible to define accurately the features of the perturbations. This aspect is critical for the accurate investigation of a relationship between the characteristics of disturbances and the entity of postural responses. A device able to control the contact force *vs* time would have allowed for more reliable assessment of postural control ability. Moreover, it would have helped to shorten the length of each trial, therefore reducing the risk for adaptation.

In contrast with the perturbation parameters, the response latency and ΔCoP were dependent on the location of the stimuli. On the other hand, time to peak and response duration were not affected by the site and session. The results are briefly presented:

- latency ($p < 0.01$): 147 ± 56 ms (IS), 97 ± 22 ms (L);
- ΔCoP ($p < 0.05$): 3.5 ± 1.4 cm (IS), 2.5 ± 1.8 cm (L);
- time to peak: 516 ± 250 ms;

- response duration: 1.7 ± 0.4 s.

By analysis of the parameters used to define the response and the perturbation, it resulted that ΔCoP was significantly better correlated with I than with PF (see Fig. 2.8). This result was confirmed in all subjects for thoracic perturbations and

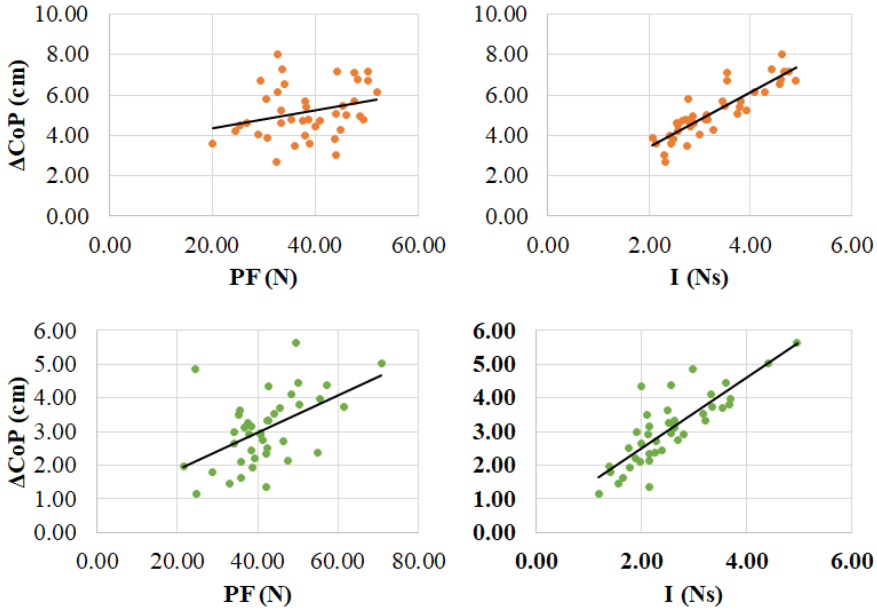

Figure 2.8: Relationship between perturbation PF or I and response ΔCoP for a subject: IS stimuli at the top, L stimuli at the bottom.

in the 80% of the subjects for lumbar perturbations. On average, the correlation between ΔCoP and I raised to 0.71 (IS) and 0.67 (L), whereas it was 0.5 for both levels of perturbation when PF was considered. This result, which was never presented before in the literature, confirms the preliminary assumption that the force impulse, being related to momentum hence to the energy of the impact, represents a more reliable parameter with respect to PF for the definition of the perturbation.

Then, the normalized ΔCoP (ΔCoP_n) was computed as:

$$\Delta CoP_n = \frac{\Delta CoP}{I} \tag{2.2}$$

This parameter, that resulted moderately correlated with the latency (0.66 for IS, $p < 0.01$, and 0.59 for L, $p < 0.01$), was selected to characterize each subjects in the two sessions since an almost linear correlation was found between ΔCoP and I. The mixed model analysis yielded a prediction logarithmic formula ($p < 0.05$, Eq. 2.3) that, if appropriately transformed, highlighted a nearly linear correlation

between I and ΔCoP.

$$ln(\Delta CoP) = 0.051(\text{if Day 2}) - 0.318(\text{if L}) + 0.276 \cdot I + 0.007 \cdot PF \tag{2.3}$$

This index remained approximately the same in both sessions and was higher for IS perturbations (see Fig. 2.9). The $ICC_{3,20}$ values for ΔCoP_n were 0.93 and 0.82

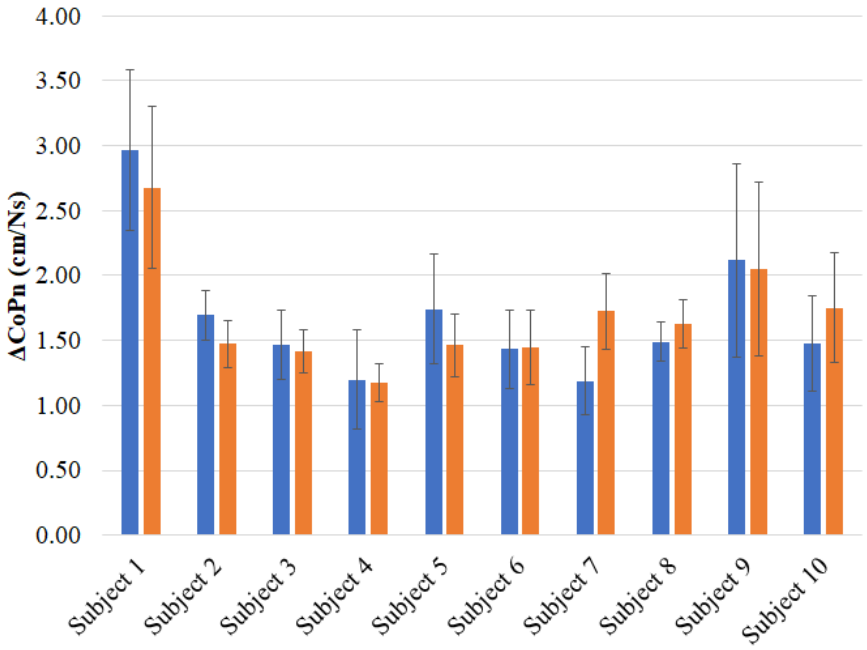

Figure 2.9: ΔCoP_n obtained in two sessions for IS stimuli: each bar refers to a session.

for IS and L respectively, showing the test-retest reliability of the results. Latency was also equally reliable. Reliability and consistency of ΔCoP_n among different subjects suggested the potential role of this index in the definition of postural control skills. However, it resulted surprisingly different and specific among the set of tested subjects and was not correlated with weight and height. These results are supported by recent studies that evidenced an average latency of 99 ms and CoP displacement between 44.7 mm and 80.4 mm, even though the experimental protocol was quite different from the one used in this preliminary analysis ([3], the subjects were pulled or pushed directly by hand at shoulders level). The correlation between ΔCoP and latency suggests that they could be linked. Given the same perturbation, a subject with slow reaction time (high latency) would require an higher correction torque at the ankle to counteract the loss of stability, therefore resulting in a higher ΔCoP. For this reason, high ΔCoP_n values would refer to less efficient postural control than low ΔCoP_n values. However, although a positive correlation between ΔCoP_n and latency is a promising outcome of this preliminary

analysis, further investigations are needed to support this assumption. In addition to the difficulty of an accurate control of magnitude and duration of the stimuli, this preliminary study presented the following limitations:

- small sample of subjects, all males and healthy;
- only antero-posterior perturbations were applied;
- only data related to CoP displacement were considered to characterize the postural response;
- a reproducibility study could not be performed due to the not accurate control of the perturbations.

Chapter 3

PGAS and a first prototype of automatic perturbator

3.1 Design process and requirements

The preliminary analyses shown in the previous chapter highlighted a promising and novel correlation between CoP displacement and the impulse of the contact force in all subjects tested. However, the MP did not allow to apply stimuli with selected amplitude, waveform and duration. Since a more consistent definition of the perturbations is required to confirm the preliminary outcomes of the first trials, a first version of an automatic perturbator (AP) has been conceived. Such device has been designed as part of a general system for perturbation and analysis, called PGAS (Perturbation Generation and Analysis System), which is currently patent pending.

PGAS consists of two main parts: a generation device, which is named AP (automatic perturbator), and an analysis system that is aimed to the acquisition of the postural response and to its interpretation. The final aim of this system is to provide controlled perturbations to the body of the subject, and to help finding a correlation between the characteristics of the stimulus and of the response. As already discussed in section 1.1.2, the response can be evaluated in multiple ways. For this study, CoP displacement estimation performed by means of a force platform was considered for ease of implementation and for the low effort required in data analysis. The design of an AP represented a far more critical point of the research presented in this dissertation, hence it will be discussed in more details. A detailed scheme of PGAS, based on pneumatic actuation, is shown in Fig. 3.1.

The AP has to provide scalable and adaptable perturbations, that is giving the operator the opportunity to select different amplitudes, durations as well as directions and points of application of the stimulus. Generally speaking, the AP can be conceived both in a fixed and in an hand-held configurations. The first one would require some turret-like structure or pole in order to hold the AP in

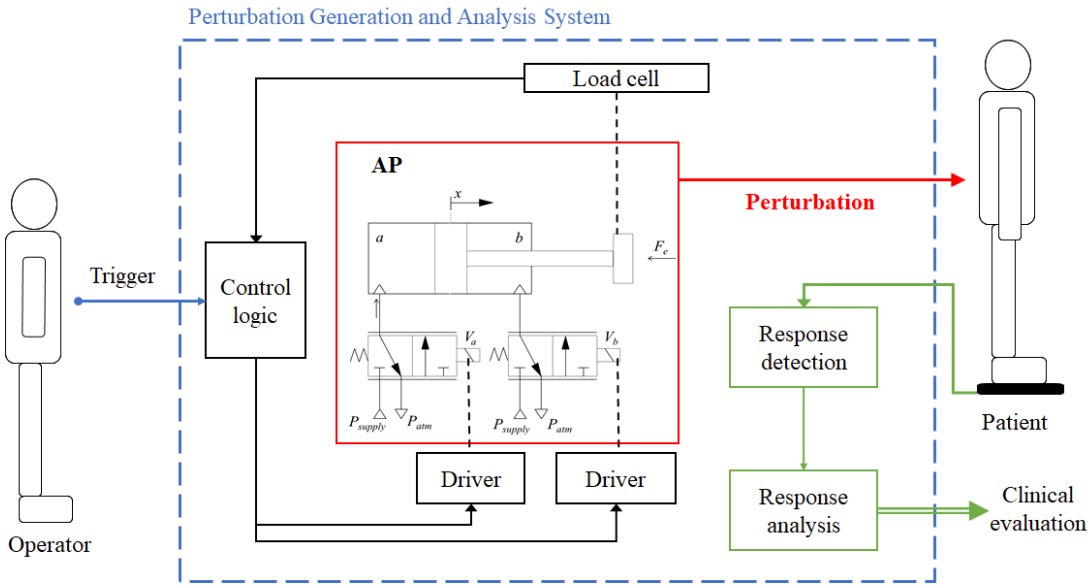

Figure 3.1: Scheme of Perturbation Generation and Analysis System; automatic perturbator (AP) based on use of a linear pneumatic actuator.

position and a motion controller to allow for different positioning and direction of the disturbance. On the other hand, the hand-held solution would require only one or more handles attached to the AP frame and used by the operator to maneuver the device. The MP discussed in the previous chapter was based on the second configuration too. Even if a fixed configuration would provide a stiffer system with less concerns regarding the accuracy of force control during impact, the AP was finally conceived as hand-held similarly to the MP. As highlighted by discussion with clinicians, a more compact solution, not requiring expensive technology for the accurate positioning of the striker, could be more easily adopted in clinical environments with respect to the fixed one.

Among the several actuation systems available, pneumatic actuation has been selected for being generally not expensive and suitable for clean environments. More expensive solutions with higher performance, especially regarding friction effects, are available and can be implemented similarly. However, it is primarily necessary to test cheaper solutions in order to get preliminary data about the efficacy of pneumatic actuation in such an application. As pointed out in the preliminary analysis, force profile should have limited magnitude, in the range of 20 - 100 N, to avoid any risky situation for the subject, and limited duration (below 250 ms) to reduce overlap with active postural response.

Based on those requirements, a first AP prototype was built. Its architecture and control logic design are outlined in the following sections. Then, the results of characterization trials and the first clinical trials on healthy subjects are discussed.

3.2 Architecture of the first AP prototype

The first prototype of AP (see Figs. 3.2 and 3.3) consisted of the following parts:

- a linear double acting pneumatic actuator (Metal Work S.p.A., Italy, ISO 6432, bore diameter 25 mm, stroke 120 mm);
- two flow proportional control valves (CKD Co. Ltd., Japan, 3AF2, 0 - 10 V of analog input, working pressure range 0-0.97 MPa) and dedicated control drivers (CKD Co. Ltd., Japan, APC-23);
- a uniaxial load cell (Dacell Co. Ltd., Korea, UMM, rated capacity 50 kg_f, nonlinearity, hysteresis and repeatability 0.1% of the rated capacity) and signal conditioner (DEWETRON GmbH, Austria, DEWE-RACK-4);
- an end striker covered by a layer (thickness 20 mm) of polyethylene;
- two handles (in aluminum);
- a trigger button to enable the perturbation.

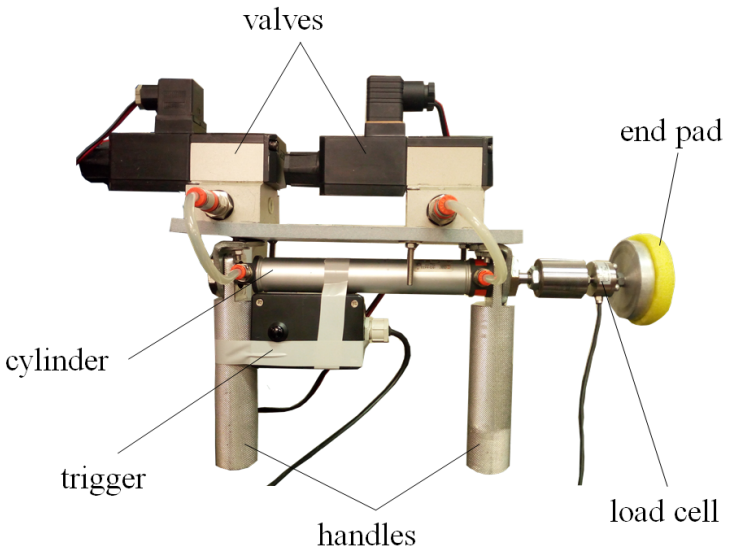

Figure 3.2: Components of the first AP prototype.

The system was supplied by a gauge pressure of 3.5 bar and controlled by a real-time system (dSPACE GmbH, Germany) for signal acquisition (DS2002 board, 16 bit and 32 channels) and generation (DS2101 board, 12 bit and 5 channels). The control logic was programmed in MATLAB® and Simulink® Real-Time™ (The

MathWorks, Inc., USA) and ControlDesk® (dSPACE GmbH, Germany) software, with sampling frequency equal to 200 Hz.

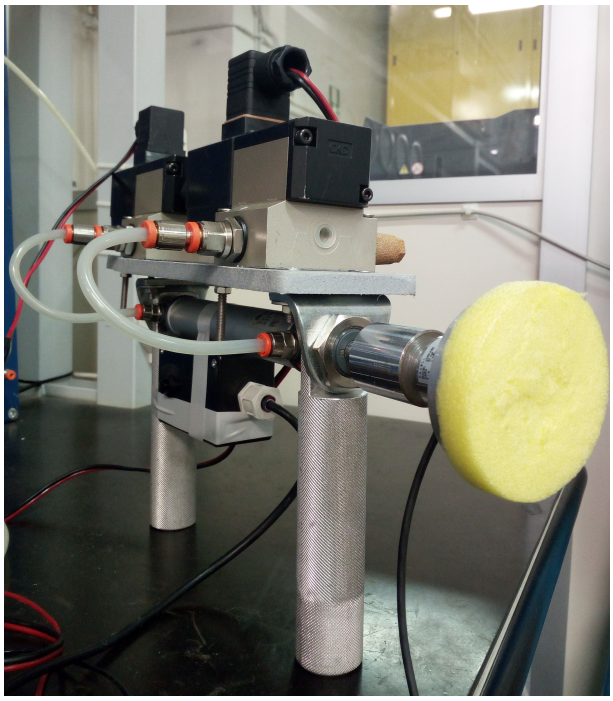

Figure 3.3: The first AP prototype.

The stroke of the actuator was selected to allow the operator to stand not too close to the subject, hence to ensure unpredictability of perturbations. The pneumatic cylinder implemented in the prototype was a typical low cost one with large availability. The size of the cylinder was relatively small, since opting for fast dynamic response was far more significant than prioritizing the maximum force provided by the actuator. Because of that, small cylinders could be implemented and provide the required force magnitude even if working at relatively low supply pressure (between 3 bar and 4 bar).

To control the actuator, a simple pneumatic circuit comprising two three-way flow proportional valves was realized. A flow proportional valve is a device able to accurately control the air mass flow, e.g. regulating the flow directed towards or coming from one of the chambers of a pneumatic cylinder. Typically, flow rate is continuously modulated by the current supplied to a solenoid. The size of the valve affects directly the maximum flow rate and response time, hence it is fundamental to find the optimal agreement between them with respect to the dynamics required by the application. For the design of the AP, two flow proportional valves with 0 - 10 V of analog input range were selected. The voltage reference signals were provided by the control system with the aim to regulate the contact force and to move the piston as intended. In order to improve the dynamic response as much

as possible, the valves were placed directly on top of the cylinder, fixed on a frame integral with the actuator (see Fig. 3.3), whereas the drivers were placed apart and near the acquisition and control hardware (Fig. 3.4). The weight of each valve, approximately 1 kg, was considered still acceptable to embed the valves in the body of the AP. However, more compact and lightweight devices can improve the handling of the perturbator. Each valve was connected to a different chamber of the actuator, in order to control separately input and output mass flow rates.

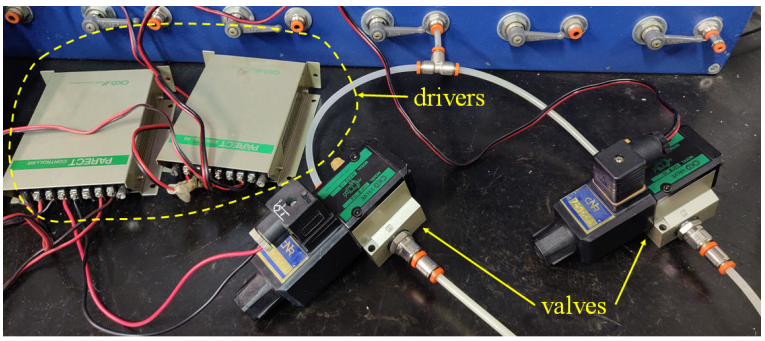

Figure 3.4: Valves and drivers used to control the actuator.

At the end of the piston rod, a cylindrical support was fixed and used to hold a uniaxial load cell in position. Since the sensor could measure only compression or tensile forces along its longitudinal direction, it was asked to the operator to orient opportunely the perturbator when applying stimuli to the subjects. In order to compensate for non-axial loads and to reduce operator's effect on device performance, it could be possible to: (1) use a prismatic guide-like structure similar to the one designed for the MP; (2) mount a 6 DoF load cell. The latter solution, besides being more expensive, would provide additional complexity in the analysis of the contact force signal with respect to the uniaxial solution implemented. The range of the load sensor (50 kg_f) was selected to avoid any unsafe condition of the transducer, since the maximum force expected was about 100 N. The sensor was calibrated and zeroed through control logic software before each capture. At the far end of the load cell, an end damping pad (buffer) covered by a deformable synthetic foam was used to distribute the load on a wide surface, similarly to what was done for the MP (see Fig. 3.3). This was useful to avoid discomfort and pain for the subject.

3.3 Control logic design

With respect to MP design, the AP was based on the automatic control of the contact force exerted to disturb the balance of subjects. As discussed in section 1.2.2, several architectures exist to design force control logics. However, very low

emphasis has been put on the actual control of the contact force profile (i.e. force *versus* time) during high dynamics impacts. Given the very simple architecture of the first version of AP, a direct force control was developed, being the load cell output the only quantity continuously monitored to assess the state of the device. The system had to control the force only when impact occurred, hence during a short time period lasting few hundreds of milliseconds.

The control logic architecture was designed as sequential, therefore considering four phases that differently regulate the actuator motion depending on external events (see Fig. 3.5). The four phases considered are the following:

- idle;
- approach;
- strike;
- return.

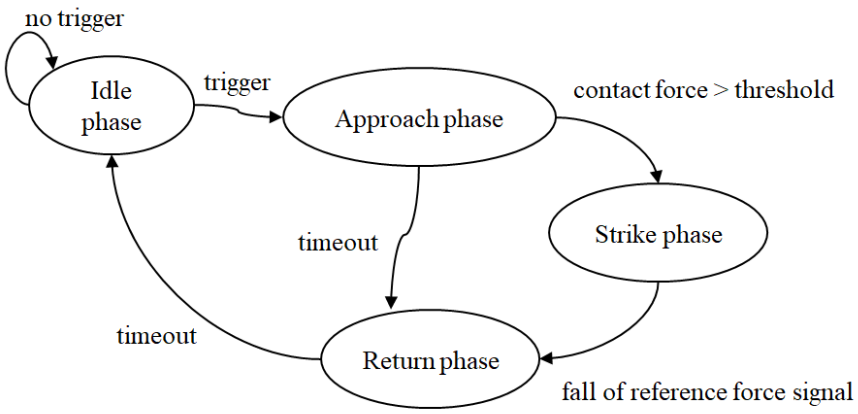

Figure 3.5: Sequential control logic of the AP.

3.3.1 Idle phase

Idle phase represents the resting condition of the AP, in which the chambers of the actuator are completely discharged. In this phase, the system continuously monitors the input signal given by an external trigger, which is under control of the operator. When the latter triggers the stimulus, the control logic shifts in the second phase, i.e. the approach phase.

3.3.2 Approach phase

In this condition, the piston, which is initially fully retracted, must extend in order to reach the target. The control logic regulates the extension of the actuator, which is limited by the maximum stroke available. This phase is particularly significant for the accurate control of the impact force, since it defines the contact velocity hence the energy and momentum of the impact. Slow approaching perturbator is not advisable, since it affects the overall duration of a trial. On the other hand, fast approach can be dangerous for the subject and have negative effect on the accuracy of the control. Therefore, it is fundamental to select an appropriate velocity for the approaching phase. Since this first AP prototype only had a force sensor on its tip, it was not possible to design an actual position or velocity control of the piston rod during this phase, therefore it had to be open-loop controlled. The open-loop control is realized by selection of appropriate command voltage signals for each valve during approach. These values were defined by means of iterative procedure, trying to achieve the best compromise between velocity of execution and accuracy of the force control during impact. Since the input regulating signal for each valve ranges between 0 and 10 V, with the central (neutral) position at 5 V, the valve connected to the rear chamber of the actuator must be controlled by a 5 - 10 V signal, whereas the other one shall be controlled by a 0 - 5 V command. To enable fast piston sliding, the front chamber could be discharged completely. On the other hand, values around 4 - 4.5 V for the front chamber command could add some damping to the motion of the piston, thus limiting the initial overshoot in the contact force signal. With the selected voltages (presented in following sections), the perturbator completed a typical stroke of 8 cm in about 1.5 s.

3.3.3 Strike phase

The approach phase was programmed to last at most 4 seconds. This timeout condition was reached if no perturbation occurred, e.g. when the operator was too far from the subject. Otherwise, the rise of the contact force above a defined threshold carries the system to the third phase, i.e. the strike phase. In this condition, the system performs the actual direct control of the contact force. The definition of the threshold is critical for switching between approach and strike phases. Theoretically, the threshold should be as lower as possible to enable fast switching between open-loop motion control and closed-loop force control. However, noise generated by the load cell, by the signal conditioning system and by the cable (BNC connectors were used) all contribute in raising the baseline of the signal. A threshold equal to 5 N was selected for this application since numerical noise consistently remained under that value. To filter out high frequency noise components, a Butterworth IIR low pass filter (4^{th} order, cut-off frequency equal to 10 Hz) was applied to the signals. To increase SNR, it could be also possible to

select a force sensor with narrower range to improve matching between transducer dynamics and stimuli amplitude.

The implementation of direct force control might consider rather complex architectures, that often rely on additional sensors or mathematical modeling of the plant to get information about the state of the system. For sake of simplicity, the control logic was based on a Proportional-Integral (PI) controller, using the load cell signal for force feedback. With this solution, the command voltages for the valves are given by the following relations:

$$V_{rear} = k_p(F_{set} - F_{measured}) + k_i \int (F_{set} - F_{measured})\, dt + V_0 \tag{3.1}$$

$$V_{front} = -V_{rear} + V_0 \tag{3.2}$$

In both Eqs. 3.1 and 3.2, the V_0 term represents the voltage corresponding to the neutral position of the valves. V_{rear} and V_{front} were defined symmetrical with respect to the zero position, therefore when an actuator chamber is charged, the other one is simultaneously discharged of the same amount. Tuning of PI controller was performed by a semi-empirical iterative approach (Ziegler-Nichols) for different durations and amplitudes of the perturbation. The system allows to select any waveform with defined amplitude and duration. When the zero-crossing of the reference signal F_{set} occurs after the start of the perturbation, the system shifts to the final return phase.

3.3.4 Return phase

This phase, similarly to the approach one, can be open-loop or closed-loop controlled. However, since fast retraction of the piston is required, the system is forced to return to the next idle phase as fast as possible. This behavior is achieved by charging the front chamber of the actuator while the rear one is completely discharged. When the return phase is triggered, after a short timeout period the system forces the transition to idle phase, then it waits for the next trigger. As stated above, return phase is also triggered if no perturbation occurs in the next 4 s after the operator trigger.

3.4 Characterization trials of the AP

The device was characterized in laboratory in order to get some preliminary data about its performance. Both a fixed and an hand-held configurations were considered, since they present different challenges for control logic efficacy. In particular, a fixed configuration, in which the AP is placed on a fixed test-bench, avoids oscillations in the device positioning due to the operator. In this configuration, contact force profiles lasting 250 ms and 500 ms were tested. Moreover,

different initial distances between perturbator and target were considered (55 mm and 80 mm). The magnitude of perturbations was set between 50 N and 75 N, kept constant during the duration of the strike. In all of these trials, the target was represented by a fixed metal plate covered in foam. After the initial trials, the device was tested in a hand-held configuration, therefore it was maneuvered by a skilled operator and used to exert automatically-controlled stimulations to the fixed target. In this configuration, since it was not possible to measure the actual distance between striker and target, the operator was asked to keep such distance as constant as possible.

As presented in Fig. 3.6, the tracking of force profile seemed not sufficiently accurate in both configurations, with slow transients in the initial and final part of the perturbation. In stimuli theoretically lasting 250 ms, an average duration of 350 - 400 ms was reached. On the other hand, no significant overshoot in the contact force was highlighted. Slow dynamic response depends on the components selected,

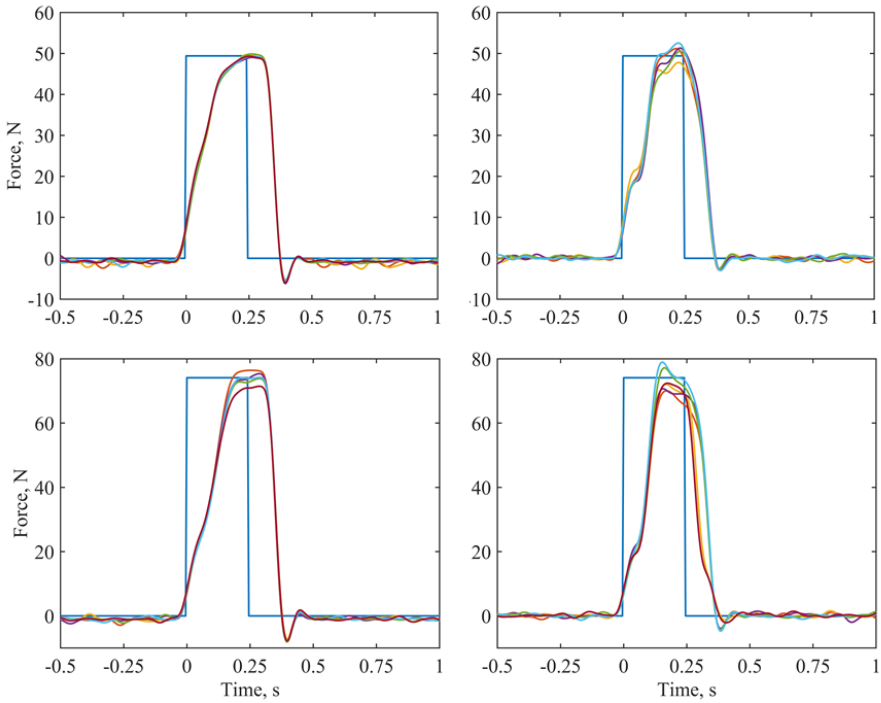

Figure 3.6: Force tracking in fixed (left, top and bottom) or hand-held (right, top and bottom) configurations. Each plot shows several repetitions of the same task during a trial (6 consecutive perturbations on the left, 5 on the right). The figures on top refer to a force reference of 50 N, the bottom ones to 75 N. In all trials, the duration of reference stimuli was set to 250 ms [72].

which were generally not expensive but showed limited performance, especially the pneumatic cylinder. Moreover, performance was likely reduced by the selected

valves that showed limited speed and accuracy during the trials performed. In both configurations, focusing on both duration and amplitude of the stimuli, the system showed repeatable results, with better performance in fixed condition. To assess the repeatability, the time integral of the contact force was computed for each trial and compared with the reference force impulse. Results of this comparison are shown in Table 3.1. This outcome highlights good repeatability of the stimuli among several trials, hence enabling more standardized protocols of stimulation with respect to the one provided by the MP. Force tracking showed instead only acceptable accuracy, demonstrating that the solution tested could not fulfill completely the requests of the application. As shown in Table 3.1, the system performed with less accuracy when a 75 N magnitude was selected, and it also required additional tuning of the controller gains. A comparison between 50 N and 75 N perturbations lasting 500 ms is presented in Fig. 3.7.

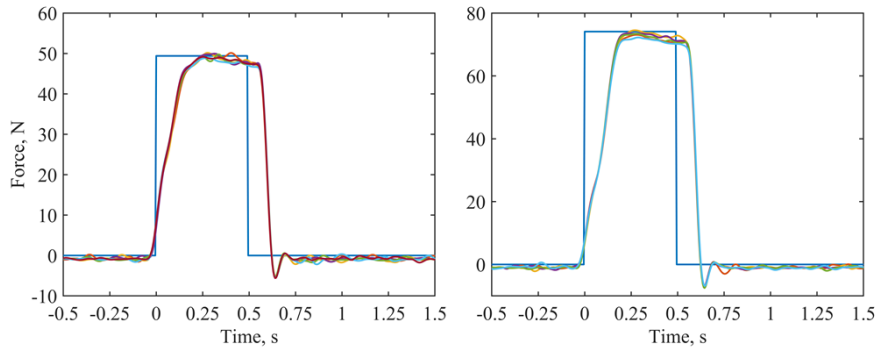

Figure 3.7: Force tracking in fixed condition for 50 N (left) and 75 N (right) perturbations lasting 500 ms. Each plot shows several repetitions of the same task during a trial (6 consecutive perturbations on the left, 5 on the right) [72].

Configuration	**Set Impulse** (N s)	**Impulse (mean ± std,** N s)
Fixed	12.50	13.88 ± 0.05
Hand-held	12.50	12.49 ± 0.24
Hand-held	18.75	17.13 ± 1.20

Table 3.1: Impulse values in fixed and hand-held configurations.

In addition to the outcomes of aforementioned trials, other aspects were also considered during this preliminary characterization. The effect of supply pressure on the system was evaluated rising the default value of 3.5 bar to 4.5 bar. In the second condition, the system presented significant overshoot in the contact force, due to the increased amount of energy available. For this reason, controller gains

had to be re-tuned accordingly to the increased supply pressure to avoid overshoot. However, pressure variations did not seem to produce any significant improvement in the system's performance. Moreover, working with high level pressures might be not advisable in specific contexts such as clinic environments.

The effect of different valve command voltages during approach phase was also evaluated. The default value of $V_{rear} = 5.6$ V and $V_{front} = 5$ V were changed respectively to 5.7 V and 4.7 V, therefore increasing the velocity of the piston during approach. The resulting force profiles presented a shorter initial transient, however they also showed less accuracy in the regulation of peak force. Impulse accuracy was also negatively affected by such unstable behavior and required additional tuning of the controller to get acceptable results. This observation confirms the necessity for a more accurate control of piston motion during approach phase in order to get a more reliable and efficient system.

In order to verify the performance of AP when hand-held, since it is not possible for the operator to easily maintain a constant positioning with respect to the subject, the device was tested on the fixed bench by selecting different values of initial distance (55 mm and 80 mm) between striker and target. The results of this comparison are presented in Fig. 3.8 for 50 N perturbations. In this particular configuration the device seemed only slightly affected by the initial distance, showing very similar performance in both conditions. However, given the same controller gains, the peak force observed in the 55 mm condition was definitely higher than the one obtained in the 80 mm condition. Closed-loop motion control during approach could significantly reduce or completely remove the dependency between initial positioning of the operator and the performance of the system.

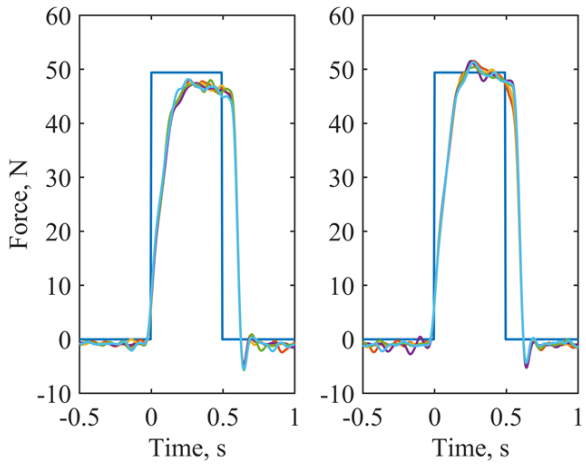

Figure 3.8: Force tracking in fixed condition for different values of initial distance between the perturbator and a fixed target: 80 mm (left) and 55 mm (right). Each plot shows 5 repetitions of 50 N stimuli [72].

3.5 First trials on healthy subjects with AP

Even though the performance of the system in preliminary characterization trials was not sufficiently accurate, first trials with the AP prototype were carried out on 20 healthy subjects, therefore enlarging the number of samples with respect to the preliminary study performed with the MP. Among the subjects, 10 people were young (23.5 ± 1.5y) and 10 people were adult (53.2 ± 8y). Only 5 subjects were female, then it was not possible to evaluate the dependency between response and gender. Each subject was analyzed in two separate sessions, with 20 perturbations each. Only antero-posterior perturbations, with thoracic and lumbar levels selected randomly, were imparted. Two magnitudes were decided, equal to 12 N s (for the first session) and 18 N s (for the second session). An example of trial performed in laboratory is presented in Fig. 3.9.

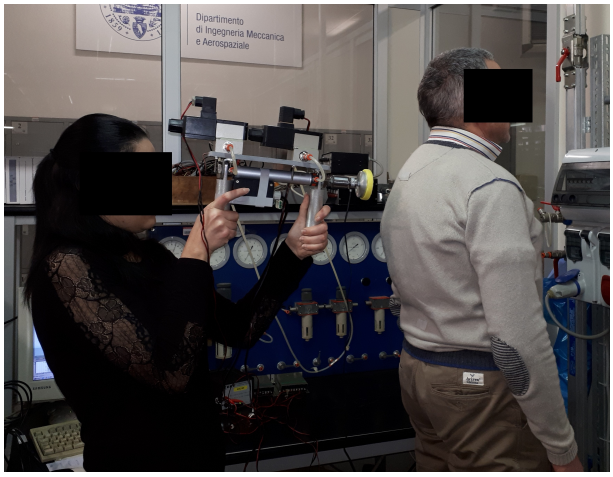

Figure 3.9: The operator and a subject during a trial performed with the AP, first prototype.

With respect to force profiles obtained in first trials, the accuracy of force tracking worsened as pointed out in Fig. 3.10.

An accuracy error has been evaluated as:

$$\text{Impulse accuracy error} = \frac{|I_{mean} - I_{set}|}{I_{set}} \cdot 100 \tag{3.3}$$

where I_{mean} is the average value of contact force impulse. Perturbations were distinguished between thoracic and lumbar levels. Figures 3.11 and 3.12 present respectively the impulse values and accuracy error results, showing that force control performed more accurately when lower magnitude of perturbation was selected (session 1). However, repeatability was still good, especially for lumbar perturbations.

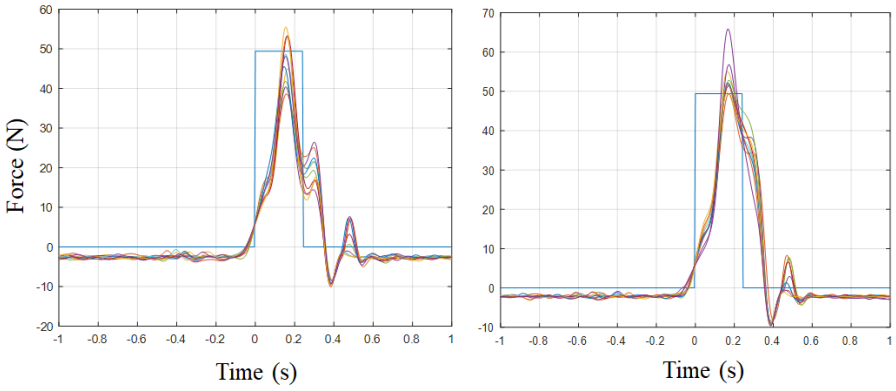

Figure 3.10: Force tracking in hand-held condition during experimental trials on healthy subjects. Thoracic stimuli on the left, lumbar stimuli on the right.

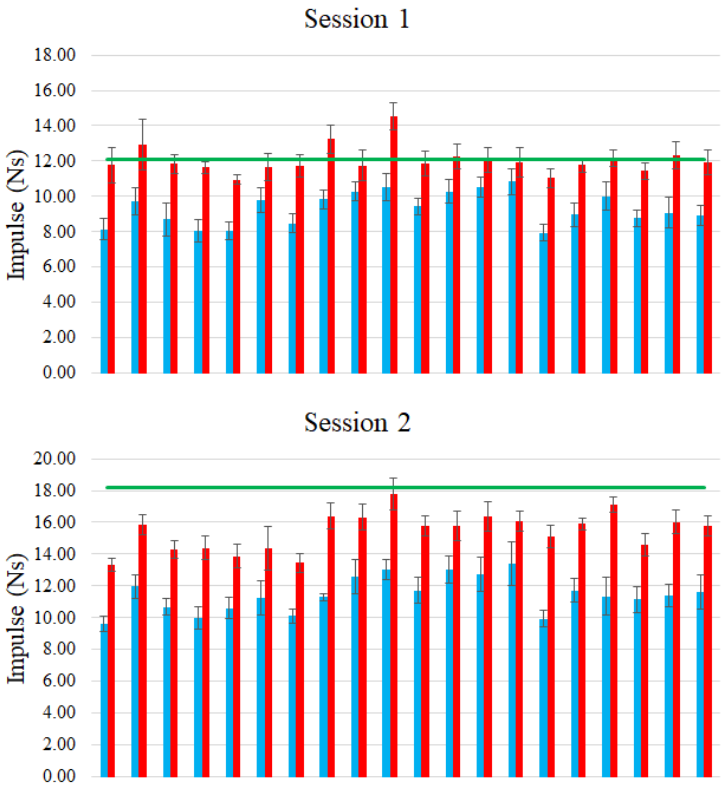

Figure 3.11: Impulses obtained in two sessions for reference values of 12 N s and 18 N s stimuli on 20 subjects. Blue and red bars refer respectively to thoracic and lumbar perturbations, green bars represent the reference impulses.

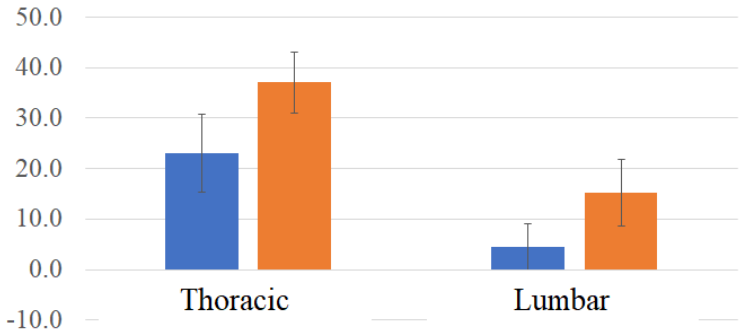

Figure 3.12: Impulse accuracy error for thoracic and lumbar perturbations. Blue and orange bars refer respectively to first (12 N s) and second (18 N s) session.

The ratio between CoP displacement and impulse (ΔCoP_n) was calculated for each trial, showing good repeatability and reliability (variation coefficient below 15 %). This postural index resulted consistently higher for thoracic perturbations, probably due to the increased lever arm of the perturbation force with respect to the ankle joint. CoP displacement was inversely proportional to the mass of the subject, especially for adult people. The postural index ΔCoP_n was not significantly affected by the session considered, supporting the idea that this parameter could be used to characterize postural control ability in clinics (see Fig. 3.13).

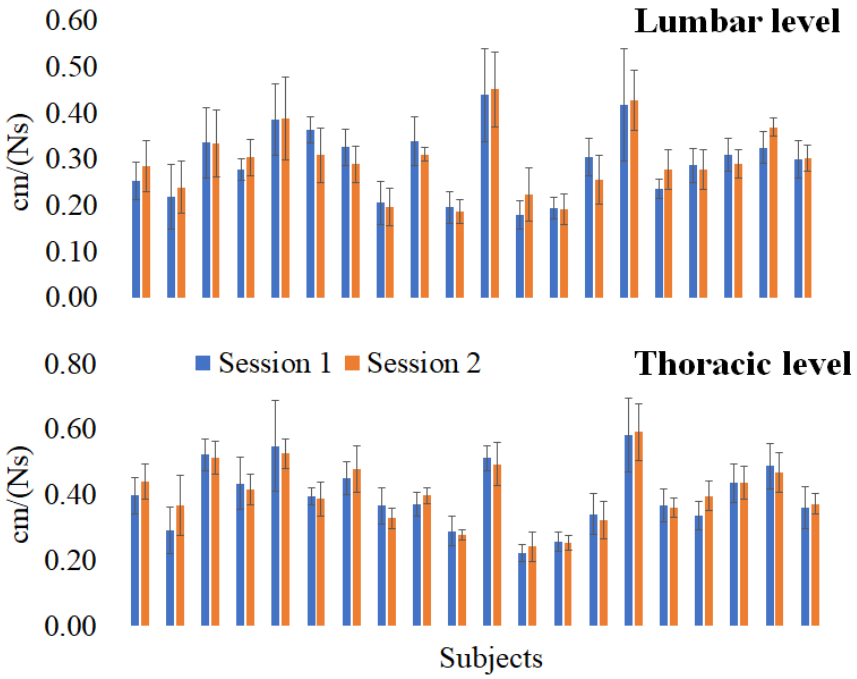

Figure 3.13: ΔCoP_n obtained in two sessions for thoracic and lumbar stimuli.

3.6 Critical aspects of the first AP prototype

The realization and testing of the first automatic perturbator showed that a simple architecture based on common commercial components could only partially fulfill the specifications required by the application. Good reproducibility of the perturbations and repeatability of trials conditions were the main outcomes of the first analyses, however force tracking accuracy was very limited, with unacceptable slow transients that affected the duration of stimuli. This result is very important since short lasting perturbations are required to reduce the overlap between the stimulation and active postural response. However, slight differences were observed by comparison of the performance in fixed and hand-held configurations, therefore the device showed enough robustness to be implemented in a clinical environment and directly maneuvered by the clinician. Limited accuracy in force control can be tackled in different ways:

- testing different types of actuation;
- selecting different components with higher performance;
- definition of more complex and reliable control logics, e.g. based on modeling of the system and of its interaction with a human subject.

Since pneumatic actuation owns several advantages with respect to electrical or electro-mechanical actuation, as previously discussed, the research still focused on this kind of actuation system. However, to test different components and control systems, it was necessary to define an environment in which it could be possible to perform such analyses. For this reason, it led to the definition of:

- an analytical and numerical model of PGAS, that is of the automatic perturbator interacting with both the operator and the subject;
- an experimental test-bench used to physically test different components and control solutions.

These two topic will be discussed in the next chapters. The development of a model and of a test-bench was considered fundamental for the design of a second AP prototype, that will be presented and discussed later.

Chapter 4

Modeling of PGAS and control logic design

Modeling of PGAS was necessary to get a better understanding of the interaction between the AP and both the subject and the operator. In the following sections, the model is outlined in details and validated thanks to experimental data. Then, different control solutions aimed to improve the performance of the automatic perturbator are presented and discussed.

4.1 PGAS model

PGAS involves two connected human-machine interactions, that is:

- the interaction between the operator and the device (AP);
- the interaction between AP and the subject of postural analysis.

The two physical interactions are interlaced since the characteristics of one interaction depend on the other one and vice versa. For instance, the energy of the impact occurring between the AP striker and the body of the subject is affected by the stiffness of the interaction between the perturbator and the clinician handling the device. Therefore, it is fundamental to analyze the behavior of the main parts of the system as a whole, and not separately, since the performance of the general system are affected by the single interactions among the parts. Since the human-machine interfaces in this application are rather difficult to describe, several models can be defined with different complexity. The choice of a single direction of the perturbation can be useful to simplify the description of such interactions, since the movement of the stricken body can be approximated by a translation along the direction of the perturbation. Since only antero-posterior stimuli were given in the experimental trials on healthy subjects, the movements of the operator and of the subject, as well as the sliding of the piston rod, were modeled as single DoF. This

approximation allowed for the definition of a model that could be implemented easily. Since model-based control logics were also considered (and presented in the following sections), the definition of a model with limited numerical demand was also necessary to enable fast response timing of such control designs.

The main parameters of the model are presented in Table 4.1.

Description	**Symbol**	**Unit**
Mass of cylinder tube	M_1	kg
Elastic constant of the operator	k_1	N/m
Damping coefficient of the operator	β_1	N s/m
Mass of the stricken body	M_2	kg
Elastic constant of the stricken body	k_2	N/m
Damping coefficient of the stricken body	β_2	N s/m
Elastic constant of the buffer	k_3	N/m
Damping coefficient of the buffer	β_3	N s/m
Cylinder bore	d_c	mm
Piston rod diameter	d_s	mm
Mass of the piston	m	kg
Initial stroke of the piston	x_0	mm
Total stroke of the piston	x_l	mm
Dead band of the cylinder	x_m	mm
Initial pressure	P_i	bar
Initial temperature	T_i	K
Polytropic coefficient of air	n	
Air viscous coefficient	γ	N s/m
Air density at 25°C temperature	ρ_0	kg/m^3
Supply pressure	P_s	bar
Atmospheric pressure	P_{atm}	bar
Friction force on the piston	F_{fr}	N
Max static conductance of the valve	C_{max}	l/(s bar)
Critical ratio of the valve	b	
Max voltage command of the valve	V_{max}	V
Valve time constant	τ_v	ms

Table 4.1: Main parameters of PGAS model.

4.1.1 Operator and stricken body modeled as mechanical impedances

The operator interacts with the AP by means of two handles. Therefore, he or her represents the constraint of the perturbator towards the environment. This

constraint is not infinitely rigid, since the clinician is allowed to move during the application of the perturbations. To correctly applying the stimuli, the operator should remain as stiff as possible, however this cannot be guaranteed without the additional support of a fixed frame. For this reason, this first interaction (between the clinician and the device) was represented by a visco-elastic behavior, i.e. by means of a Kelvin-Voigt model. In this simple model, the force exerted by the cylinder tube on the environment depends on the translation of the actuator frame as well as on its rate of change. Since the actuator is also defined by a mass (which can be considered lumped or distributed), the interaction between the device and the fixed frame (environment) was described by a mechanical impedance, whose parameters are M_1, k_1 and β_1, respectively the cylinder tube mass, spring constant and damping coefficient of the Kelvin-Voigt model. This modeling, even though it is quite simple and only takes into account the passive response of the operator, is commonly used for the generality of the results it provides.

Similarly to the operator's model, the stricken body (i.e. the body of the subject that is perturbed by the AP) was modeled as a second mechanical impedance, with similar choice of parameters M_2, k_2 and β_2. As already discussed in section 1.1.3, rather complex modeling of postural response are available. However, since the perturbation occurs in a very limited time interval, the performance of force control during impact is likely more affected by the passive response of the subject rather than by the active one, which is generally evoked with a latency depending on the specific subject and point of application of the stimulation. The mechanical impedance parameters used to simulate the behavior of the stricken body had to be selected appropriately in order to provide a realistic representation of the body sway during the impact phase. On the other hand, more refined models, as the one presented in section 1.1.3, would be necessary to get a detailed description of the response occurring after the impact, hence when active response overlaps passive one. For this modeling, however, a better understanding of the muscles involved as well as on their level of activation would be required.

As detailed above, the movement of the stricken body was modeled as a single DoF sliding along the antero-posterior direction. A single inverted pendulum structure, as the one used to model human postural response in most of the studies, is used to model postural reaction as a simple rotation about the ankle joint. Since the motion of the mass M_2 was translational, an equivalence between that and the whole mass and inertia of a subject's body in a single inverted pendulum model can be estimated to get more realistic values of the parameters used to define the subject's mechanical impedance. In particular, it was fundamental to ensure that the stricken body would move similarly to the body CoM, hence with the same order of magnitude of CoP displacement as measured by force plate during experimental trials. A scheme of PGAS model is presented in Fig. 4.1.

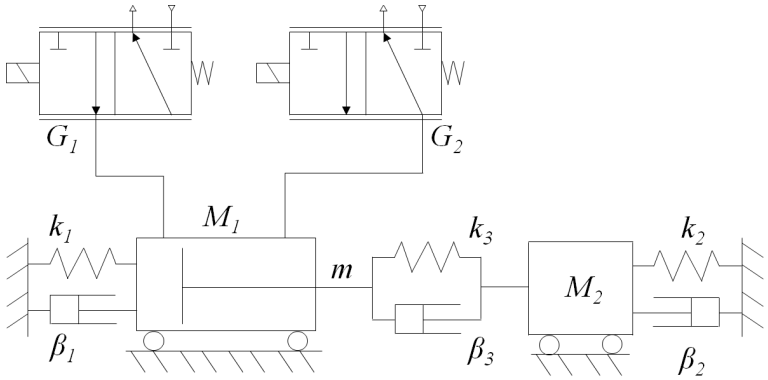

Figure 4.1: Model of Perturbation Generation and Analysis System; descriptions of the parameters are reported in Table 4.1.

4.1.2 Valves

Each flow proportional valve was modeled according to the ISO 6358, thus as a pneumatic resistance defined by a sonic conductance C and a critical ratio b. Each valve had different upstream and downstream pressures depending on the direction of the air flow. For instance, when the piston was extended, the valve connected to the rear chamber had the supply pressure P_s set as the upstream pressure and the pressure P_1 (measured inside the rear chamber) as the downstream one. Assuming P_A and P_B as general upstream and downstream pressures, flow rate G was calculated with the following equations in sonic and subsonic conditions:

$$G = \rho_0 P_A C \text{ for } 0 < \frac{P_B}{P_A} \leq b \tag{4.1}$$

$$G = \rho_0 P_A C \sqrt{1 - \left(\frac{P_B/P_A - b}{1 - b}\right)^2} \text{ for } b < \frac{P_B}{P_A} \leq 1 \tag{4.2}$$

Flow rate calculated with Eqs. 4.1 and 4.2 was assumed positive when directed towards the actuator and negative when opposite. Conductance C also remained not constant during operation, since it depended on the sectional area regulated by the valve. Even if more detailed models of valve internal dynamics are available, based on the knowledge of the internal components and working principles of the device, a simplified approach was chosen to express the relationship between the conductance and sectional area, hence between the conductance and the voltage command. The relationship between the variation of effective sectional area and voltage command V_{ref} was assumed linear, as to the relationship between the conductance and the sectional area. These approximations led to the following equation:

$$C = K_v V_{ref} \tag{4.3}$$

in which K_v is the static flow gain of the valve, expressed as:

$$K_v = \frac{C_{max}}{V_{max}} \tag{4.4}$$

Equation 4.3 shows the static relationship between the voltage command and the conductance. Then, a first order dynamics was implemented to take into account the dynamic effect of conductance variations related to the voltage command:

$$C = \frac{K_v}{1 + \tau s} V_{ref} \tag{4.5}$$

4.1.3 Double acting pneumatic cylinder

Regarding the pneumatic cylinder, it was modeled considering each chamber a tank with variable volume V. The mass flow rate in each chamber was calculated as:

$$G_{in} - G_{out} = \frac{d(\rho V)}{dt} = \rho \frac{dV}{dt} + V \frac{d\rho}{dt} \tag{4.6}$$

Continuity equation 4.6 was used to express the balance between flow rates at the inlet G_{in} and at the outlet G_{out} of the tank. Since any volume variation depended only on the motion of the piston rod, the following equations could be obtained:

$$\frac{dP_1}{dt} = \frac{G_1 n R T_{1i}}{A_1 (x_0 + x_{m1} + x_3)(P_1/P_{1i})^{\frac{1-n}{n}}} - \frac{P_1 n}{x_0 + x_{m1} + x_3} \frac{dx_3}{dt} \tag{4.7}$$

$$\frac{dP_2}{dt} = \frac{G_2 n R T_{2i}}{A_2 (x_l - x_0 + x_{m2} - x_3)(P_2/P_{2i})^{\frac{1-n}{n}}} + \frac{P_2 n}{x_l - x_0 + x_{m2} - x_3} \frac{dx_3}{dt} \tag{4.8}$$

Subscripts 1 and 2 in Eqs. 4.7 and 4.8 refer respectively to rear and front chambers of the cylinder. A_1 and A_2 represent the sectional area of each chamber that were subjected respectively to the absolute pressures P_1 and P_2. The variable x_3 was assigned to the stroke of the piston rod, i.e. the relative position of the piston with respect to the cylinder tube. A_1 and A_2 were different since the selected actuator was not a through rod type. Therefore, piston cross-sectional area had to be subtracted from the cylinder tube sectional area to compute A_2 correctly. Other parameters included in Eqs. 4.6 to 4.8 have been all collected in Table 4.1.

Dynamic equilibrium of the piston was evaluated with the following equation (Fig. 4.2):

$$m \left(\frac{d^2 x_3}{dt^2} + \frac{d^2 x_1}{dt^2} \right) + \gamma \frac{dx_3}{dt} + F_e + p_2 A_2 - p_1 A_1 + F_{fr}\ sign \left(\frac{dx_3}{dt} \right) = 0 \tag{4.9}$$

Since x_1 represented the motion of cylinder tube, $x_1 + x_3$ corresponded to the

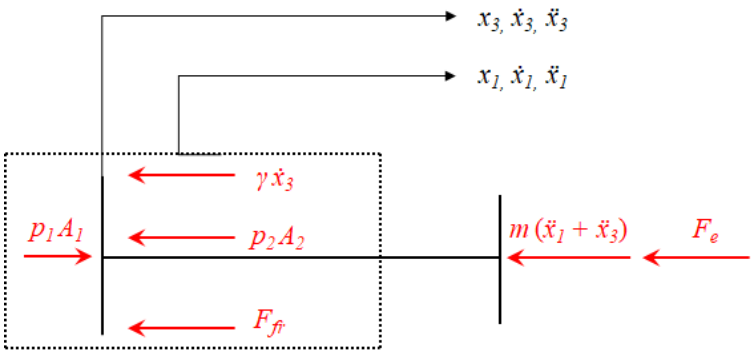

Figure 4.2: Free body diagram of actuator's piston, dot notation for time derivative.

absolute position of the piston rod. p_1 and p_2 represented the relative pressures in rear and front chambers, computed as:

$$p_1 = P_1 - P_{atm}, \; p_2 = P_2 - P_{atm} \tag{4.10}$$

Dynamics of the whole actuator was evaluated by equilibrium of all external forces (Fig. 4.3) and was affected by the visco-elastic constraint provided by the operator (expressed by the constants k_1 and β_1):

$$m\left(\frac{d^2x_3}{dt^2} + \frac{d^2x_1}{dt^2}\right) + M_1\frac{d^2x_1}{dt^2} + k_1x_1 + \beta_1\frac{dx_1}{dt} + F_e = 0 \tag{4.11}$$

The force exerted on the piston, given by the impact with the stricken body, was

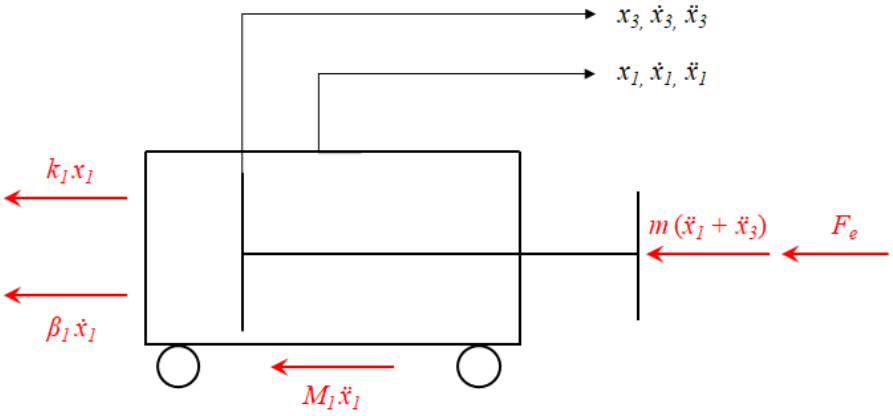

Figure 4.3: Free body diagram of the pneumatic actuator, dot notation for time derivative.

expressed as F_e (Eqs. 4.9 and 4.11). The magnitude of this contact force depended

on the dynamics of the cylinder frame (Eq. 4.11) and of the stricken body (Eq. 4.14), as well as on the characteristics of the deformable end pad used to distribute the contact pressures on a wider surface (Eq. 4.12).

4.1.4 Deformable end pad

As pointed out above, the external force F_e, i.e. the perturbation force, depended also on the characteristics of the deformable pad located at the extremity of the piston rod and used to directly contact the body of the subject. Since the AP could only push the subject, this compressive force was related to the crushing of the foam used to cover the end striker, as well as to the gradient of such deformation. For these reasons, the interface was modeled as a visco-elastic buffer with parameters k_3 and β_3, i.e. as a Kelvin-Voigt material, similarly to the operator's action on the perturbator. The relationship used to express F_e was the following (see Fig. 4.4):

$$F_e = k_3(x_3 + x_1 - \Delta x - x_2) + \beta_3 \left(\frac{dx_3}{dt} + \frac{dx_1}{dt} - \frac{dx_2}{dt} \right) \tag{4.12}$$

in which Δx represented the initial distance between the end striker and the stricken body, whose displacement (with respect to the initial resting condition) was x_2. In the model, it was necessary to set a condition that allowed for the correct identification of the contact phase, as given by Eq. 4.13:

$$F_e \neq 0 \text{ if } x_3 + x_1 \geq \Delta x + x_2 \tag{4.13}$$

4.1.5 Dynamics of the stricken body

As discussed in section 4.1.1, the body of the subject was modeled as a passive system, therefore as a mechanical impedance defined by the parameters M_2, k_2 and β_2. Since only antero-posterior perturbations were considered, the oscillation in the horizontal direction was evaluated by dynamic equilibrium (Fig. 4.5) of the mass as presented in the following equation:

$$M_2 \frac{d^2x_2}{dt^2} + \beta_2 \frac{dx_2}{dt} + k_2 x_2 = F_e \tag{4.14}$$

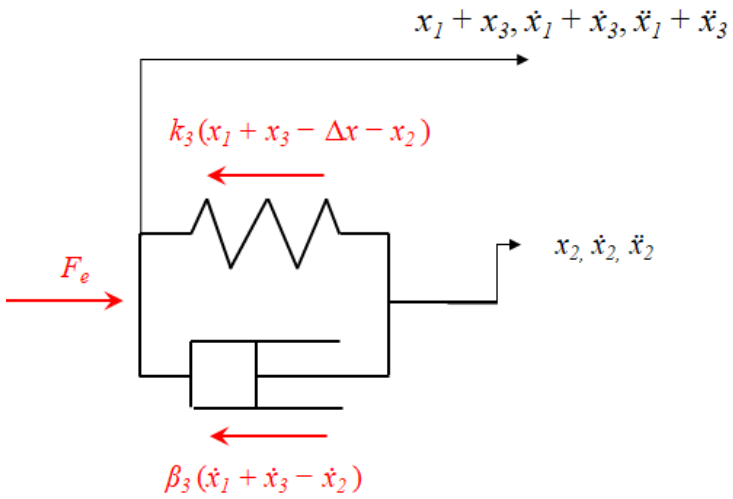

Figure 4.4: Free body diagram of deformable pad, dot notation for time derivative.

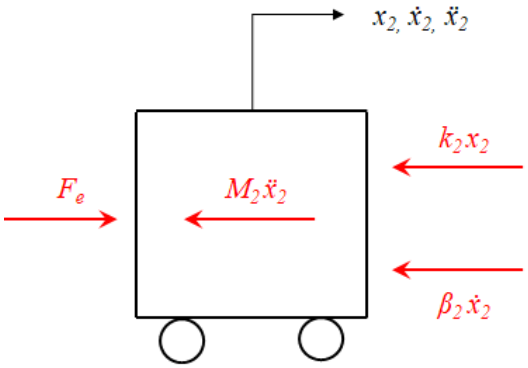

Figure 4.5: Free body diagram of stricken body, dot notation for time derivative.

4.2 Model validation

In order to support the use of the analytical model, it was necessary to validate it by comparison with the results given by the experimental system. The default actuator considered was the ISO 6432, controlled by 3AF2 valves with direct force feedback during impact. Parameters of actuators and valves are reported in Tables 5.1 and 5.2. The aim of this validation process was to verify that the model could match the actual behavior of the system with good accuracy and reliability. The unknown data, as the coefficients C_{max} and b needed to define the valve model, were extracted from characterization trials, whereas the other parameters were obtained from the datasheets of the components (e.g. size of the actuator). The main parameters implemented in the model are presented in Table 4.2.

Parameter	**Value**
Stricken body mass	10 kg
Supply pressure	3.5 bar
Static friction force	20 N
Kinetic friction force	15 N
Velocity limit	10^{-6} m/s
V_{rear} - approach phase	5.6 V
V_{front} - approach phase	4 V
V_{rear} - return phase	0 V
V_{front} - return phase	6.2 V
Operator stiffness k_1	30 kN/m
Operator damping β_1	1 kN s/m
Subject stiffness k_2	3 kN/m
Subject damping β_2	1 kN s/m
End pad stiffness k_3	10 kN/m
End pad damping β_3	0 N s/m
Initial distance Δx	80 mm

Table 4.2: Main parameters used for model validation.

As shown in Table 4.2, valves command voltages V_{rear} and V_{front} were fixed during approach and return phases, since the motion of the piston rod was open-loop controlled during those phases. Force control during impact was performed by means of a simple PI controller. A Coulomb model was chosen for the description of friction related to piston sliding. The parameters k and β were selected by iterative procedure to match the experimental behavior and to get consistent results about deformation of the damping pad interface. The controller gains were similarly estimated by semi-empiric iterative approach (Ziegler-Nichols).

Reference force signal was a smooth function given by a sine wave period plus

a constant bias, with predefined peak-to-peak amplitude and duration. This reference was chosen to avoid fast transients in the force error signal. However, a step reference signal would have likely given similar results with a different choice of the controller gains. Typical amplitude of the perturbation force was 50 N and its duration was 300 ms, yielding a reference impulse equal to 7.5 N s.

The system was tested in three different configurations, defined as follows:

A) AP and stricken body fixed;

B) AP fixed and stricken body free to move;

C) AP and stricken body free to move.

For each configuration, the performance of the AP was compared with the corresponding results of the model. Figure 4.6 presents the effect of different k_p (proportional gain) on the force tracking performance of the controller. Ziegler-Nichols methods was used for a first assessment of k_p, then it had to be finely tuned to avoid oscillations in the control law and to reduce the time-to-peak. On the other hand, the integral gain k_i only slightly affected the results whereas the system was far more sensitive to variation of k_p. This behavior was confirmed by both experimental and model results and can be explained by the lack of a steady-state for the controller to track, since the reference force signal was impulsive. For such short lasting perturbations, tuning of proportional gain was far more relevant since it directly affected the responsiveness of the controller to sudden variations in the force error. However, for the optimal tuning of the controller, integral term should not be neglected a priori, since it can improve peak force accuracy.

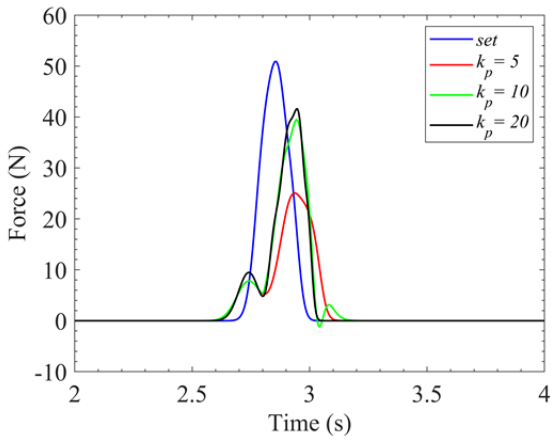

Figure 4.6: Effect of proportional gain k_p on the system behavior [74].

Unfortunately, the model did not perform in a realistic way when the same controller gains were used in both the model and the experimental system. In particular, the contact force profiles obtained in the model had significantly lower amplitude with respect to the experimental ones. This result was confirmed for all the configurations under analysis (A, B and C). To get a better approximation of the real system, it was necessary to manually tune the proportional gain iteratively, yielding to a larger value (about 10 times greater) of k_p in the model with respect to the one used in the test-bench trials. As highlighted in Fig. 4.7, after tuning of the controller, matching between model and experimental system increased noticeably. Even if the accuracy of force tracking was low, as expected since low performance

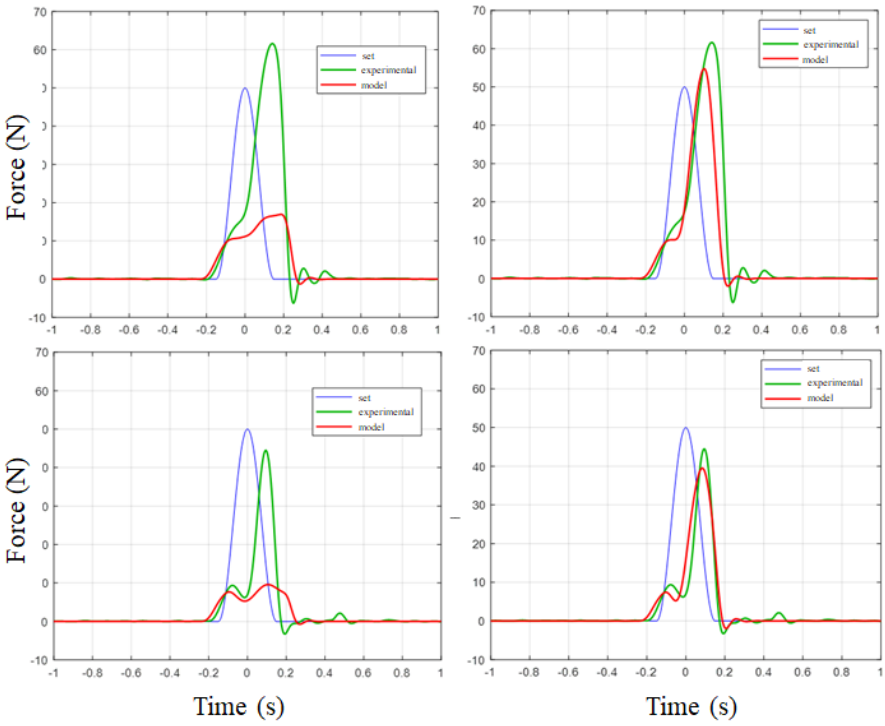

Figure 4.7: Effect of proportional gain scaling on model accuracy in different configurations (top: A; bottom: B) for different k_p (left: $k_p = 1.5$; right: $k_p = 10$) [74].

valves and actuator had been selected for validation, the conformity between force profiles obtained became substantially stronger. Particular behaviors as the initial oscillation in the contact force profile (configuration B) were highlighted in the model as well as during experimentation in laboratory. The need for a scaling factor on k_p could be due to the inaccurate modeling of some aspects as friction forces or pneumatic resistance of pipes used to connect valves and actuator. Moreover, some features as the friction model chosen for the piston rod were only approximated for

the lack of data and for sake of simplicity. However, the model showed good level of accuracy and could be used to predict the behavior of the real system.

4.3 Control logic design

The first AP prototype was based on the direct control of the contact force exerted during the perturbation. The only signal used to close a force feedback was the one given by the load cell positioned at the extremity of the end striker of the perturbator. Since the performance obtained with this first control architecture were not sufficient to guarantee accurate force tracking, different solutions were investigated thanks to the modeling of the physical system.

As presented in Eqs. 3.1 and 3.2, valve commands were expressed as function of force error and of its time integral (PI controller). These relationships referred only to the phase corresponding to the impact. The same organization, based on the sequence of four phases, i.e. idle, approach, strike and return, was selected for the model as well as for the systems and prototypes presented in the following chapters. With respect to the first AP prototype, different solutions for motion and force control during the several phases were investigated.

4.3.1 Different control solutions during approach phase

In the first prototype, the AP was open-loop controlled during approach phase. Valves regulating the flow to the actuator's chambers were controlled by means of fixed voltage command signals. Such constant signals were selected iteratively, in order to find the best compromise between the accuracy of force control and duration of the stimulus. In order to improve the performance of the system, and to exclude any effect given by the operator's skill and by different initial positioning of the perturbator with respect to the body of the subject, closed-loop control solutions were investigated to regulate the motion of the piston during approach phase with higher accuracy and reliability. The following solutions were considered:

- force control;
- motion control at defined speed.

Force control during approach

In the first solution, the control logic had to follow a force reference also during the approach phase, in addition to the one given during strike phase. Since the load cell did not measure any force until the contact occurred, the force error indirectly drove the piston rod to extend. The magnitude of force reference during approach was set to get the desired dynamics of the piston rod. In most of the simulations,

a 5 N constant signal was used as reference one, and a simple PI controller was used to drive the system. Although the system was closed-loop controlled during approach phase, this solution did not allow for the direct control of piston motion. Therefore, expression of V_{rear} and V_{front} during approach phase were the same as presented in Eqs. 3.1 and 3.2.

Motion control during approach

In this solution, the motion of the piston rod was directly controlled during approach phase. By an experimental point of view, different solutions are available to monitor piston sliding as accelerometers, LVDT, magnetic sensors, potentiometers etc. Among the several possibilities, laser displacement sensors allow for easy and accurate measurements with high dynamics (low response time) in many environments, without the need for demanding signal conditioning and unnecessary loading effect. For this reason, the motion control implemented was based on the piston position feedback, provided by a laser sensor. Displacement reference signal $x_{3,set}$ was computed as time integral of a velocity reference, e.g. a constant one that could enable fast perturbations with about 1 - 1.5 s of free travel before impact. Equations for rear and front valves commands, still based on a PI controller as the one presented in the previous section, were the following:

$$V_{rear}^{'} = k_p^{'}(x_{3,set} - x_{3,measured}) + k_i^{'} \int (x_{3,set} - x_{3,measured})\, dt + V_0 \tag{4.15}$$

$$V_{front}^{'} = -V_{rear}^{'} + V_0 \tag{4.16}$$

Similarly to the other solutions adopted, this one still considered a force threshold to drive the system from approach phase to the strike one. Different solutions of force control during strike phase will be discussed in the next section.

4.3.2 Force control during strike phase based on sliding mode controller

In the first AP prototype, force feedback control was used to regulate the contact force during strike phase. Control architecture was based on a simple Proportional-Integral controller, that was tuned iteratively to get accurate enough results. However, even if the system could perform well in characterization trials, first analyses on healthy subjects with the AP showed very limited performance, especially regarding the accuracy of force tracking (section 3.5). Repeatability of the perturbations was instead adequate to the application. Although force control accuracy was clearly influenced by the low performance of the actuator and valves selected, respectively for the presence of high friction and for large response timing, more advanced control techniques could be tested thanks to the model to investigate their effect on the general performance of the system.

In addition to simulations based on the control logic presented in section 3.3, a second architecture based on a non-linear model-based controller was tested. The new architecture was based on sliding mode control [65], whose implementation will be here presented.

Definition of sliding mode control

Model-based controllers as sliding mode control can provide better performance with respect to commonly used linear controllers in many contexts where non-linear phenomena such as friction are relevant. This particular controller has been already implemented in systems based on pneumatic or hydraulic actuation, as discussed in section 1.2.2. It is based on the definition of a sliding surface variable called s_F that represents a function of the error e_F. This error variable depends on the specific physical quantity to regulate. In this particular application, it was represented by the perturbation force error, expressed as:

$$e_F = F_e - F_{set} \tag{4.17}$$

The expression of sliding surface was given by the following equation:

$$s_F = \left(\lambda + \frac{d}{dt}\right)^{q-1} e_F \tag{4.18}$$

The tracking of force reference ($e_F = 0$) was performed by remaining on the sliding surface for any $t > 0$, therefore controlling the system in sliding mode condition ($s_F = 0$) [65]. The parameter λ in Eq. 4.18 was defined arbitrarily and related to the dynamics of the error e_F. The q parameter was equal to the order of the differential equation that related the input and output of the controller. In this system, this parameter can be computed as follows.

Order of input - output differential equation of the controller

Starting from Eq. 4.9, it was necessary to differentiate the equation to get the first derivative of the pressures p_1 and p_2:

$$m\left(\frac{d^3x_3}{dt^3} + \frac{d^3x_1}{dt^3}\right) + \gamma\frac{d^2x_3}{dt^2} + \frac{dF_e}{dt} + \frac{dp_2}{dt}A_2 - \frac{dp_1}{dt}A_1 + \frac{dF_{fr}(t)}{dt} = 0 \tag{4.19}$$

To simplify the equation, any term related to friction and air viscosity was neglected. Moreover, they could not be measured directly during experimentation, hence they had to be estimated or completely removed by Eq. 4.19 for the practical implementation of the controller. Similarly, third derivative of tube and piston rod position could not be feasibly computed due to the errors produced by numerical differentiation. For this reason, an approximated version of Eq. 4.19 was obtained:

$$\frac{dF_e}{dt} = \frac{dp_1}{dt}A_1 - \frac{dp_2}{dt}A_2 \tag{4.20}$$

Equation 4.20 shows the relationship between first derivatives of the external force and of the pressures inside the chambers of the actuator. Any term removed from Eq. 4.19 represented a *modeling noise* that was tackled by the definition of the control law, which could be designed to mitigate any discrepancy in the modeling due to approximations.

Equation 4.20 can be combined with Eqs. 4.7 and 4.8 to get the flow rates G_1 and G_2. To ease the formulation, Eqs. 4.1 and 4.2 was rewritten using the following form:

$$G = \rho_0 C f(P_A, P_B, b) = C\psi(P_A, P_B) \tag{4.21}$$

in which the function ψ depended on the critical ratio b (see Eqs. 4.1 and 4.2). This function assumed different values when the piston was extended and when it was retracted, since upstream and downstream pressures varied. For instance, when the piston was extended, $\psi_1 = \psi(P_s, P_1)$ and $\psi_2 = \psi(P_2, P_{atm})$. P_A and P_B in Eq. 4.21 represent respectively the upstream and downstream pressures. Substituting Eq. 4.21 in Eqs. 4.7 and 4.8, assuming the transformation as isothermal for simplicity ($n = 1$), yielded:

$$\frac{dP_1}{dt} = \frac{dp_1}{dt} = \frac{C_1\psi_1 nRT_{1i}}{A_1(x_0 + x_{m1} + x_3)} - \frac{P_1 n}{x_0 + x_{m1} + x_3}\frac{dx_3}{dt} \tag{4.22}$$

$$\frac{dP_2}{dt} = \frac{dp_2}{dt} = \frac{C_2\psi_2 nRT_{2i}}{A_2(x_l - x_0 + x_{m2} - x_3)} + \frac{P_2 n}{x_l - x_0 + x_{m2} - x_3}\frac{dx_3}{dt} \tag{4.23}$$

Since valves were controlled symmetrically, Eqs. 3.1 and 3.2 were rewritten in the following way, assuming $V_{ref} = u$:

$$V_{rear} = u + V_0,\ V_{front} = -u + V_0 \tag{4.24}$$

Only the symmetrical part u of the command voltages affected the conductance of the valves, since a voltage equal to V_0 corresponded to the zero position (no flow). Therefore, u represented the actual control input of the system. If valve time constant τ_v is small, first order dynamics could be neglected and a static relationship (Eq. 4.3) could be found between the conductance of each valve and the control input u:

$$C_1 = K_v u,\ C_2 = -K_v u \tag{4.25}$$

Substituting Eq. 4.25 in Eqs. 4.22 and 4.23, and combining the latter with Eq. 4.20, the following equation was obtained:

$$\frac{dF_e}{dt} = -\left(\frac{P_1 A_1}{x_0 + x_{m1} + x_3} + \frac{P_2 A_2}{x_l - x_0 + x_{m2} - x_3}\right)\frac{dx_3}{dt} + K_v RT_i\left(\frac{\psi_1}{x_0 + x_{m1} + x_3} + \frac{\psi_2}{x_l - x_0 + x_{m2} - x_3}\right)u \tag{4.26}$$

in which the same initial temperature T_i was considered for both chambers. Equation 4.26 was rewritten in the following form:

$$\frac{dF_e}{dt} = f(\mathbf{x}) + p(\mathbf{x})u \tag{4.27}$$

in which $\mathbf{x}$ represented the vector including the variables needed to define the state of the system (P_1, P_2, x_3) and some of the parameters necessary to compute the functions $f(\mathbf{x})$ and $p(\mathbf{x})$. The formulation of Eq. 4.27 highlighted the relationship between the external force F_e, that is the physical quantity to control, and the actual control input u. The order of this differential equation ($q = 1$) was required for the definition of the sliding surface.

Design of the control law

Equation 4.18, for $q = 1$, yielded the following expression for the sliding surface:

$$s_F = \left(\lambda + \frac{d}{dt}\right)^0 e_F = e_F = F_e - F_{set} \tag{4.28}$$

Sliding mode theory defines the control law, that is necessary to keep the system in sliding condition ($s = 0$), in the following form:

$$u = u_{eq} + \overline{u} \tag{4.29}$$

Equation 4.29 shows that the control law must include two separate contributions: u_{eq} is called equivalent control input and comes directly from the modeling of the physical system. It was evaluated by first derivative of s_F as follows:

$$u_{eq} = u\big|_{\frac{ds_F}{dt}=0} \Rightarrow \frac{ds_F}{dt} = \frac{dF_e}{dt} - \frac{dF_{set}}{dt} = \overline{f(\mathbf{x})} + \overline{p(\mathbf{x})}u_{eq} - \frac{dF_{set}}{dt} = 0 \tag{4.30}$$

Solving Eq. 4.30 yielded the expression of equivalent control input u_{eq} (Eq. 4.31).

$$u_{eq} = \frac{\dfrac{dF_{set}}{dt} - \overline{f(\mathbf{x})}}{\overline{p(\mathbf{x})}} \tag{4.31}$$

The functions $\overline{f(\mathbf{x})}$ and $\overline{p(\mathbf{x})}$ can be computed if the state variables required are available or can be estimated as accurately as possible. Since the model could only partially match the real system behavior, due to several approximations, the equivalent control input did not correspond to the optimal one. Therefore, the system only approached the sliding mode condition when $u = u_{eq}$. For this reason, an additional term $\overline{u}$ was required (see Eq. 4.29). This contribution, i.e. the switching control input, forces the system to reach the sliding mode condition.

Since it was implemented through a fast switching function (as *sign*), it could induce chattering (i.e. fast oscillations in the control law). To reduce this effect, a smoother function as the *sat* (saturation) one was used effectively, which is defined as follows:

$$\overline{u} = -\frac{K_{smc}}{\overline{p}(\mathbf{x})} sat\left(\frac{s_F}{\delta}\right) \tag{4.32}$$

in which K_{smc} was the controller gain and δ was a constant parameter used to regulate the switching frequency of the control logic. *sat* function was defined as follows:

$$sat\left(\frac{s_F}{\delta}\right) = \frac{s_F}{\delta} \text{ if } 0 \leq |s_F| < \delta,\ sat\left(\frac{s_F}{\delta}\right) = sign(s) \text{ if } |s_F| \geq \delta \tag{4.33}$$

Piston rod excursion as well as the internal actuator pressures were required to compute the control input u, since they were included in $\overline{p(\mathbf{x})}$. Even though the actuator stroke could be easily monitored (e.g. by means of a linear potentiometer), internal pressures would have required specific sensors to be measured. For this reason, in the following section a methodology for the estimation of pressure inside actuator's chambers is presented.

Estimation of the unknown pressures

The methodology here presented and implemented in the model has been formerly reported in [70]. Pressures P_1 and P_2 can be estimated considering the average pressure P_{ave} in the actuator during operation, defined as follows:

$$P_{ave} = \frac{P_1 A_1 (x_0 + x_{m1} + x_3) + P_2 A_2 (x_l - x_0 + x_{m2} - x_3)}{A_1 (x_0 + x_{m1} + x_3) + P_2 A_2 (x_l - x_0 + x_{m2} - x_3)} \tag{4.34}$$

P_{ave} could be estimated from simulations or set approximately as constant (e.g. $P_s/2$). By combination of Eq. 4.34 with Eq. 4.9, it was possible to estimate the values of P_1 and P_2. Since viscous and friction terms in Eq. 4.9 were generally unknown, as well as the inertial term, it was possible to simplify the expression of Eq. 4.9 in order to get a static relationship between F_e and absolute pressures P_1 and P_2. This approximation can provide realistic results especially for low inertia and low friction systems.

This technique was used to effectively implement sliding mode control in the model of automatic perturbator. As stated by the Authors in [70], the methodology discussed cannot ensure an accurate estimation of the unknown pressures, but it can be useful to provide a realistic approximation of such variables without increasing the complexity of the system (e.g. by implementation of additional transducers). Moreover, the switching control input $\overline{u}$ is designed to take into account discrepancy in the model such as the one due to the inaccurate estimation of the internal pressures. As an alternative, a model running in parallel with the experimental system could be designed to estimate the unknown quantities required by the control logic (Hardware-in-the-Loop approach).

Chapter 5

Test-bench design and model simulations

5.1 Design of the test-bench

In order to identify all hardware and software requirements necessary to achieve the desired performance, an experimental test-bench that matched the PGAS and its model (see section 4.1) was developed. The three main parts of the system, hence the operator, the AP and the subject, were all taken into account by including corresponding elements in the test-bench. Similarly to the model, the motion of each part was reduced to a single DoF, therefore only antero-posterior perturbations were considered. In the model, the operator acted as a visco-elastic constraint that limited the oscillations of the AP. At the same time, the stricken body was also modeled as a passive system and represented by a mechanical impedance. The same idea was applied to the design of the experimental test-bench: the AP was fixed on a sliding cart and constrained by a custom-made visco-elastic damper. Moreover, the stricken body consisted in a mass fixed on another cart, the latter constrained by a second visco-elastic damper. In this way, it was possible to replicate the condition already presented in the model that could match the real system with good accuracy.

The test-bench was assembled by means of both commercial and custom-made components, as visco-elastic dampers. In particular, the two carts were realized with commercial low friction linear guides. Each cart had a couple of supports sliding on two parallel binaries. The linear guide (C-SHR28-1000-B4, MISUMI Europa GmbH, Germany) was 1 m long and meant for average/large loads (5.1 kN of dynamic load coefficient, for each support). The AP was fixed on one cart, while the stricken body mass was placed on the other one. Custom 3D printed flanges were used to fix the actuator on the cart. The AP shared the same architecture used for the first prototype, therefore it was equipped with a uniaxial load cell to measure the contact force. The handles were removed to ease the assembly of the

AP on the cart, whereas the valves were still placed directly on top of the actuator. The stricken body cart was equipped with a fixed metal plate used as a target for the AP. A render of the rig is presented in Fig. 5.1, whereas Fig. 5.2 shows the actual test-bench.

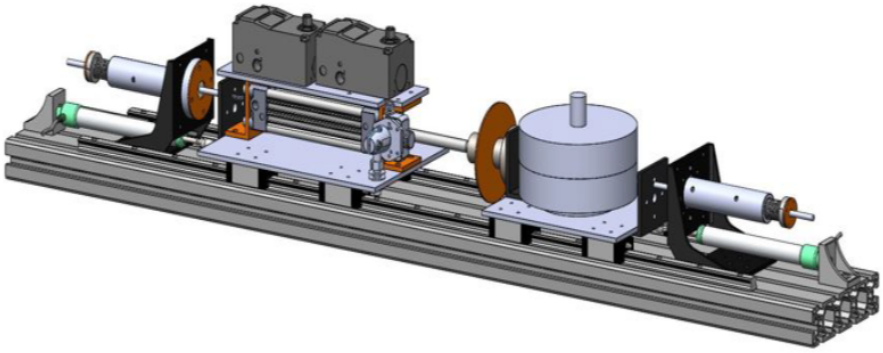

Figure 5.1: Render of test-bench.

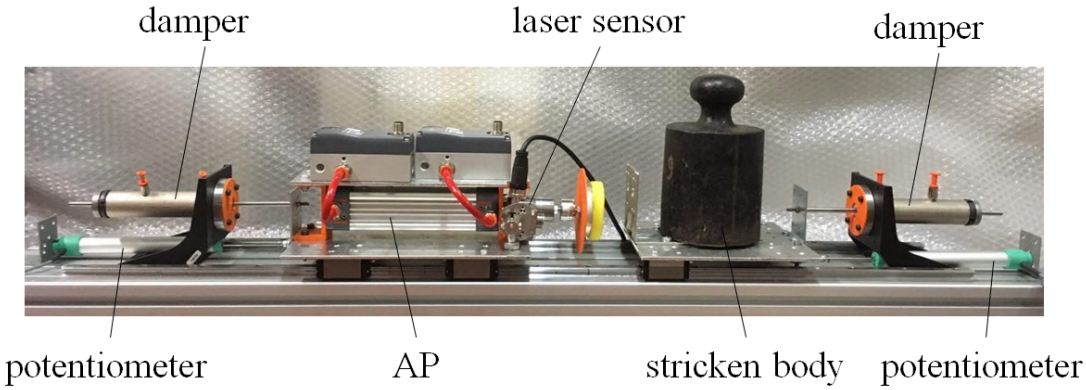

Figure 5.2: The experimental test-bench.

In order to measure the positioning of the carts, two linear potentiometers (PZ-34-A-100, Gefran S.p.A, Italy) were embedded in the test-bench (see Fig. 5.2). Each sensor was mounted and connected to its cart by means of a ball joint, to take into account any misalignment between the transducer and the longitudinal direction of the linear guide. The range of each sensor (100 mm) was selected to match the expected oscillations of both carts, hence respectively of the operator and of the stricken body. Moreover, since it was necessary to measure the stroke of the actuator (i.e. the relative position of the rod with respect to the tube) for monitoring and control purposes, the test-bench was equipped with a laser displacement sensor (Q4XTULAF300-Q8, Banner Engineering Corp., USA). This

transducer is able to get precise measurements in a range between 25 mm and 300 mm and can be calibrated opportunely to provide a linear relationship between the displacement of the target and the output voltage (between 0 and 10 V). The sensor was fixed to the cylinder frame, therefore it was integral with the tube (Fig. 5.2). A 3D printed plastic circular plate was mounted at the extremity of the piston rod (near the load cell) and used as a moving target for the laser sensor.

The control logic, as well as the signal acquisition and processing, was still based on a real-time system (dSPACE GmbH, Germany), similarly to the first AP prototype. However, a second solution was developed and based on a recent system (by Speedgoat GmbH, Switzerland, Fig. 5.3) equipped with two IO 183 modules (4 differential 16-bit analog inputs, 4 16-bit analog outputs, 100 kHz maximum aggregate sample rate for each module) + two IO 397 modules (4 differential simultaneous sampling 16-bit analog inputs, 4 16-bit analog outputs, 200 kHz maximum sample rate, FPGA-based, for each module). This system was programmed in Simulink®

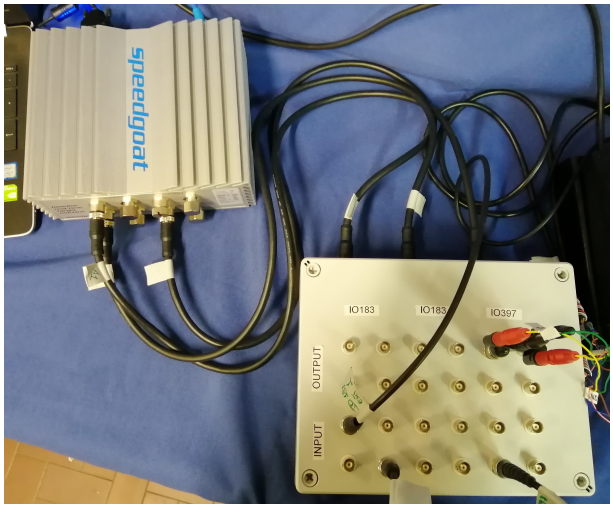

Figure 5.3: Real-time system (Speedgoat GmbH, Germany) and terminal box.

similarly to the first one, however it allowed for more efficiency and flexibility with respect to the dSPACE system. The core of this system was a Baseline real-time target machine Education, provided with terminal boards for signal input-output. A custom panel equipped with BNC connectors was fabricated to ease the acquisition of sensors data and to provide a comfortable interface for valve command signals generation (Fig. 5.3).

As presented above, custom visco-elastic dampers (Fig. 5.4) were designed and fabricated in order to restrain the motion of both carts and to match the natural oscillations of the operator or of the stricken body. With respect to the zero position (corresponding to half the stroke of the damper), each device allowed for limited sliding in a $\pm$ 30 mm range. They also had to be adjustable since different stiffness and damping could be needed to achieve the required response. Each damper

consisted of an external fixed tube (about 130 mm long) and a piston that was integral with its respective cart (see Fig. 5.2). Two identical springs acted in

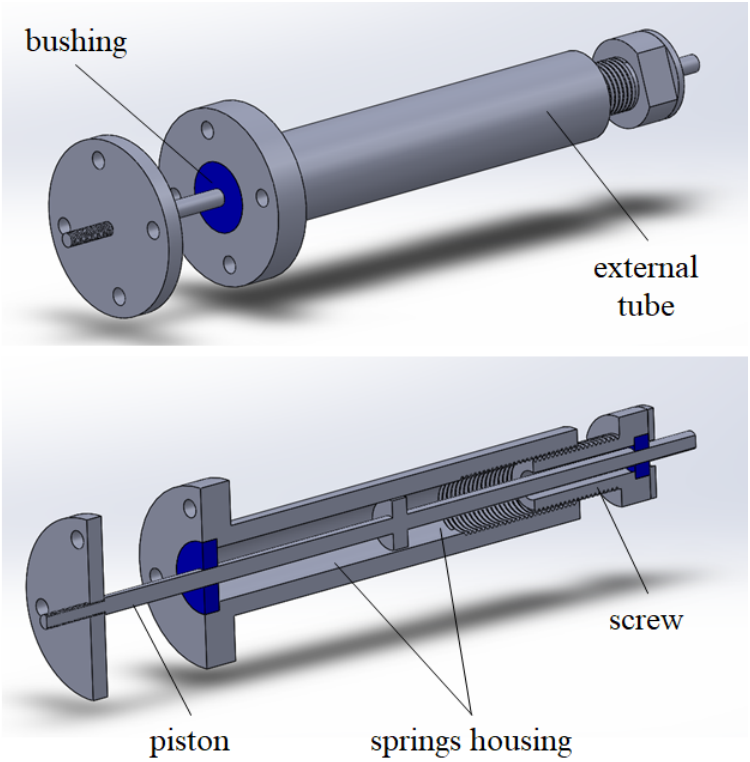

Figure 5.4: Custom-built visco-elastic damper.

parallel to ensure the zero position of the damper, then a cover plate and a flange were mounted to hold the springs in position. Each damper's tube was threaded and allowed for setting different spring pre-load and damper stroke by means of a regulation screw. By varying the initial length of the springs, a different stroke of the damper could be selected. Stiffness could be varied by means of different springs. Two nylon bushings were placed at both ends to support the piston and to reduce friction during sliding. On the cylindrical surface of the tube, two holes were realized, one for each damper's chamber. In this way, by connecting adjustable pneumatic resistances, it is possible to modulate the damping effect of the device. This regulation, as for the stiffness adjustment provided by the screw, was necessary to achieve the desired behavior of the mechanical impedances considered (i.e. of the operator or of the stricken body). The spring implemented in the test-bench had stiffness approximately equal to 0.7 N/mm and length at rest equal to 94 mm.

5.2 Components selected for the final AP

In this section, new components selected and tested with the experimental rig are shown. Since the architecture of the AP was not changed, different actuators and valves were considered to improve the performance of the device. The same test-bench would easily allow for different solutions to be tested, e.g. based on electric or electro-mechanical actuators.

5.2.1 Pneumatic cylinders

The pneumatic cylinder used in the first AP prototype (ISO 6432) was a low cost one, mainly chosen for its large availability and ease of implementation. However, it showed very limited performance in force tracking accuracy, calling for actuators with improved performance. For this reason, two commercial low-friction double-acting cylinders were selected:

- ISO 15552 (Metal Work S.p.A., Italy), stroke: 120 mm, bore: 32 mm;
- MQM Series (SMC Corporation, Japan), stroke: 100 mm, bore: 25 mm.

Both cylinders were advertised by the manufacturers as high performance actuators with ultra-low friction, thus able to perform with substantial accuracy in demanding applications. However, whereas the first solution used gaskets made of Nitrile Butadiene Rubber (NBR), the second one was a metal seal cylinder and could theoretically perform with negligible friction effects. Both cylinders were able to resist lateral loads and could operate up to 1 MPa (for the ISO 15552 cylinder) and 0.7 MPa (for the MQM cylinder). Dimensions were compatible with the ones of the former ISO 6432 cylinder used in the first AP prototype. The choice of the actuator was still focused on compactness since low magnitude forces with high dynamics were necessary for the application. The parameters of the new actuators are collected in Table 5.1.

Parameter	**ISO 6432**	**ISO 15552**	**MQM**
Piston mass (kg)	0.2	0.18	0.15
Cylinder frame mass (kg)	2.6	3	2.7
Rod diameter (mm)	10	12	10
Cylinder bore (mm)	25	32	25
Dead band (mm)	5	5	2
Stroke (mm)	120	120	100

Table 5.1: Parameters of the pneumatic cylinders selected in the experimental rig.

5.2.2 Valves

Dynamics and accuracy of the AP depended also on the valves. The first AP prototype was based on 3AF2 valves by CKD Corporation that allowed high flow rate but had limited dynamics. Each valve was controlled by an external control driver that had to be located aside (see Fig. 3.4). The same valves were tested with the different actuators described in the previous section on the experimental test-bench. Moreover, a second valve model (LRWD2 Series, Camozzi Automation S.p.A., Italy) was tested, with high flow rate and dynamics, maximum pressure up to 10 bar, flow rate up to 700 l/min ANR. In particular, the response time was particularly low, with step response time equal to 10 ms. The valve had an internal control loop based on Pulse Width Modulation (PWM) and a PID controller that allowed for accurate positioning of the internal spool. Such control was managed directly by the driver electronics that was embedded in the body of the valve. This allowed for a more compact architecture of the AP, since the driver did not have to be placed aside. The parameters of the valves are collected in Table 5.2.

Parameter	**3AF2**	**LRWD2**
Static conductance ($\mathrm{l\,s^{-1}\,bar^{-1}}$)	1.97	1.68
Critical ratio	0.14	0.36
Valve time constant (ms)	10	7
Dead band (V)	0.5	0.2

Table 5.2: Parameters of the valves selected in the experimental rig.

5.2.3 Characterization of the sensors

All the transducers were characterized before implementation in the test-bench. Linear potentiometers were supplied by a 10 V DC voltage and fixed on the bench. The displacement of the sensor rod was measured and related to the change in the output voltage. Four trials were performed in both extension and retraction of the rod. This process allowed for the calculation of the static gain $K_{pot} = 0.1\mathrm{V/mm}$ of the sensor, that showed an optimal linear behavior in the measuring range. Similarly, the laser displacement sensor was calibrated within the actuator stroke range (100 mm): the sensor had a *teach* button that allowed for selecting initial and final limits of the measuring range, that corresponded respectively to zero and full stroke of the actuator. Output voltage of the laser sensor ranged between 0 V and 10 V, therefore the static gain resulted in $K_{opt} = 0.1$ V/mm.

As already done before preliminary analyses carried out with MP and AP (although not discussed before), the load cell was calibrated in compression trials. The force transducer characteristics resulted linear within the working range ($r^2 > 0.99$),

with a static gain of $K_{lc} = 94.33$ N/V. Zero bias error was removed digitally before each acquisition, since it would affect the performance of force tracking during impact.

5.3 Test-bench trials and simulations

In this section, the main outcomes of the trials performed with the new components are presented. Each subsection is focused on a specific aspect under analysis, and supported by comparison between model and experimental results whenever possible. The system was tested in several configurations (as already discussed in section 4.2), that are presented again for clarity:

A) both carts fixed on the linear guide;

B) AP cart fixed and stricken body free to move;

C) both carts free to move.

Not all the configurations were necessarily evaluated for each analysis, and only significant results will be presented and discussed. However, flexibility and adaptability of the test-bench, as well as efficacy of the model, are evidenced by the several aspects examined in the trials presented.

The results presented in Fig. 4.7, which were based on the default selection of components (actuator, valves) already considered for the first AP prototype, clearly showed insufficient accuracy in force tracking as confirmed by preliminary trials on healthy subjects (section 3.5). As expected, the most accurate results were reported for configuration A, that only partially matched the actual conditions of a posturographic task. In particular, by removing the ability to move of both operator and subject, a direct relationship between sliding of the piston rod and the increase in the contact force was established, with a relevant impact of the characteristics of soft interface placed between the striker and the stricken body. However, even in that configuration, the system showed very large response timing and did not allow for selecting short lasting perturbations (up to 250 ms). Since the possibility to exert impulsive stimuli represents one of the main specifications of the AP, due to the necessity to reduce the overlap between the perturbation and the active (musculoskeletal) postural reaction, these first trials confirmed the necessity for components with higher dynamic performance.

The quality of the results was assessed by calculating two parameters, defined as follows:

$$I_{acc} = \frac{|I_e - I_{set}|}{I_{set}} \cdot 100 \tag{5.1}$$

$$E_{tr} = \frac{\int |F_e - F_{set}|\, dt}{I_{set}} \cdot 100 \tag{5.2}$$

I_{acc} was already presented in Eq. 3.3 to interpret the results of preliminary analyses performed with the first AP prototype. I_e represented the impulse (time integral) of the contact force, while E_{tr}, i.e. tracking error, was equal to the percentage cumulative error of force tracking normalized by the reference impulse I_{set}. Whereas I_{acc} allowed for a general assessment of impulse accuracy, E_{tr} was more specific and helped in the evaluation of force tracking precision.

5.3.1 Contact force reference profile

The first analysis focused on the ability of the system to regulate the contact force by choosing several reference profiles. The system was meant to receive any waveform as input, thus it was possible to test its performance in different conditions. Given the application, only impulsive forces were considered, lasting less than 250 - 300 ms, with limited amplitude (50 - 100 N). The two waveforms considered were a square pulse (with step variation of the contact force) and a smoother one, already used in validation trials, that was defined by a sine wave period plus a bias (see Fig. 4.6).

The system was tested in the three configurations allowed by the test-bench (A, B and C), and the results were consistent in all of them. Whereas Fig. 4.7 shows the results obtained with the model and on the test-bench for the first architecture tested (based on the first AP prototype), Figs. 5.5 and 5.6 show force tracking performance for the simulations carried out with the two reference profiles and obtained by considering some of the new components, i.e. ISO 15552 cylinder and LRWD2 valves, whose characteristics are presented in Tables 5.1 and 5.2.

The other parameters required by the model were configured as presented in Table 4.2, except for β_3 and k_2 that were set respectively to 10 N s/m and 1 kN/m. Addition of a damping coefficient for the soft interface modeling was necessary to avoid numerical artifacts due to the oscillations of contact force, whereas stiffness of the stricken body mechanical impedance was lowered (with respect to Table 4.2) in order to get a more realistic excursion of mass displacement (within the range 1 - 8 cm, depending on the amplitude of perturbation force). The same PI controller gains ($k_p = 3$, $k_i = 20$) were used for both reference force profiles and durations of the perturbation.

As highlighted in Figs. 5.5 and 5.6 respectively for perturbations lasting 250 ms and 100 ms, the system showed a good level of force tracking performance when the square wave was selected, while its accuracy worsened when a smooth profile was chosen. In this condition, the model always showed undesired oscillations in the contact force (that was already highlighted in preliminary analysis, see Fig. 4.7) that did not allow for a correct tracking of the smooth force profile, especially at the beginning of the contact phase. Similar oscillations were also highlighted in trials performed using a square pulse as reference profile, however they had a very slight effect on the general performance due to the step variation of the target

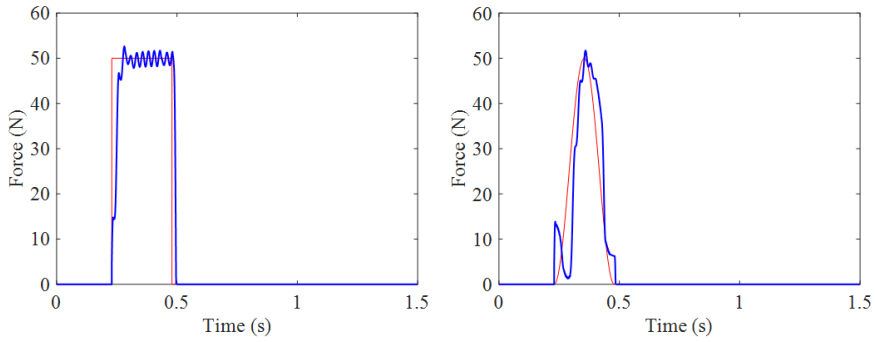

Figure 5.5: Force tracking performance for simulations carried out with two reference profiles lasting 250 ms with 50 N amplitude.

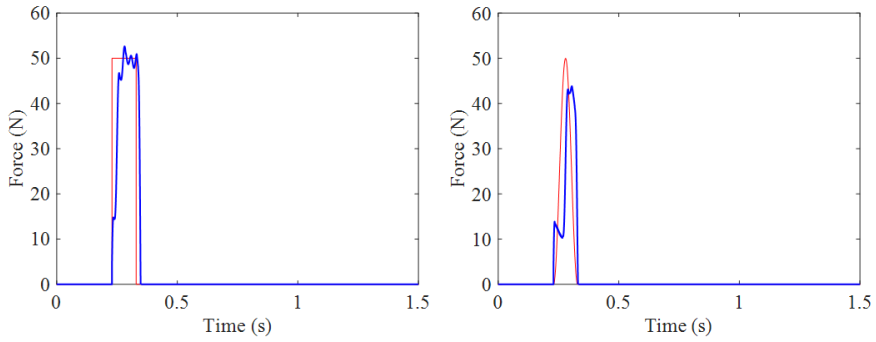

Figure 5.6: Force tracking performance for simulations carried out with two reference profiles lasting 100 ms with 50 N amplitude.

force.

The oscillation of the contact force at the beginning of the impact depended on the velocity of the former. This observation was confirmed by simulating the behavior of the system when the perturbator was driven with higher speed during the approach phase. The contact force represented in Fig. 5.7 showed indeed a first oscillation with higher amplitude (with respect to the one presented in Fig. 5.5) and even worse performance, since a detachment between perturbator and stricken body occurred (signaled by the fall of the contact force). *Bounce* of the interaction force was due to the controller action: since the measured force raised quickly and easily exceeded the set profile during initial contact, the actuator was forced to retract and subsequently lost contact with the stricken body.

With respect to the data presented in validation trials (section 4.2), simulations presented in this section showed significantly improved performance thanks to the model parameters matching new components. This allowed for selecting perturbations lasting less than 150 ms, as shown in Fig. 5.6 for 100 ms stimulus. Even

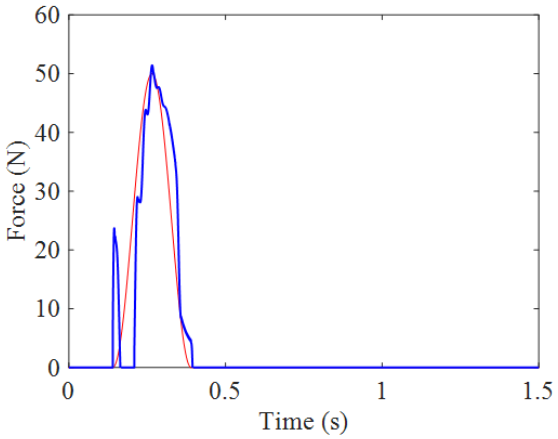

Figure 5.7: Force tracking performance for simulations carried out by driving the piston at higher speed before impact.

perturbations that lasted about 50 ms were tested and will be shown in the following sections. At the same time, perturbations with higher amplitudes (> 50 N) were also tested, as presented in Fig. 5.8. Similarly to the results presented above,

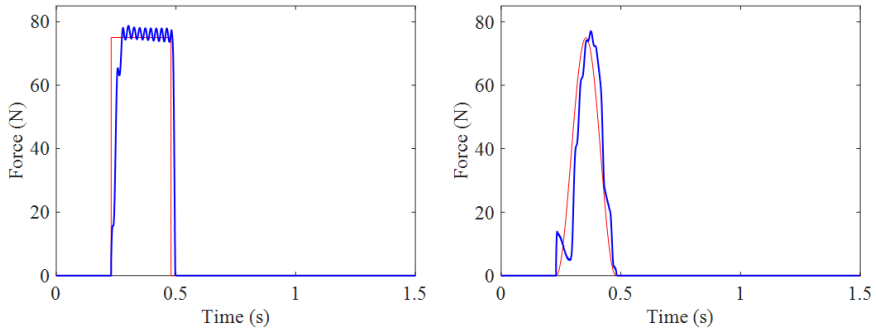

Figure 5.8: Force tracking performance for simulations carried out with two reference profiles lasting 250 ms with 75 N amplitude.

the system performed with better accuracy and without large oscillations when a step variation was selected.

Table 5.3 reports impulse accuracy and tracking errors given by the simulations presented. Although trials performed with the sine wave reference profile showed very low impulse accuracy error, tracking errors always exceeded the 30% threshold and almost doubled the values of tracking errors obtained when a square pulse was selected. Therefore, as supported by the analysis carried out in the model and detailed in this section, the square reference profile seemed to be the most suitable for the system to be implemented in following analyses. Since the system was focused on regulating the perturbation impulse, it was necessary to select the

solution that allowed for more reliable and accurate perturbations.

Reference profile	**Amplitude** (N)	**Duration** (ms)	I_{acc} (%)	E_{tr} (%)
Square	50	250	1.37	13.96
Sine + bias	50	250	0.72	35.91
Square	75	250	0.59	14.33
Sine + bias	75	250	0.71	31.26
Square	50	100	1.88	32.97
Sine + bias	50	100	1.43	70.88

Table 5.3: Impulse accuracy I_{acc} and tracking errors E_{tr} obtained for different reference force profiles.

5.3.2 Control solutions for approach and contact phases

In this section, simulations and experimental data regarding the different control logic solutions described in section 4.3 are presented. AP modeling was based on the solution adopting low friction ISO 15552 cylinder and high performance valves LRWD2. The same force reference profile (square pulse, 50 N, 200 ms) was used for all the simulations, whereas the model was configured with the parameters reported in Table 4.2. Different control solutions were implemented separately for approach and strike phases.

Regarding the approach phase, the following solutions were investigated both in the model and in the experimental system:

- open-loop motion control;
- closed-loop force control;
- closed-loop motion control.

Open-loop motion control was already considered for the first AP prototype (section 3.3), whereas closed-loop force and motion control were developed specifically for the test-bench. Motion control could be implemented thanks to the laser displacement sensor integrated in the architecture of the AP.

Regarding the strike phase, PI and non-linear controllers were tested for the control of contact force. In particular, sliding mode control was only implemented and tested in the model. This choice was related to the necessity of additional measurements and processing that will be described in the following sections.

Open or closed-loop control during approach phase

Figures 5.9 - 5.11 present force tracking performance as well as the actuator stroke and carts displacements for every different control solution implemented during approach phase. In these first simulations, the oscillations of the operator were limited by choosing a high stiffness constant $k_1 = 30$ kN/m. Figure 5.12 presents the result for closed-loop motion control when a higher impact velocity (200 mm/s) was defined with respect to Fig. 5.11. Figure 5.13 shows the tracking of the displacement reference during the approach phase, for both velocities considered.

Then, system performance was evaluated by considering three different values of initial distance Δx between the perturbator and the stricken body. In each condition, the same control parameters were selected. The operator should be able to exert the perturbations with the same level of accuracy and repeatability regardless of his or her positioning with respect to the subject. Figures 5.14 - 5.16 present the results of these simulations for open-loop control, closed-loop force control and closed-loop motion control solutions.

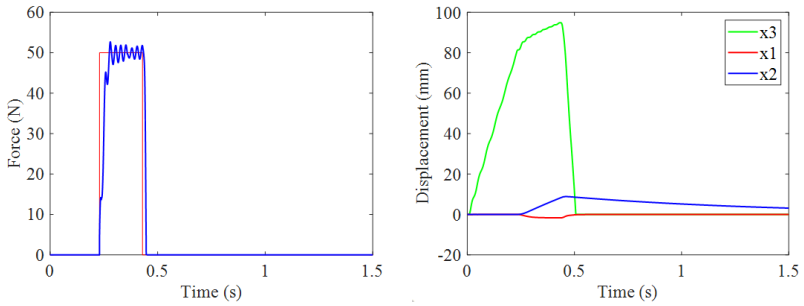

Figure 5.9: Force tracking performance (left) and resulting displacements (right) observed in the model, open-loop control during approach: x_1 refers to the operator's cart, x_2 to the stricken body, x_3 to piston stroke.

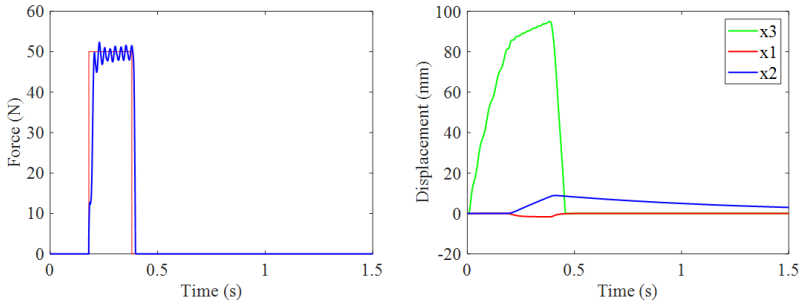

Figure 5.10: Force tracking performance (left) and resulting displacements (right) observed in the model, closed-loop force control during approach: x_1 refers to the operator's cart, x_2 to the stricken body, x_3 to piston stroke.

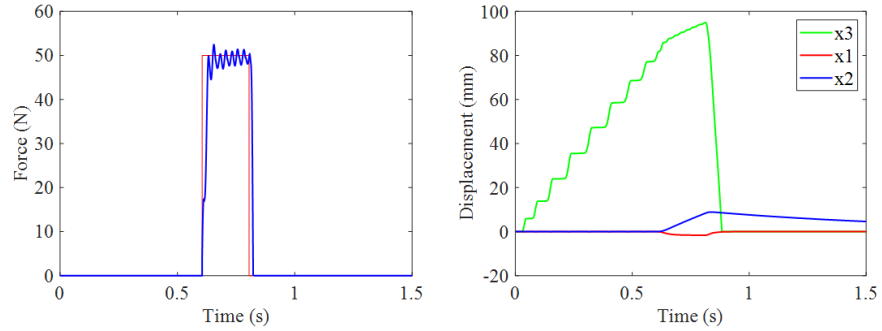

Figure 5.11: Force tracking performance (left) and resulting displacements (right) observed in the model, closed-loop motion control during approach, constant velocity reference equal to 140 mm/s: x_1 refers to the operator's cart, x_2 to the stricken body, x_3 to piston stroke.

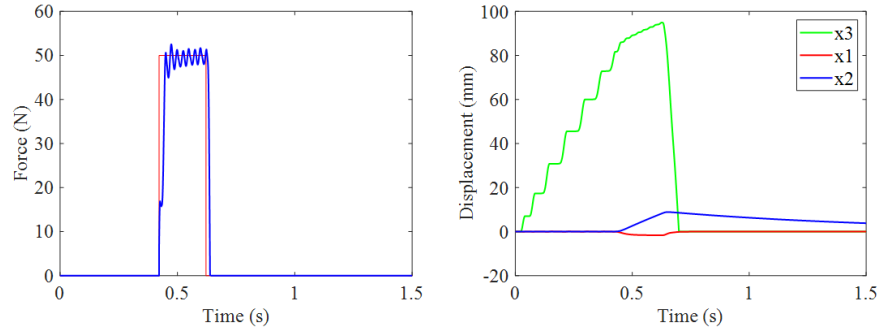

Figure 5.12: Force tracking performance (left) and resulting displacements (right) observed in the model, closed-loop motion control during approach, constant velocity reference equal to 200 mm/s: x_1 refers to the operator's cart, x_2 to the stricken body, x_3 to piston stroke.

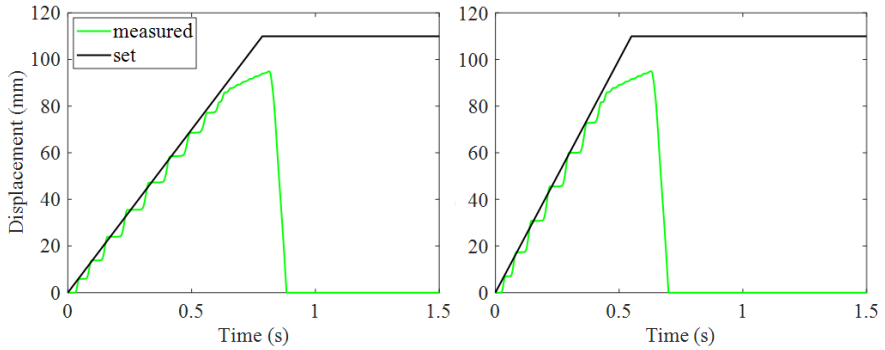

Figure 5.13: Motion tracking performance with 140 mm/s (left) and 200 mm/s (right) velocity references, closed-loop motion control during approach.

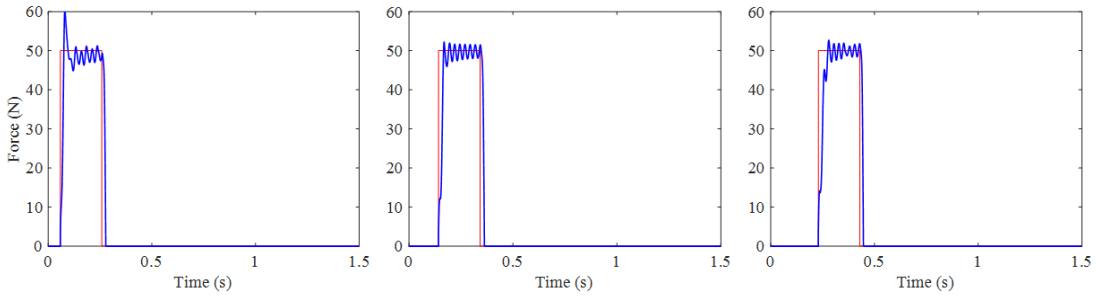

Figure 5.14: Force tracking performance observed in the model, open-loop control during approach, for different initial distance Δx: 20 mm (left), 50 mm (center), 80 mm (right).

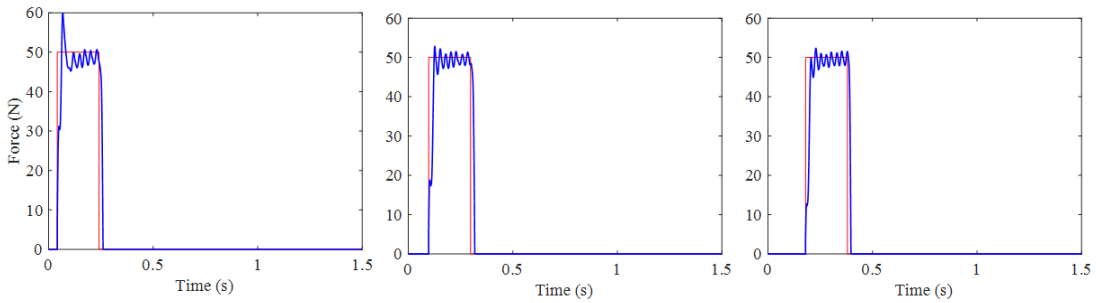

Figure 5.15: Force tracking performance observed in the model, closed-loop force control during approach, for different initial distance Δx: 20 mm (left), 50 mm (center), 80 mm (right).

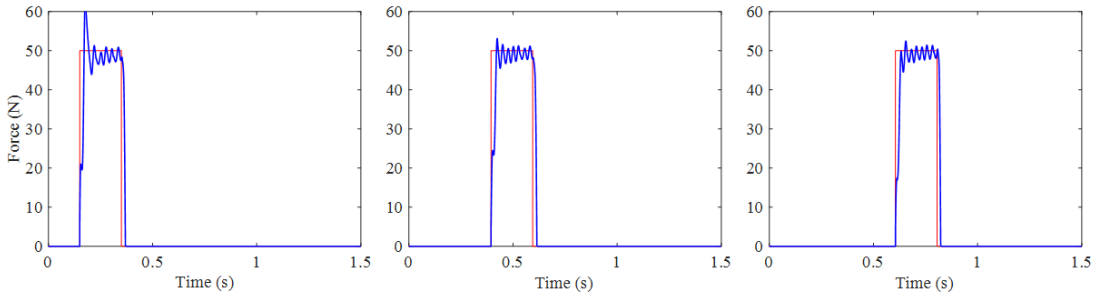

Figure 5.16: Force tracking performance observed in the model, closed-loop motion control during approach, for different initial distance Δx: 20 mm (left), 50 mm (center), 80 mm (right).

Figure 5.17 shows tracking performance for closed-loop motion control when a lower k_1 was selected. Figure 5.18 presents the corresponding actuator stroke and carts displacement. In these simulations, the role of different operators on the reliability of the control logic was considered. Table 5.4 reports impulse accuracy and tracking errors for the results showed in Figs. 5.14 - 5.17.

Control logic	Δx (mm)	k_1 (kN/m)	I_{acc} (%)	E_{tr} (%)
Open-loop	20	30	0.98	16.68
Open-loop	50	30	0.45	17.70
Open-loop	80	30	1.93	17.46
Closed-loop force	20	30	0.85	15.55
Closed-loop force	50	30	0.04	16.90
Closed-loop force	80	30	1.42	16.09
Closed-loop motion	20	30	0.72	17.32
Closed-loop motion	50	30	0.19	16.30
Closed-loop motion	80	30	1.25	16.04
Closed-loop motion	20	3	0.29	18.29
Closed-loop motion	50	3	0.84	17.15
Closed-loop motion	80	3	2.97	16.17

Table 5.4: Impulse accuracy I_{acc} and tracking errors E_{tr} obtained for different control solutions during approach phase.

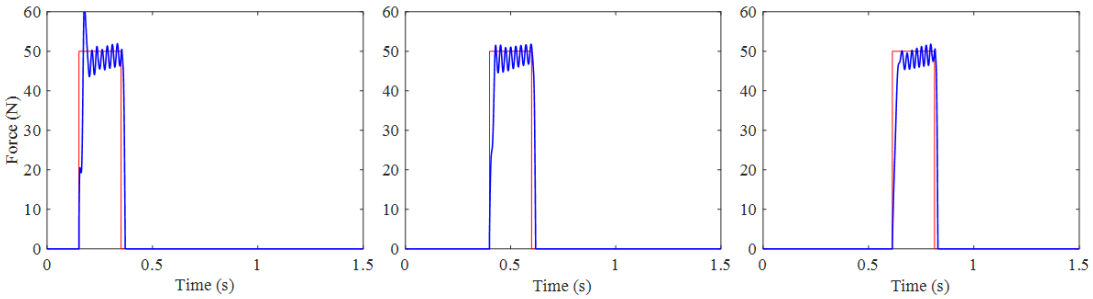

Figure 5.17: Force tracking performance observed in the model, closed-loop motion control during approach, for different initial distance Δx: 20 mm (left), 50 mm (center), 80 mm (right). With respect to Fig. 5.16, lower stiffness of the operator's mechanical impedance was selected.

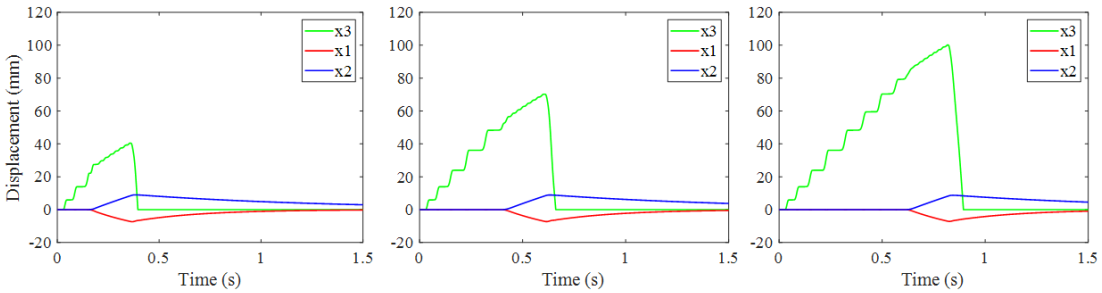

Figure 5.18: Operator displacement x_1, stricken body displacement x_2 and actuator stroke x_3 observed in the model, closed-loop motion control during approach, for different initial distance Δx: 20 mm (left), 50 mm (center), 80 mm (right). With respect to Fig. 5.16, lower stiffness of the operator's mechanical impedance was selected.

Figures 5.19 and 5.20 show the performance of the experimental system with different control solutions during approach. The test-bench was set in full fixed configuration (A) and equipped with the MQM cylinder. The valves used were the LRWD2. In this configuration, the AP was tested for two different values of the initial distance between striker and stricken body. In particular, Fig. 5.19 refers to open-loop solution, whereas Fig. 5.20 presents the results of force tracking when a closed-loop motion control was used. As pointed out in section 4.3, stroke measurement provided by the laser sensor was fed back to the control logic to perform the regulation of piston's speed during approach (set value equal to 70 mm/s). The same impulse, with 50 N amplitude and lasting 150 ms, was used in all the experimental trials presented in this section.

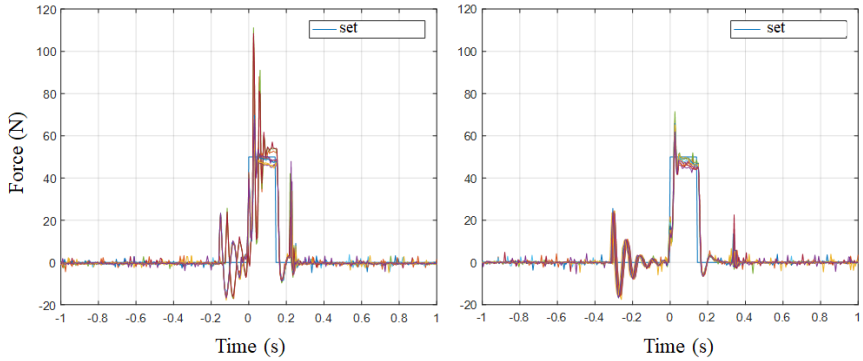

Figure 5.19: Force tracking performance observed in the experimental test-bench, open-loop control during approach, for different initial distance Δx: 50 mm (left), 80 mm (right).

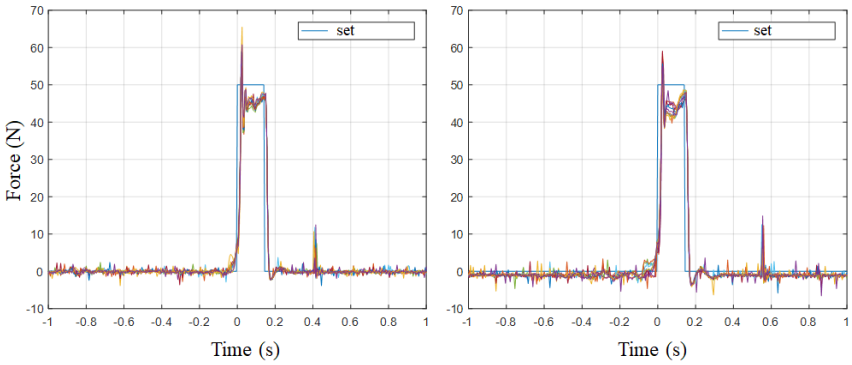

Figure 5.20: Force tracking performance observed in the experimental test-bench, closed-loop motion control during approach, for different initial distance Δx: 50 mm (left), 80 mm (right).

Discussion of the different control solutions during approach

The system showed quite similar performance in open-loop motion control (Fig. 5.9) and in closed-loop force control (Fig. 5.10) during approach, since both of the solutions only indirectly controlled the velocity of piston rod. A constant force reference equal to 5 N, used in the second control solution, drove the rod with almost the same speed observed with the first open-loop control solution. By selecting different force references, or alternatively by tuning of the control gains, it was possible to drive the piston with different velocity. However, as already pointed out above, the first two solutions only represented an indirect approach to control the motion of the striker before impact. Figure 5.11 shows the performance of the system when a closed-loop motion control was selected. Force tracking accuracy, at least in the model, was similar to the one obtained for the other solutions. However, this approach allowed for selecting a fixed velocity during approach set to 140 mm/s for the results presented in Fig. 5.11. With respect to Figs. 5.9 and 5.10, the relative piston rod displacement x_3 presented in Fig. 5.11 showed a more irregular behavior, due to the effect of friction on the controller accuracy. However, since the actual profile of rod displacement during approach is quite irrelevant for the application, whereas the control of impact velocity is fundamental to achieve more reliable and repeatable results, closed-loop motion control seemed to be the most appropriate and effective for the scopes of this application. It was indeed possible to select different impact velocity (see Fig. 5.12). Similarly to Fig. 5.11, it can be seen that the system was capable to follow the predefined reference with good accuracy, as highlighted by the performance of force tracking (see Fig. 5.13).

Figs. 5.14 to 5.16 show the performance of force tracking in the model for different initial distance between striker and stricken body. The values of Δx selected (20, 50 and 80 mm) were chosen to cover most of the actuator stroke available.

Performance of force tracking were quite similar for all the control solutions tested, with a significant overshoot in the first condition ($\Delta x = 20$ mm). It should be highlighted that: (i) the controller gains were not tuned finely for each condition, therefore they could have been customized to limit or even remove any overshoot in the contact force; (ii) the value of 20 mm did not likely represent a non realistic condition, since in all of the preliminary trials performed with the first AP prototype, the operator could keep a distance of at least 50 mm. However, these simulations proved that the AP could not perform accurately enough when a very short distance was set between the operator and the body of the subject, even if the approaching speed was regulated. As showed in Fig. 5.16, the impact occurred in only 150 ms when $\Delta x = 20$ mm, hence the controller was not fast enough to limit the error in that situation.

Figure 5.17 shows tracking performance for closed-loop motion control when a lower k_1 was selected. Figure 5.18 presents the corresponding actuator stroke and carts displacement. In these simulations, the role of different operators on the reliability of the control logic was considered. Even for large variations of x_1 with respect to the results presented in the previous simulations, force tracking performance was not significantly affected.

With respect to the results observed in the model (Figs. 5.14 - 5.16), the test-bench showed significantly higher performance regardless of initial distance when a closed-loop control was set during the approach phase (see Figs. 5.19 and 5.20). Discrepancy with the model is likely due to lack of accurate modeling of some aspects, as the presence of friction on cart sliding due to the linear guide. In such a complex environment, with larger impact of non-linear phenomena such friction, the experimental system performed significantly better with closed-loop motion control solution. Initial oscillation of perturbation force before contact (see Fig. 5.19) was probably due to the inertial effect of the sliding masses that acted as an apparent force exerted on the piston. Accurate control of piston displacement during approach (see Fig. 5.20) instead removed completely such oscillations, providing a smoother behavior of the perturbator during both approach and contact phases. Both Figs. 5.19 and 5.20 present the results of five consecutive perturbations, highlighting also high level of repeatability of the perturbation system.

Linear and non-linear controllers for contact force regulation

A linear PI and a non-linear model-based sliding mode controllers were implemented and tested through simulations. The system was analyzed in the default configuration of the test-bench (ISO 15552 cylinder + LRWD2 valves). Moreover, closed-loop motion control presented in the previous section was implemented during approach phase. Figures 5.21 - 5.23 show the performance in configuration B (AP fixed and stricken body free to move) for different choices of perturbation amplitude and duration, whereas Figs. 5.24 and 5.25 refer to configuration C (both

carts free to move) with 200 ms and 100 ms lasting stimuli.

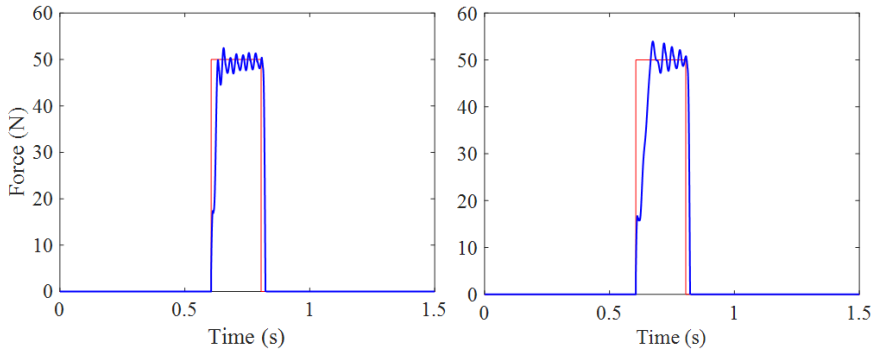

Figure 5.21: Force tracking performance observed in the model (configuration B) for 50 N perturbation lasting 200 ms, with different controllers: PI (left), sliding mode (right).

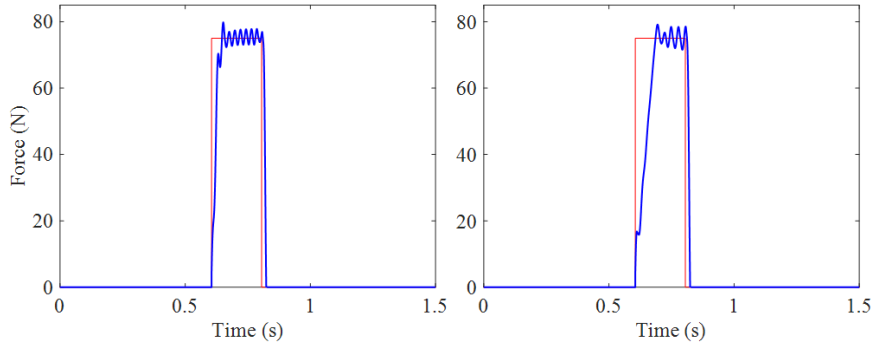

Figure 5.22: Force tracking performance observed in the model (configuration B) for 75 N perturbation lasting 200 ms, with different controllers: PI (left), sliding mode (right).

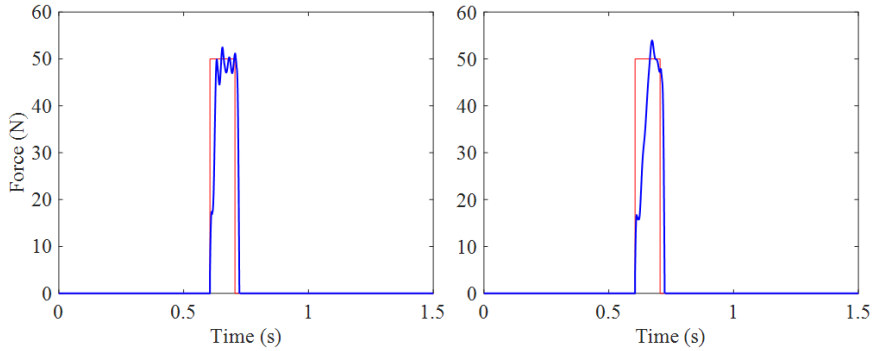

Figure 5.23: Force tracking performance observed in the model (configuration B) for 50 N perturbation lasting 100 ms, with different controllers: PI (left), sliding mode (right).

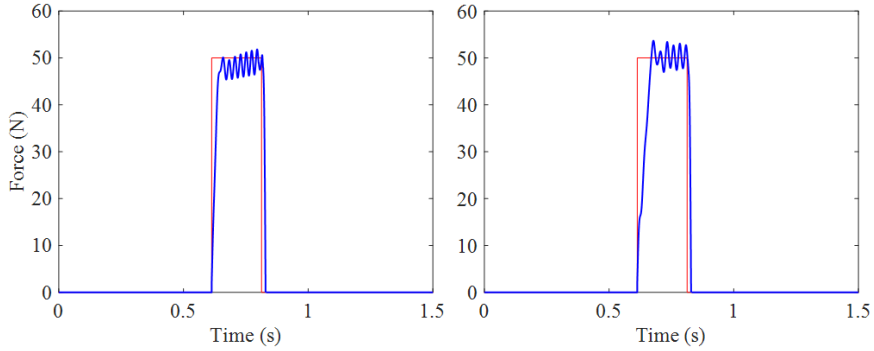

Figure 5.24: Force tracking performance observed in the model (configuration C) for 50 N perturbation lasting 200 ms, with different controllers: PI (left), sliding mode (right).

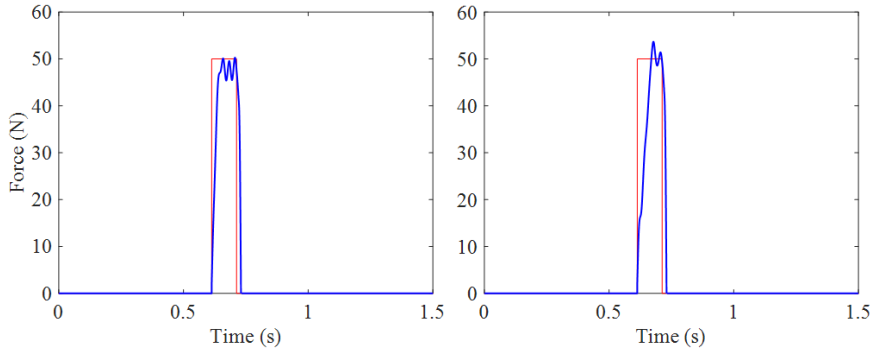

Figure 5.25: Force tracking performance observed in the model (configuration C) for 50 N perturbation lasting 100 ms, with different controllers: PI (left), sliding mode (right).

Only configurations B and C were shown since they match the real setting of experimentation with better accuracy. The accuracy of both controllers was similar in all configurations considered, as confirmed by data presented in Table 5.5. Sliding

Control logic, conf.	**Amp. (N)**	**Duration (ms)**	I_{acc} (%)	E_{tr} (%)
Proportional-Integral, B	50	200	1.25	16.04
Sliding mode control, B	50	200	5.63	21.97
Proportional-Integral, B	75	200	0.30	16.04
Sliding mode control, B	75	200	11.26	27.35
Proportional-Integral, B	50	100	0.93	30.14
Sliding mode control, B	50	100	11.26	41.59
Proportional-Integral, C	50	200	2.97	16.17
Sliding mode control, C	50	200	5.72	20.84
Proportional-Integral, C	50	100	3.39	28.47
Sliding mode control, C	50	100	10.99	38.90

Table 5.5: Impulse accuracy I_{acc} and tracking errors E_{tr} obtained for different control solutions during strike phase.

mode controller for 75 N perturbations (Fig. 5.22) had to undergo an additional tuning process to perform with sufficient accuracy. With respect to PI controller, the non-linear solution highlighted a more compliant behavior especially during first half of the perturbation, that could not be removed by tuning of the controller gains (K_{smc} and δ). In addition, sliding mode control law presented larger and faster oscillations than the one obtained for PI controller. This chattering worsened if a lower δ was chosen (see Fig. 5.26, $\delta = 0.01$ N). The default parameters were K_{smc} = 0.25 and $\delta = 2$ N. Oscillations in the control law could especially affect the performance of the experimental system rather than the model, since real valve dynamics could be not sufficiently high to provide adequate response.

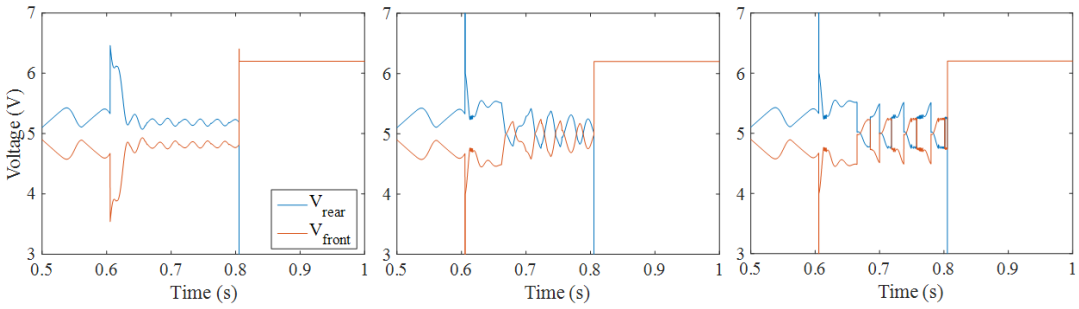

Figure 5.26: Command signals obtained for different controllers: PI (left), sliding mode with $\delta = 2$ N (center), sliding mode with $\delta = 0.01$ N (right).

For the reasons discussed, PI controller was selected as the most appropriate solution for the development of a second AP prototype. The increase of complexity of the controller and the need for additional instrumentation needed to run sliding mode logic (see section 4.3.2) was not balanced by a significant increase of performance in force tracking. It is clear that such architecture is potentially more accurate than simple linear control, especially given the possibility to take into account non-linear phenomena of the plant directly into the formulation of the command signal. However, for this particular application, accuracy of the perturbation generation strictly depended on the responsiveness of control logic that resulted better for PI control. As reported in Table 5.5, tracking accuracy worsened for very short perturbations, however impulse accuracy was consistently higher when PI control was implemented.

5.3.3 Effect of new components tested with the test-bench

As highlighted by simulations presented so far, the second architecture of the AP, based on a pneumatic cylinder and valves with high performance, allowed for selecting short lasting perturbations that could be exerted with good accuracy. However, it was fundamental to test such components in a real environment, since the model matched experimental results only with limited precision, mainly due to the approximations related to the description of non-linear phenomena such as friction. Figure 5.27 shows the performance of AP mounted on the test-bench for perturbations lasting 300 ms, when low cost components from initial AP prototype were still used (section 3.2, ISO 6432 cylinder and 3AF2 valves). As already highlighted by the preliminary analyses performed with such prototype (section 3.4), limited dynamics of the AP did not allow for accurate tracking of reference force profile during impact. Such inaccuracy became even larger when both the AP cart and the stricken body were free to move (configuration C), as reported in Fig. 5.27. The most accurate results were obtained for configuration A, with only 2.67 % of impulse accuracy error. However, tracking performance were really poor even in theoretically optimal configuration A. Especially due to limited dynamics of the valves, and also due to stick-slip effect related to high friction on piston sliding, every stimulus lasted consistently 70 ms more than the reference pulse. An increase of controller gains poorly affected the duration of the stimuli, increasing the risk for overshoot (especially for fixed configuration A). Results given by former selection of components confirmed that the AP could not fulfill the requirements of the application in such stage. Figure 5.28 shows the performance of the AP mounted on test-bench with every actuator considered, when the former valves (3AF2) were mounted. Test-bench was set in full fixed configuration A. The reference force profile had 50 N magnitude and lasted 250 ms. The system was open-loop controlled during approach phase, whereas a PI controller (as the one presented in the previous section) was implemented to regulate contact force during impact.

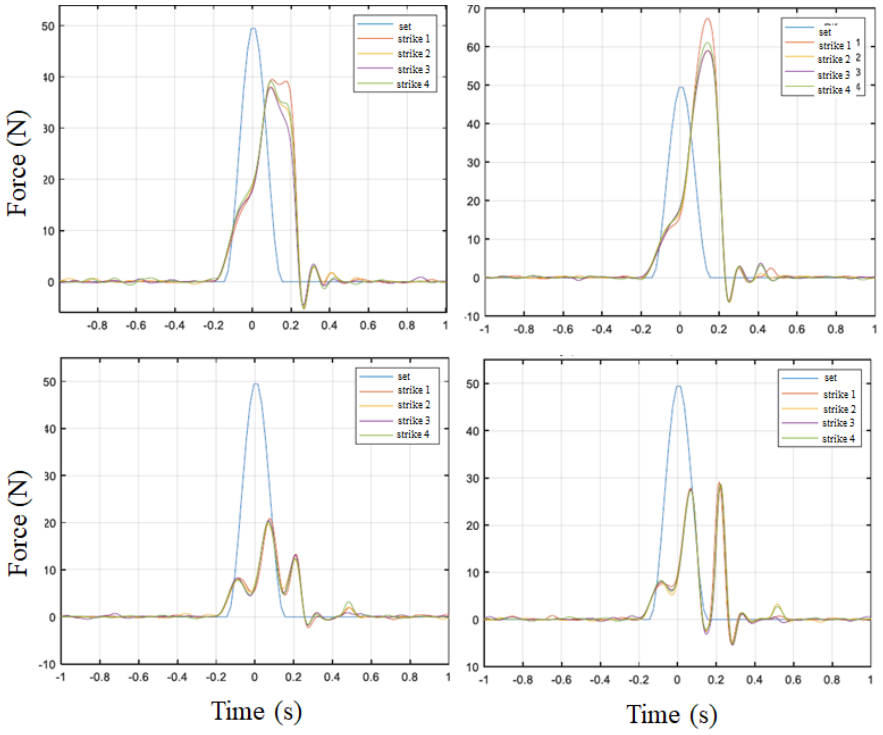

Figure 5.27: Force tracking observed during experimental trials in different configurations (top: A; bottom: C) for different values of proportional gain (left: $k_p = 1$; right: $k_p = 1{,}5$) [74]. AP architecture based on the ISO 6432 cylinder and the 3AF2 valves.

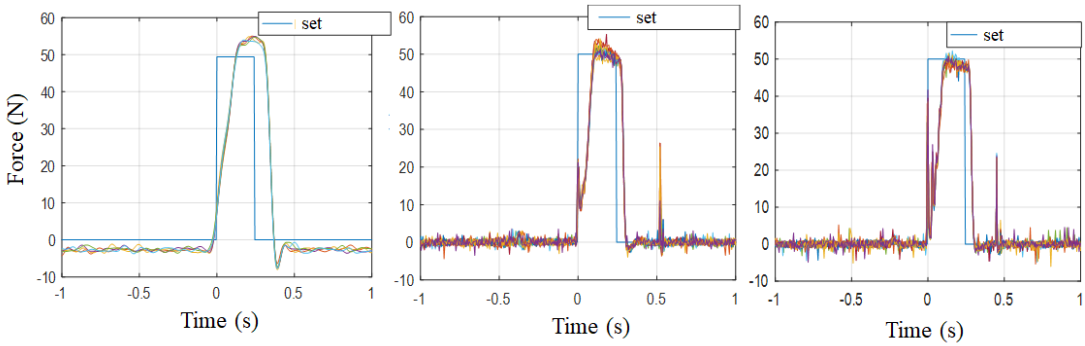

Figure 5.28: Force tracking observed during experimental trials, configuration A, for different pneumatic cylinders: ISO 6432 (left), ISO 15552 (center), MQM (right). AP architecture based on the 3AF2 valves.

The introduction of new ultra-low friction pneumatic cylinders significantly improved the accuracy of the AP by limiting the force overshoot and by reducing the step response time. The second peak (approximately 25 N) shown in Fig. 5.28 was

given by fast retraction of the striker occurring after the perturbation (during the return phase). With respect to the ISO 15552 cylinder, the MQM one showed even higher responsiveness. This behavior was probably due to the lack of plastic seals in the latter, whereas the former had NBR gaskets. For this reason, friction likely had negligible impact on the performance of the MQM cylinder. That actuator has been designed by the manufacturer to control forces as low as 0.05 N, with minimal sliding resistance allowing pressure actuation at 0.005 MPa.

However, although tracking accuracy already improved significantly with the new selection of actuators, the resulting force profiles still showed a rather slow transient when step reference variations occurred (see Fig. 5.28). Such delay did not allow for testing perturbations that lasted less than 250 - 300 ms. This specification could be achieved only when new valves (LRWD2) were used. Figure 5.29 shows force tracking performance for the AP solution based on the MQM cylinder. By

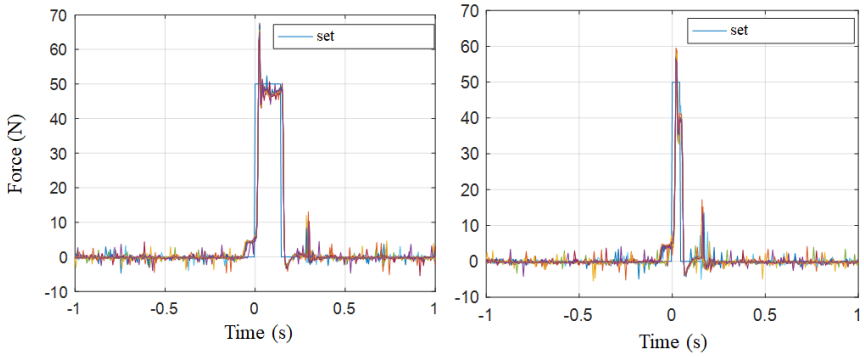

Figure 5.29: Force tracking observed during experimental trials, configuration A, with stimuli lasting 150 ms and 50 ms, 50 N magnitude. AP architecture based on the MQM cylinder and the LRWD2 valves.

comparison with Fig. 5.28, it is clear that the LRWD2 valves largely improved the dynamic response of the system. This solution enabled fast perturbations, e.g. lasting 150 ms and 50 ms (see Fig. 5.29), with good level of tracking accuracy and repeatability. I_{acc} was 1.40 % for the 150 ms duration, and raised to 12.26 % for stimuli lasting only 50 ms. However, it was predictable that impulse and tracking accuracy for such short perturbations could not be as high as expected for 100 ms or longer stimuli, since pneumatic actuation has inevitable limitations regarding the dynamics allowed. The performance of the system, based on MQM cylinder and LRWD2 valves, for different magnitude and duration of the stimuli are presented in Fig. 5.30. While Figs. 5.29 and 5.30 refer to the test-bench in fixed configuration A, Fig. 5.31 shows the performance of the system when both carts were free to move (configuration C) for 50 N stimuli lasting 50 ms and 150 ms.

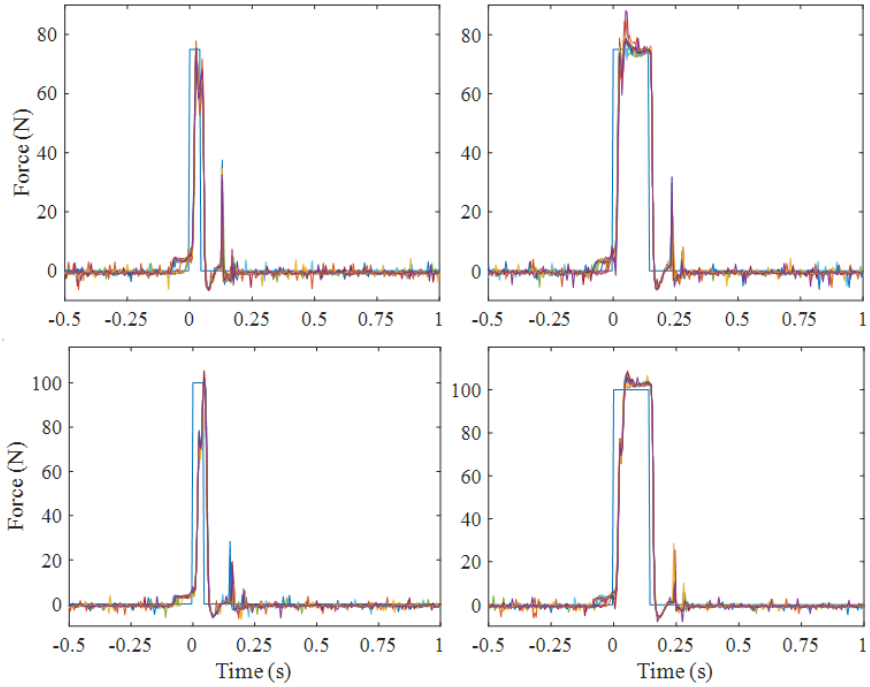

Figure 5.30: Force tracking observed during experimental trials, configuration A, with stimuli lasting 150 ms and 50 ms, 75 N and 100 N magnitude. AP architecture based on the MQM cylinder and the LRWD2 valves.

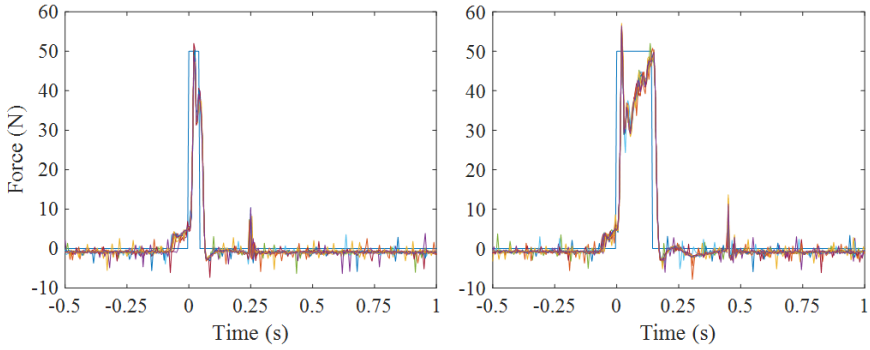

Figure 5.31: Force tracking observed during experimental trials, configuration C, with stimuli lasting 150 ms and 50 ms, 50 N magnitude. AP architecture based on the MQM cylinder and the LRWD2 valves.

Similarly to Fig. 5.30, Fig. 5.32 shows tracking performance for different amplitude and duration of the perturbations (in configuration C). These results demonstrated that the system could perform with sufficient accuracy, even for short lasting perturbations (50 ms), when both operator and subject compliances were taken into

account. However, for final validation of such architecture, experimental trials on actual subjects had to be performed. The final architecture of pneumatic actuated AP prototype is presented in the next chapter, as well as the results of clinical trials performed on healthy subjects.

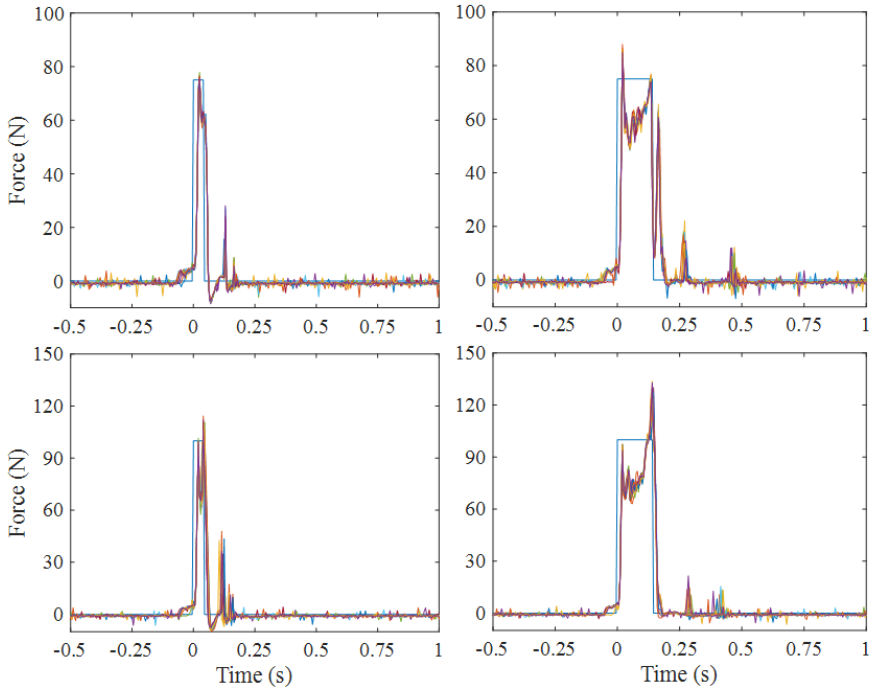

Figure 5.32: Force tracking observed during experimental trials, configuration C, with stimuli lasting 150 ms and 50 ms, 75 N and 100 N magnitude. AP architecture based on the MQM cylinder and the LRWD2 valves.

Chapter 6

Final pneumatic prototype of automatic perturbator

The final version of the pneumatic actuated AP is presented in this chapter. Accuracy and repeatability of the perturbator were evaluated by two different operators, then two sets of trials were performed on healthy subjects to tackle the limitations observed during preliminary analyses carried out with the MP and with the first AP prototype.

6.1 Architecture and control design of the AP

The final prototype of AP (Figs. 6.1 and 6.2) shared most of the components used for the first AP prototype. However, its architecture is described in details again for sake of clarity. It consisted of the following parts:

- an ultra-low friction linear double acting pneumatic actuator (MQM Series by SMC Corporation Inc., Japan, stroke: 100 mm, bore: 25 mm);
- two flow proportional control valves (LRWD2 by Camozzi Automation S.p.A., Italy, 0 - 10 V of analog input, maximum pressure up to 10 bar, flow rate up to 700 l/min ANR), with driver embedded and located integral with the actuator;
- a uniaxial load cell (UMM by Dacell Co. Ltd., Korea, rated capacity 50 kg_f, nonlinearity, hysteresis and repeatability 0.1% of the rated capacity) and external signal conditioner (DEWE-RACK-4 by DEWETRON Inc., Austria), used to measure contact force during impact;
- a laser displacement transducer (Q4XTULAF300-Q8 by Banner Engineering Corp., USA, measurement range between 25 mm and 300 mm, linear output voltage range 0 - 10 V);

- an end damping pad covered by a thick layer (20 mm) of polyethylene;
- a circular plastic plate, integral with the damping pad, used as target to measure the cylinder stroke;
- two handles;
- a trigger button.

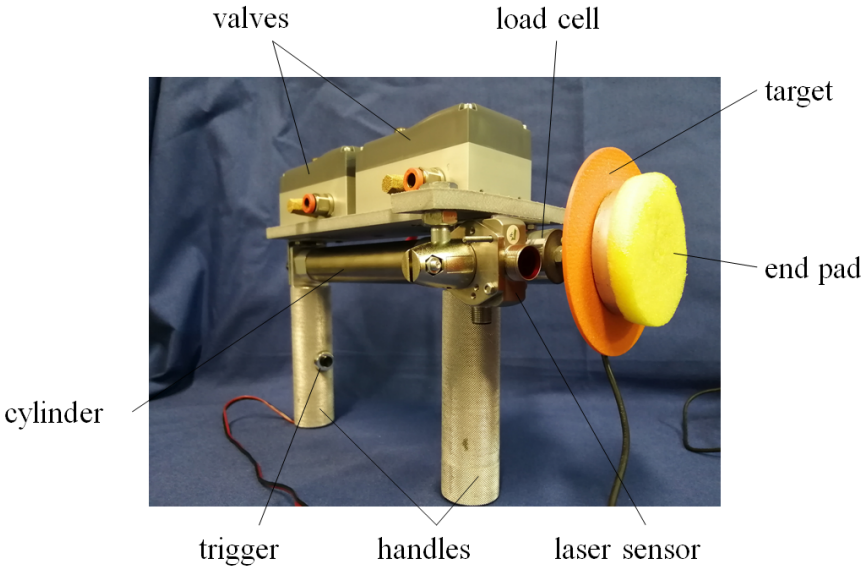

Figure 6.1: The final AP prototype.

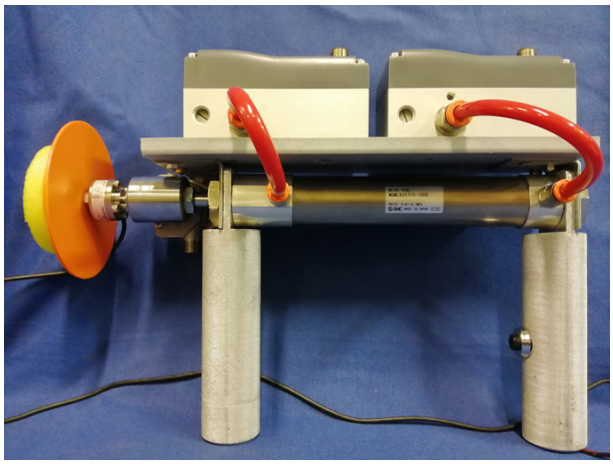

Figure 6.2: Lateral view of the AP.

A gauge pressure of 3.5 bar was set to supply the perturbation system. Similarly to the test-bench presented in the previous chapter, a real-time system (Speedgoat GmbH, Switzerland) was programmed in MATLAB® - Simulink® Real-Time™ (The MathWorks, Inc., USA) and used for both data acquisition and control prototyping. The sampling frequency was set to 1000 Hz, whereas the real-time system used for the first AP prototype ran at 200 Hz. This significant improvement was allowed by the higher performance of the real-time system implemented in the final version. As already reported in the previous chapter, this solution included two IO 183 modules (4 differential 16-bit analog inputs, 4 16-bit analog outputs, 100 kHz maximum aggregate sample rate for each module) and two IO 397 modules (4 differential simultaneous sampling 16-bit analog inputs, 4 16-bit analog outputs, 200 kHz maximum sample rate, FPGA-based, for each module). The user interface was programmed directly in Simulink®, therefore it was not necessary to use an external software (as ControlDesk® by dSPACE GmbH, Germany) to develop the panels and controls needed by the operator to configure the stimuli and to collect data of postural responses. A picture of the main system components is presented in Fig. 6.3.

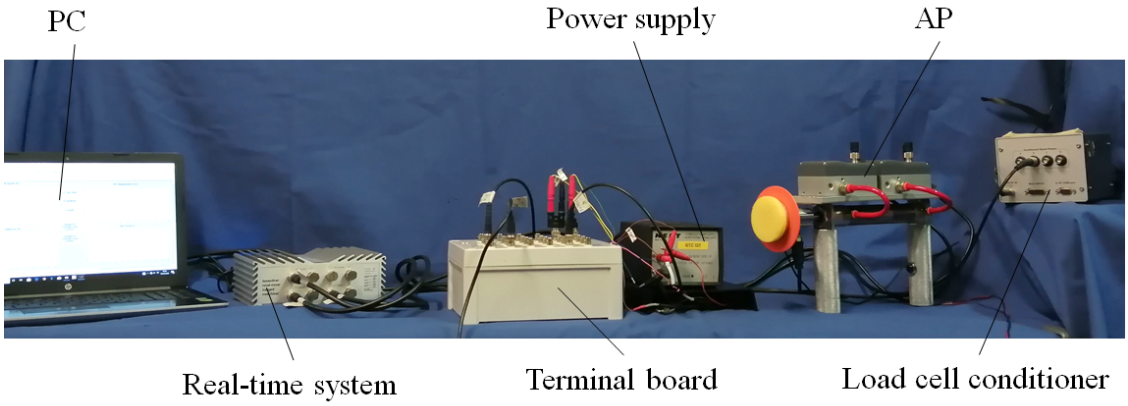

Figure 6.3: Main components of the final perturbation system.

Since valves embedded all the electronics in their case, the final system resulted significantly less bulkier. Moreover, since the overall weight of the valves was lower than that of the first AP prototype, the maneuverability of the device was generally improved as confirmed by the operators. Both valves were still placed on a frame integral with the pneumatic cylinder in order to shorten the pipes and to achieve the best dynamic performance (see Fig. 6.1). No significant vibrations resulting from valves and actuator were experienced during operation.

Control logic design was based on the trials performed with the model as well as on the test-bench in the previous chapter. Since a laser displacement sensor was implemented, a closed-loop motion control could be developed to drive the

piston at defined speed during the approach phase. On the other hand, the first AP prototype could not directly regulate piston velocity due to the lack of any dedicated transducer. The control logic was still sequential (see section 3.3) and designed in Stateflow® (The Mathworks, Inc., USA). Therefore, after occurrence of an external trigger by the operator, the transition between initial approach and strike phases was based on the detection of a force threshold. Direct force control during impact was based on a PI controller, since the implementation of a non-linear model-based controller did not show any significant improvement in force tracking accuracy (see section 5.3.2). After the impact, a return phase triggered automatically to retract the piston rod, then an idle phase put the system at rest, waiting for another input.

6.2 Tests with different operators

Since the AP is meant to be handled directly by the operator, the effect of different subjects maneuvering the device on perturbation's accuracy and repeatability was evaluated. Therefore, a skilled and a novice operators were asked to exert multiple perturbations to the body of a human subject standing on a force platform. The trial conditions corresponded to the typical ones of a real clinical posturographic task. All the stimuli were exerted from the back at thoracic level, keeping an initial distance between striker and operator equal to about 3 cm. Figure 6.4 shows force tracking performance for the two subjects. Force reference

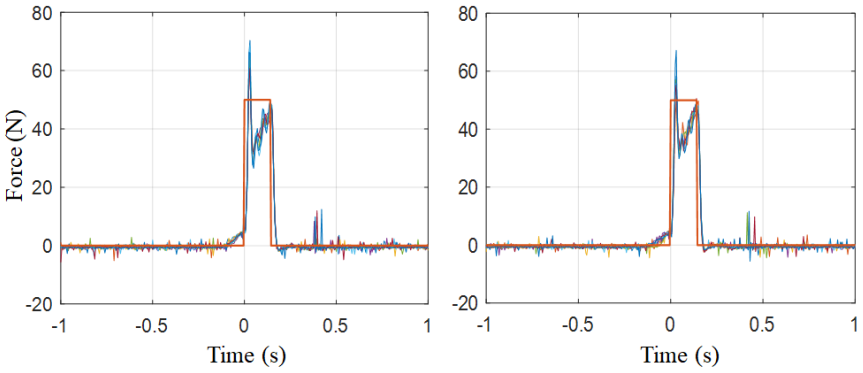

Figure 6.4: Force tracking performance of final AP prototype for consecutive thoracic perturbations, each plot refers to a different operator (left: a skilled one, right: a novice).

profile considered was the default one, with magnitude set to 50 N and lasting 150 ms. Each plot shows the results of eight consecutive stimuli exerted on the same subject. Although the operators did not own the same expertise in usage of the

AP (in particular, the novice had no prior experience with such device whereas the skilled one maneuvered the AP during all of the preliminary analyses), the tracking performance were absolutely similar in both conditions. This result confirmed that accuracy as well as repeatability of the perturbation system were not significantly affected by the operator. However, it should be highlighted that both operators were asked to direct the stimuli perpendicularly to the contact surface. Accuracy of the perturbation system is indeed directly related to the skill of the operator to chose the correct direction of the perturbation rather than to his or her ability to remain as steady as possible during application of the disturbance. For both operators, impulse accuracy was indeed higher than 85 %.

6.3 Trials on healthy subjects

6.3.1 The protocol

Experimental trials were conducted on 14 healthy subjects, all young adults (23 ± 2y) without any recent lower limb injury (in the last year) or balance deficits. Figure 6.5 shows an example of experimental trial carried out in laboratory. Among

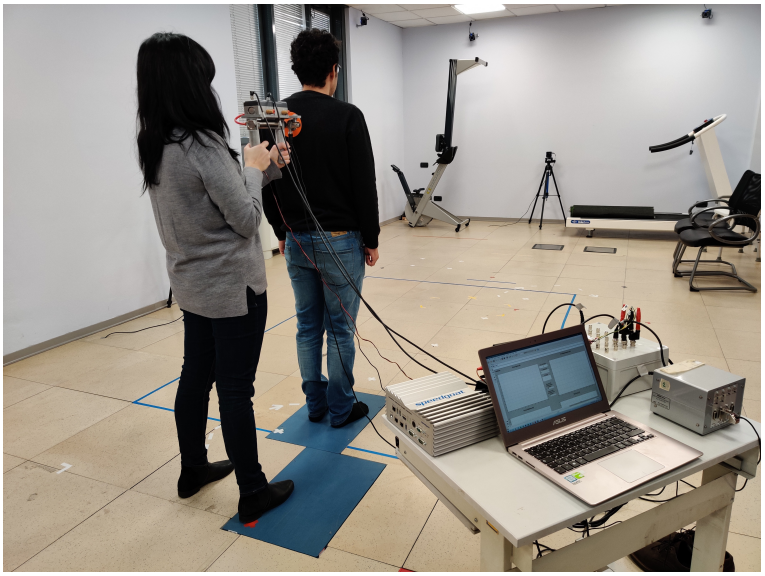

Figure 6.5: Thoracic perturbation exerted by the operator on a healthy subject with the final AP prototype.

the subjects, seven were males. They all had similar build (mean BMI equal to 21.5 ± 1.7 kg/m^2) and signed an informed consent to participate to trials. The protocol was similar to the one used for preliminary analyses carried out with MP or with first AP prototype. The only external disturbance to balance control considered

was the one provided by the AP, whereas visual and acoustic stimuli were limited respectively by exerting stimuli at the back of the subjects and by limiting noise through components that inherently allowed for silent operation. Each subject stood barefoot on the force platform in relaxed stance, with the feet locations traced directly on the surface of the platform to ensure the same positioning among the subjects. An initial stimulus was exerted before the beginning of the actual trial to help familiarization with the conditions of the task.

The perturbations were given only at thoracic (IS, inter-scapular) level, since it was not the scope of these trials to evaluate the differences among several levels of perturbation. Two sessions were performed, with 20 stimuli each. In first session, perturbations with the same amplitude (about 40 N) but different impulse were exerted, while, in second session, magnitude and duration of the stimuli were varied accordingly to provide constant impulse (5 N s) disturbances. For each value of magnitude or impulse, five perturbations were exerted in random order.

Similarly to section 2.4, impulse (I) and CoP displacement ΔCoP were considered respectively to characterize the input (perturbations) and output (response data) of each trial. Moreover, force amplitude F_a (in N), defined as the average of the force measured during the impact phase, was considered to characterize the perturbation.

6.3.2 Results and discussion

Figure 6.6 shows the results of force tracking and CoP displacement for several configurations of the stimuli during first session (constant peak force). Force tracking accuracy, especially for the shorter perturbations, was quite limited, however impulse accuracy was sufficient. Moreover, the stimuli were highly repeatable. This feature was fundamental to support the statistical analysis that was performed on the output data, since constant amplitude (first session) or constant impulse (second session) perturbations were required to perform the corresponding analyses.

Since the contact force was sampled at 1000 Hz, the relevant force overshoot shown in Fig. 6.6 could be clearly related to high frequency noise in signal acquisition. For instance, by filtering of contact force with a low pass Butterworth filter, eight order, cut off frequency set to 20 Hz (the same adopted to filter CoP data), peak force values were significantly decreased (about 35 - 40 % lower, see Fig. 6.7). Perturbation signals were not directly filtered during trial execution to avoid any delay and phase distortion provoked by digital filtering. Impulse and tracking accuracy values were calculated directly on the unfiltered force signals since they were only slightly affected by high frequency noise.

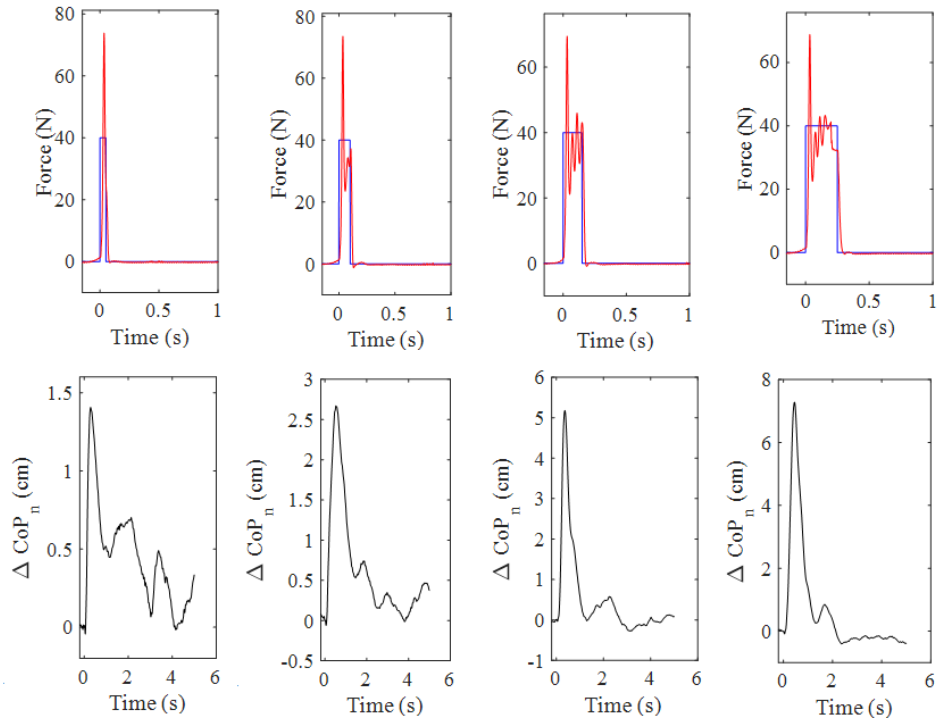

Figure 6.6: Force tracking and CoP displacement for a subject in first (constant peak force) session. Each plot shows the average of five perturbations and responses for a different impulse reference.

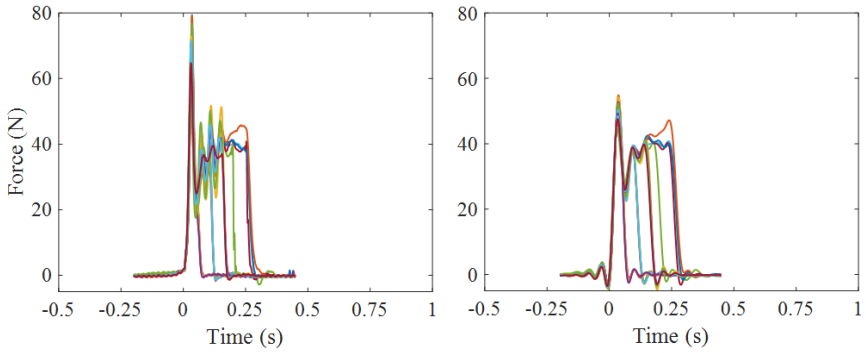

Figure 6.7: Effect of filtering on perturbation force in first session: unfiltered (left) and filtered (right) signals.

Figure 6.8 shows the results of force tracking (second session) for several amplitude and duration of the stimuli. In this session, the impulse was kept as constant. Data about perturbations repeatability and accuracy, averaged among all the subjects, are presented in Table 6.1 (first session) and in Table 6.2 (second session).

Impulse (N s)	**Duration** (ms)
2.0 ± 0.1	123.9 ± 38.2
3.9 ± 0.1	175.0 ± 44.3
5.9 ± 0.2	219.6 ± 29.6
9.9 ± 0.3	321.7 ± 40.1

Table 6.1: Impulse and duration of the stimuli averaged among the subjects, constant force (43.0 ± 3.8 N) session.

Impulse (N s)	**Force amplitude** (N)	**Duration** (ms)
4.5 ± 0.2	19.5 ± 0.6	335.7 ± 40.8
4.9 ± 0.2	38.3 ± 0.6	199.0 ± 34.5
4.3 ± 0.1	56.3 ± 1.2	162.8 ± 54.2
4.8 ± 0.1	96.8 ± 2.2	116.9 ± 38.3

Table 6.2: Impulse and duration of the stimuli averaged among the subjects, constant impulse session.

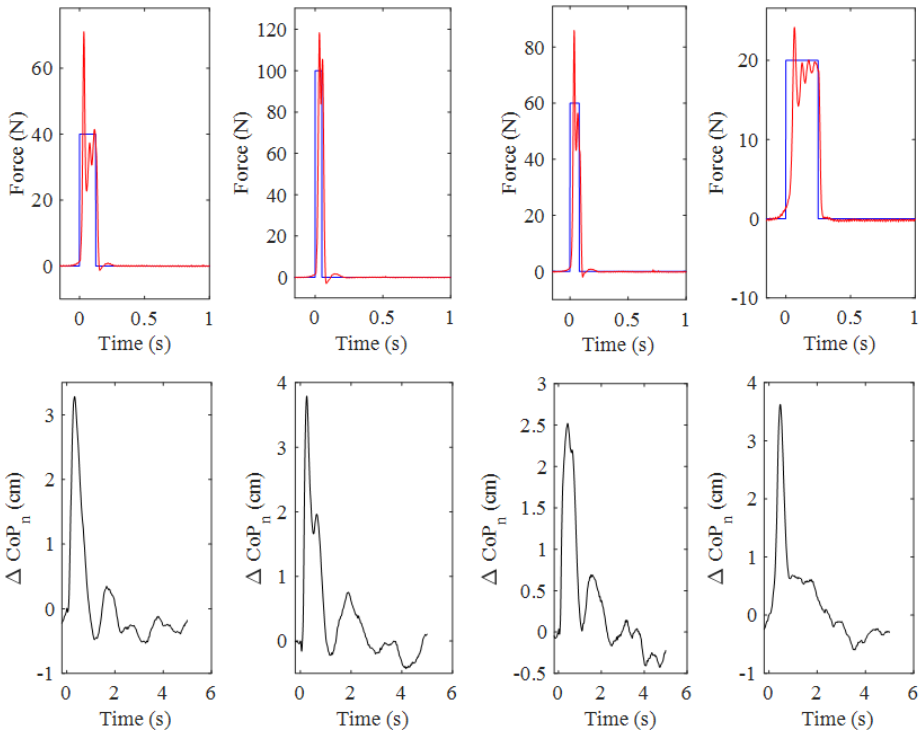

Figure 6.8: Force tracking and CoP displacement for a subject in second (constant impulse force) session. Each plot shows the average of five perturbations and responses for different magnitude and duration of the stimuli.

Analysis of the correlation between ΔCoP and I showed a more strict relationship than with F_a. The almost linear relationship between ΔCoP and I was confirmed for all subjects during the first session, i.e. when the force amplitude was kept constant. On the other hand, when the impulse was kept consent while the amplitude and duration were changed, it was not possible to find such linear relationship with the same level of correlation (see Fig. 6.9). While high impulses

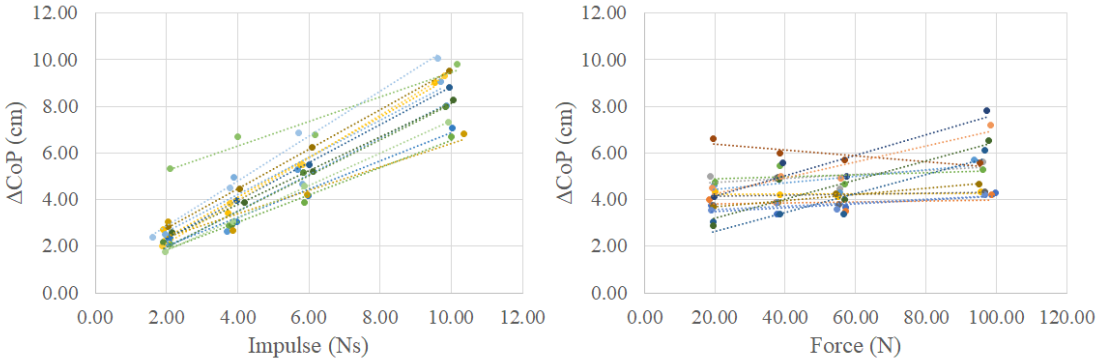

Figure 6.9: ΔCoP relationship with impulse (left) and force magnitude (right) for all subjects.

always led to an increase of CoP displacement, this was not always true for perturbations with high amplitude. The Pearson correlation coefficient was 0.96 when ΔCoP was correlated with I, whereas it was only 0.49 when the correlation between ΔCoP and F_a was considered. Therefore, as already performed during preliminary analyses, it was confirmed that is possible to consider the ratio between CoP displacement and impulse (ΔCoP_n) as an index for postural control stability. However, such index showed a consistent trend only for impulse higher than 4 N s (see Fig. 6.10).

6.3.3 Conclusion

The final AP design allowed for a much more precise and detailed analysis of the relationship between a mechanical perturbation and the postural reaction with respect to the first AP prototype. Thanks to the improved dynamics of the system, stimuli lasting 100 - 150 ms could be applied with sufficient accuracy and high repeatability. Tracking accuracy, especially for such short lasting perturbations, was still questionable but it did not prevent to obtain accurate and high repeatable impulse values. Since this feature represented the most relevant for the final aim of the perturbation system, given that a significant correlation between the impulse and the entity of the postural response was found, the efficacy of the proposed architecture for dynamic posturographic analyses was confirmed.

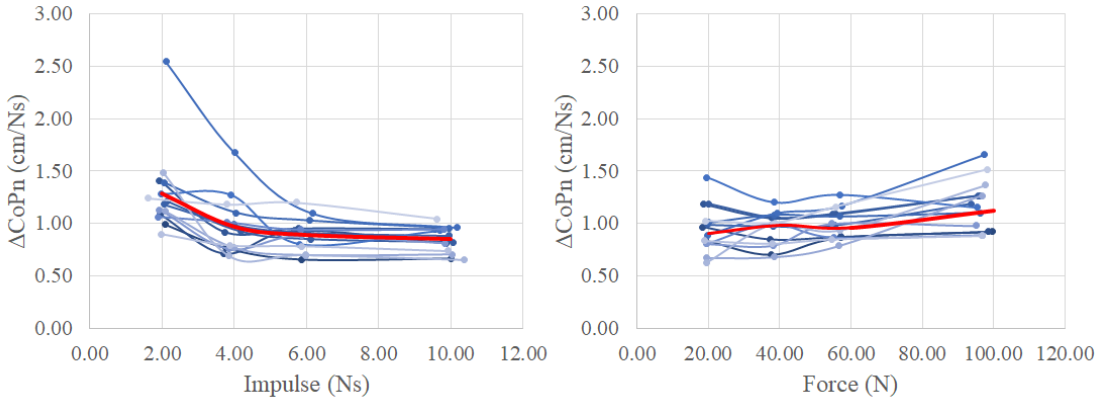

Figure 6.10: ΔCoP_n variation with impulse (left) and force magnitude (right) for all subjects.

Thanks to the improved performance, the final design of the system allows for deeper analyses of the mechanisms behind postural reaction. The analysis can also take advantage of models to describe the characteristics of active and passive responses that contribute to the whole postural reaction. This aspect will be discussed in the next chapter.

Chapter 7

Biomechanical modeling and analysis of postural response

In this chapter, two models for the analysis of postural response are presented. Model-based analyses can improve the interpretation of the response and provide information about kinetic and kinematic variables that cannot easily monitored during experimental trials. The implementation of multi-link models is discussed and output data are presented. The usage of these models, in combination with the automatic perturbator presented in the previous section, allows for the investigation of the physiological mechanisms behind postural reaction. Thanks to the ability of the AP to exert stimuli with defined impulse, it was possible to gather a reasonable amount of data on healthy subjects that was required for validation of the biomechanical models presented in this section.

Then, transfer function analysis (in the frequency domain) is discussed as a tool for the identification of unknown model parameters. Such technique, already applied for tuning of biomechanical models regarding postural control, allows for an appropriate definition of the control parameters required to stabilize the plant. The application of this methodology to dynamic posturography analyses based on impulsive perturbations is presented.

7.1 Biomechanical modeling of postural control

In this section, a single and a double link inverted pendulum models are presented. The former is described with both the typical (approximated) linearized formulation and the non-linear form. A model discussed in the literature for the implementation of neuromuscular noise is also presented. The models have been tuned by comparison of output data with experimental data available, i.e. the CoP displacement over the base of support.

7.1.1 Single link inverted pendulum model

This simple model has been already presented and discussed in many studies (e.g. [30, 31]). The body is represented by a rigid link with a single rotational degree of freedom about the ankle joint, which is described as a fixed hinge joint. This model is typically used to describe body motion in the sagittal plane when it is not required to investigate the interaction between body segments (e.g. upper and lower body, thigh and shank). It does not allow for distinguishing between left and right side, hence it would be not suitable for analyzing medio-lateral perturbations. The foot segment, integral with the base of support, is fixed. Figure 7.1 shows a graphical representation of this model when an external perturbation F_e is applied. In the following sections, the analytical model is presented, considering both a linearized and a non-linear formulation.

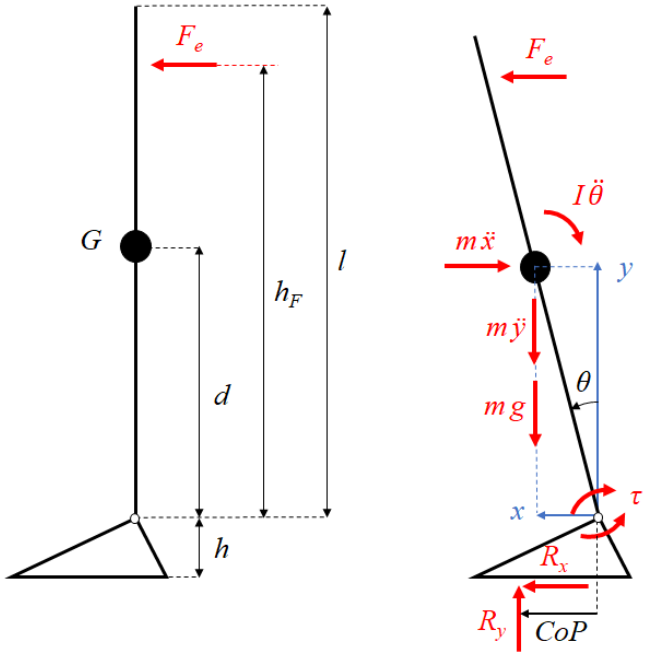

Figure 7.1: Representation of single link inverted pendulum model for postural analysis and free body diagram. Dot notation represents time derivative.

Linearized model dynamics

When limited oscillations occur about the ankle joint, it is possible to simplify the formulation of the mathematical model obtained by the system presented in Fig. 7.1. The following relationships can be assumed:

$$\cos\theta \simeq 1,\ \sin\theta \simeq \theta,\ \frac{d^2x}{dt^2} \simeq \frac{d^2\theta}{dt^2}\, d \tag{7.1}$$

in which θ represents the rotation of the body about the ankle joint, x is the antero-posterior coordinate of body center of mass CoM (G) and d is the distance between the ankle joint and CoM. The coordinate system is centered at the ankle joint. Under these approximations, the acceleration of CoM results only horizontal, hence the dynamic equilibrium of the system can be easily computed by solving the following equation:

$$\tau + mgd\,\theta - md^2\,\frac{d^2\theta}{dt^2} - I_G\frac{d^2\theta}{dt^2} + F_e h_F = 0 \tag{7.2}$$

τ is the correcting torque at the ankle, m is the body mass, g is the gravitational acceleration (9.81 m/s^2), I_G is the rotational inertia about CoM, h_F is the distance between ankle joint and the perturbation's point of application. Although not included in the equations, the length of the link l was also a parameter required for the simulations. Since τ and $F_e h_F$ represent respectively an internal and an external torque acting on the system, they can be combined as a sum in a separate term τ'. The relationship between the latter and θ (body sway) depends on the dynamic equilibrium of the body. By Laplace transformation of Eq. 7.2, the following formulation for the transfer function of the system is obtained:

$$\frac{\theta(s)}{\tau'(s)} = \frac{1}{I_A s^2 - mgd} \tag{7.3}$$

where s is the Laplace variable and I_A is the rotational inertia of the body with respect to the ankle. Such simplified formulation can only be used if Eq. 7.1 is true, i.e. for a linearized system. The transfer function, having eigenvalues with positive integer part, represents an unstable system. Without any correcting torque, any θ deviation would push the system out of stability. Therefore, an external or internal control action is required to keep the system stable. The following equations are used to calculate the horizontal R_x and vertical R_y components of the ground reaction force, as well as CoP displacement:

$$R_x = m\frac{d^2x}{dt^2} - F_e \tag{7.4}$$

$$R_y = mg \tag{7.5}$$

$$CoP = \frac{-\tau - R_x h}{mg} \tag{7.6}$$

where h is the height of ankle joint with respect to the fixed base of support.

Non-linear model dynamics

The same model presented in previous section can be studied when body oscillation θ does not have limited amplitude. In this configuration, Eq. 7.1 cannot be

used to simplify the equations describing dynamic equilibrium of the body, hence both horizontal and vertical components of CoM acceleration must be taken into account. The dynamic equilibrium can be solved starting from the following equations:

$$\tau + mgd\sin\theta - m\frac{d^2x}{dt^2}d\cos\theta + m\frac{d^2y}{dt^2}d\sin\theta - I_G\frac{d^2\theta}{dt^2} + F_e h_F\cos\theta = 0 \tag{7.7}$$

$$\tau + R_x h + R_y CoP = 0 \tag{7.8}$$

In this formulation, x and y represent respectively horizontal and vertical coordinate of CoM (with respect to a coordinate system centered at the ankle joint), that can be evaluated using the following equations:

$$x = d\sin\theta \tag{7.9}$$

$$y = d\cos\theta \tag{7.10}$$

By differentiation of Eqs. 7.9 and 7.10, velocity and acceleration of CoM can be easily computed. CoP displacement is calculated by solving Eq. 7.8 and substituting the following relations for R_x and R_y:

$$R_x = m\frac{d^2x}{dt^2} - F_e \tag{7.11}$$

$$R_y = m\frac{d^2y}{dt^2} + mg \tag{7.12}$$

Equation 7.7 can be solved only if τ expression is known. It will depend on both intrinsic (passive) and active control actions coordinated by central nervous system. In the following section, the methodology adopted to include both contributions is presented.

Modeling of control action at the ankle joint

Balance control involves the interaction between feedback and feed-forward systems. In this study, only the feedback part was considered since feed-forward only provides a minor contribution and cannot be easily modeled. Feedback control, managed by the central nervous system, processes the signals coming from vestibular, visual, proprioceptive sensors and generates the control action in terms of a torque at the ankle joint. The latter (τ) has been modeled accordingly to recent studies (e.g. [34]) and has been expressed as the sum of a passive and an active contribution, as given by the following equation:

$$\tau = \tau_p + \tau_a \tag{7.13}$$

The passive contribution τ_p is related to the intrinsic visco-elastic behavior of human joints which depends on muscles, bones, articular surfaces and ligaments interaction. As proposed in the literature, it is proportional to the deformation, and to the rate of deformation as well, within the joint. In the model described, such deformation corresponds to the rotation of the link (body) about the ankle joint, since only rigid segments are considered. Therefore, the following expression can be used:

$$\tau_p = -k_p\,\theta - \beta_p\,\frac{d\theta}{dt} \tag{7.14}$$

The minus sign is required since torque and rotation are both positive clockwise. On the other hand, active torque τ_a depends on the neuromuscular action mediated by the central nervous system. Therefore, this contribution is significantly dependent on the subject considered, since it is directly affected by his or her ability to keep balance. Moreover, other factors such as sport habit and physical condition have a large impact as well. Given that, the same subject could respond differently for large or small magnitude perturbations. As presented in several studies in the literature [18, 34, 38], active control can be effectively described by a PD (Proportional-Derivative) action, hence with a formulation similar to the one presented for passive torque (Eq. 7.14). However, the meaning of proportional and derivative terms in the following equation is quite different from the one attributed to passive torque:

$$\tau_a(t) = -k_a\,\theta(t - t_d) - \beta_a\,\frac{d\theta(t - t_d)}{dt} \tag{7.15}$$

Although τ_p was also time-dependent, time variable t has been highlighted in Eq. 7.15 to stress that a delay t_d has been implemented to take into account latency between the variation of θ and the generation of a correcting active torque. This latency includes the time needed for signal transmission and processing, as well as the one required for muscle activation. On the other hand, the passive reaction τ_p occurs with no latency. This delay would depend on the muscles involved, the type and location of the external perturbation, as well as on the subject considered. For sake of simplicity, it was set constant for the simulations. In the literature, the possibility to distinguish among several physiological mechanisms that contribute to such latency and to the general control action has been discussed. For instance, Authors in [19] isolated sensory (e.g. visual), neuromuscular and graviceptive systems and assigned weighing factors to each contribution to describe feedback mechanisms of central nervous system in postural control. However, the approach chosen in this study was to simplify such modeling by choosing a single time delay and only the rotation θ (and its first derivative) as control input variable. This decision was supported by the fact that it was not possible to distinguish among several feedback mechanisms needed to stabilize posture only by analysis of CoP displacement.

To take into account the limitations of proprioceptive and vestibular systems in the accurate determination of body positioning, which is directly related to the

rotation angle θ, it was necessary to introduce *physiological noise* into the model. Accordingly to [17, 18, 34], such sensory noise was modeled as a pink noise and created by scaling of a white noise signal with the methodology reported in [75]. The power spectral density (PSD) of such noise is inversely proportional to the frequency, and it has been demonstrated to provide a realistic description of the actual sensory noise. This signal, with relatively low power, was added directly to the actual state variable θ in the feedback loop, therefore the rotation angle included in Eq. 7.15 for τ_a actually includes such contribution. On the other hand, the angle θ used in the formulation of τ_p (Eq. 7.14) corresponds to the actual ankle joint rotation, since passive control does not depend on feedback provided by sensory system.

7.1.2 Double link inverted pendulum model

While a single link inverted pendulum represent a typical model for postural control analysis, multi-link (or multi-segmental) models have been increasingly studied by researchers in the recent literature. They allow for studying the interaction among different body segments and can generally provide more realistic results. By visual examination of posturography trials, it is clear that most of the oscillations occur by rotation about the ankle joint, having the knee and hip fully extended. This behavior is known as ankle strategy. However, especially in elderly people, ankle strategy is often combined with hip strategy, producing larger movements of the thigh and of the trunk in order to directly control the CoM. Therefore, especially for studying such patients, multi-link systems represent a useful tool.

Figure 7.2 shows a representation of a double link inverted pendulum subjected to an external force. As for dynamic posturographic analyses, such force is applied to the back of the trunk, hence to segment 2. Segment 1 represents the fully extended lower limb. As for the single link inverted pendulum, the foot is integral with the fixed base of support. Each segment is defined by means of its inertial properties (mass m and rotational inertia I), length (l) and position of the CoM (d, defined as the distance between the segment CoM and the distal joint). The subscripts 1 and 2 refer to the segments. Length h_2 is the distance between perturbation's point of application and the hip joint. Ankle and hip joints are located respectively at points A and H. As for the single link model, this one only allows for studying the body motion in the sagittal plane, therefore it would be not suitable for analyzing the response to medio-lateral stimuli.

Analytical model

Since three segments are included, several free body diagrams can be represented and solved to evaluate the dynamics of this system (Fig. 7.3).

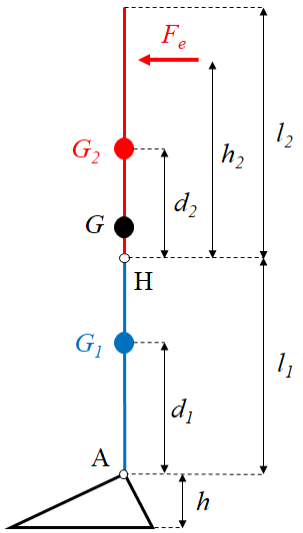

Figure 7.2: Representation of double link inverted pendulum model for postural analysis; blue and red segments represent respectively lower limb and trunk.

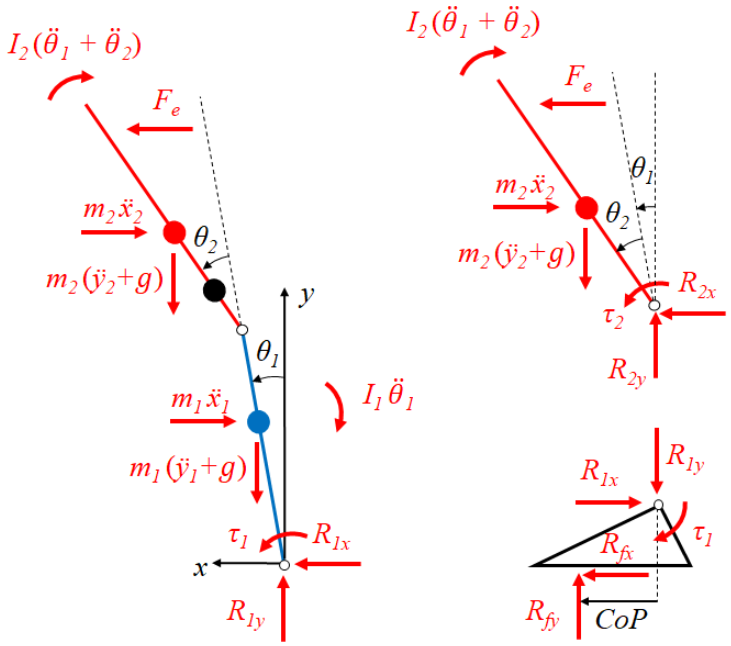

Figure 7.3: Free body diagrams of double link inverted pendulum model for postural analysis. Dot notation represents time derivative.

It is possible to write the following equations for the equilibrium of segments 1

and 2 altogether:

$$\tau_1 + m_1 g d_1 \sin\theta_1 + m_1 \frac{d^2 y_1}{dt^2} d_1 \sin\theta_1 - m_1 \frac{d^2 x_1}{dt^2} d_1 \cos\theta_1 - I_1 \frac{d^2\theta_1}{dt^2} + m_2 g(l_1 \sin\theta_1 + d_2 \sin(\theta_1+\theta_2)) + m_2 \frac{d^2 y_2}{dt^2}(l_1 \sin\theta_1 + d_2 \sin(\theta_1+\theta_2)) - m_2 \frac{d^2 x_2}{dt^2}(l_1 \cos\theta_1 + d_2 \cos(\theta_1+\theta_2)) - I_2 \left(\frac{d^2\theta_1}{dt^2} + \frac{d^2\theta_2}{dt^2}\right) + F_e(l_1 \cos\theta_1 + h_2 \cos(\theta_1+\theta_2)) = 0 \quad (7.16)$$

$$R_{1x} - m_1 \frac{d^2 x_1}{dt^2} - m_2 \frac{d^2 x_2}{dt^2} + F_e = 0 \quad (7.17)$$

$$R_{1y} - m_1 \frac{d^2 y_1}{dt^2} - m_1 g - m_2 \frac{d^2 y_2}{dt^2} - m_2 g = 0 \quad (7.18)$$

Rotation θ_1 is the angular position of the lower limb segment 1 (zero corresponds to vertical position), whereas θ_2 is the relative rotation of the trunk (segment 2) with respect to the lower limb segment. The dynamic equilibrium of segment 2 yields:

$$\tau_2 + m_2 g d_2 \sin(\theta_1+\theta_2) + m_2 \frac{d^2 y_2}{dt^2} d_2 \sin(\theta_1+\theta_2) - m_2 \frac{d^2 x_2}{dt^2} d_2 \cos(\theta_1+\theta_2) - I_2 \left(\frac{d^2\theta_1}{dt^2} + \frac{d^2\theta_2}{dt^2}\right) + F_e h_2 \cos(\theta_1+\theta_2) = 0 \quad (7.19)$$

$$R_{2x} - m_2 \frac{d^2 x_2}{dt^2} + F_e = 0 \quad (7.20)$$

$$R_{2y} - m_2 \frac{d^2 y_2}{dt^2} - m_2 g = 0 \quad (7.21)$$

As for the single link model, the dynamic equilibrium of the foot (subscript f) gives the following equations:

$$\tau_1 + R_{fx} h + R_{fy} CoP = 0 \quad (7.22)$$

$$R_{fx} - R1x = 0 \quad (7.23)$$

$$R_{fy} - R1y = 0 \quad (7.24)$$

To solve the dynamic equilibrium of the system, it is useful to write x and y (coordinates of any segment's CoM) in terms of θ. The following relations can be used for the two links:

$$x_1 = d_1 \sin\theta_1 \quad (7.25)$$

$$y_1 = d_1 \cos\theta_1 \quad (7.26)$$

$$x_2 = l_1 \sin\theta_1 + d_2 \sin(\theta_1 + \theta_2) \tag{7.27}$$

$$y_2 = l_1 \cos\theta_1 + d_2 \cos(\theta_1 + \theta_2) \tag{7.28}$$

Differentiation of Eqs. 7.25 to 7.28 is needed to calculate velocity and acceleration of each segment's CoM. CoP can be calculated by rearranging Eq. 7.22.

Modeling of ankle torque for a multi-link system

Similarly to the single link model, torque at each joint has been modeled as the sum of a passive and an active contributions (see Eq. 7.13). However, accordingly to [34], additional terms were added to the active torque, to take into account the coupling between the segments. For instance, a rotation at the hip joint not only affects the active torque exerted on the same joint, but also the one at the ankle. Such contributions are referred as indirect terms [39]. General formulations for passive and active torques are the following:

$$\tau_{p_i} = -k_{p_i}\,\theta_i - \beta_{p_i}\,\frac{d\theta_i}{dt} \tag{7.29}$$

$$\tau_{a_i} = -k_{a_{ii}}\,\theta_i - \beta_{a_{ii}}\,\frac{d\theta_i}{dt} - k_{a_{ji}}\,\theta_j - \beta_{a_{ji}}\,\frac{d\theta_j}{dt} \tag{7.30}$$

with $(i, j) = (1,2)$ for segment 1 and $(i, j) = (2,1)$ for segment 2. Although it was not highlighted as in 7.15, the angles in Eq. 7.30 are delayed and noisy to take into account the neuromuscular latency and sensory noise, similarly to what has been discussed previously for single link model.

7.1.3 Tuning and simulations

The models described in the previous sections were implemented in MATLAB® - Simulink® environment, then simulations were performed by customizing each model to the physical characteristics of each subject from the analyses carried out with the final AP prototype (section 6.3, first session). The parameters considered will be discussed in the following sections separately for single and double link models. The parameters related to passive response (k_p and β_p, see Eqs. 7.14 and 7.29) were set accordingly to the literature [76]. This represents of course an approximation, however stiffness and damping characteristics would likely not be really different among subjects with similar build and age. Similarly, sensory noise features and neuromuscular latency were set equally for the subjects [34]. On the other hand, active response parameters (k_a and β_a, Eqs. 7.15 and 7.30) could be really different, depending on the specific subject considered. For this reason, they were optimized by means of a least square procedure for each subject considered. The suitability of the optimization method to single link and multi-link based systems will be also discussed.

In each simulation, the model was subjected to the same external force that was recorded during experimental trial. For each subject, the average perturbation force was computed among the data recorded in laboratory and implemented in the model. The resulting CoP motion was compared to the average CoP displacement measured during experimentation. Residuals were calculated for each trial by evaluating the difference between the real and model responses for each time step, then the optimal active torque parameters were chosen by minimization of the sum of squares of the residuals (S_{min}), normalized by the number of time frames. Each simulation lasted 5 s to match the actual duration of experimental data. Since each clinical trial consisted of about 20 perturbations in sequence, it was necessary to segment data in order to get a synchronized set of perturbations and of responses. Then, an average force and an average CoP displacement was calculated and used for model validation.

Single link model

Figure 7.4 shows the typical results of the analysis for the single link inverted pendulum (linear) model. The analysis was performed for each subject tested

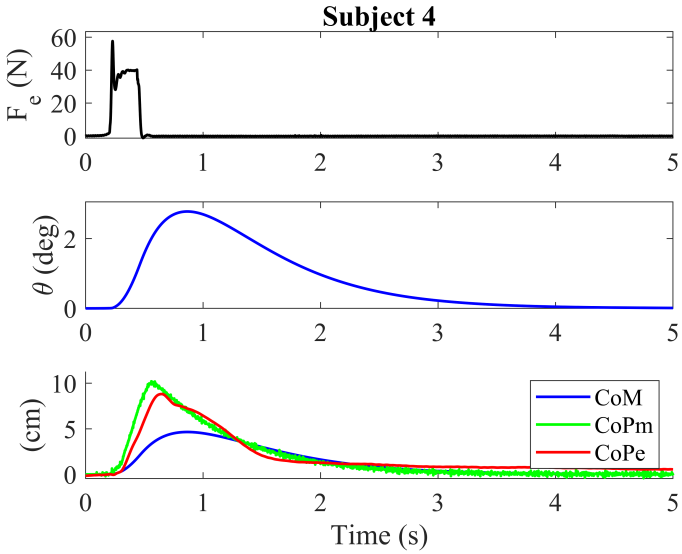

Figure 7.4: Perturbation force (top), sway (middle), CoM/CoP displacement (bottom) for linearized single link model, subject 4. CoPm and CoPe refer respectively to model and experimental results.

during the trials carried out with the final AP prototype in the constant force magnitude session (see section 6.3, first session). For the subject considered in Fig. 7.4, the following parameters were used: $m = 50$ kg, $l = 1.6$ m, $h = 0.1$ m, $d = 0.6l$, $I = ml^2/12$, $h_F = 1.2$ m. Rotational inertia was approximated by considering the

mass equally distributed along the whole segment and resulted similar to values found in the literature ([34, 76]). Passive torque parameters were set accordingly to [76] ($k_p = 280$ N m/rad, $\beta_p = 65$ N m s/rad). The simulation was stopped, hence it was not considered for further analysis, when CoP displacement exceeded the range [-0.1 - 0.2] m. This condition was relevant to avoid unrealistic behaviors that could affect the least square optimization procedure. Figure 7.5 shows the residuals for each combination of active torque parameters (k_a and β_a) tested for the same subject of Fig. 7.4. A first optimization was run for large ranges of the controller parameters, then they were narrowed to get more refined results (see Fig. 7.6). Active torque delay t_d was set to 90 ms for all simulations, similarly to [38].

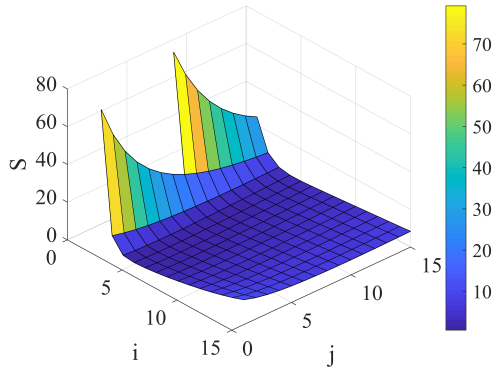

Figure 7.5: Residuals for several (k_a, β_a) combinations in large ranges of active parameters, $k_a = [100 - 1000]$ N m/rad, $\beta_a = [100 - 300]$ N m s/rad. i and j are the indexes corresponding to the different values of k_a and β_a tested.

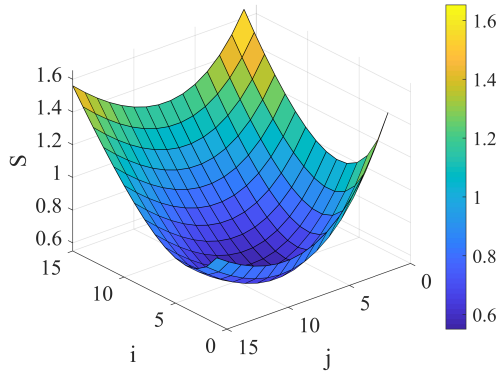

Figure 7.6: Residuals for several (k_a, β_a) combinations in large ranges of active parameters, $k_a = [300 - 450]$ N m/rad, $\beta_a = [100 - 180]$ N m s/rad. i and j are the indexes corresponding to the different values of k_a and β_a tested.

The model results presented in Fig. 7.4 refer to the linear model. However,

no significant differences were highlighted within the non-linear model (see Fig. 7.7). This result was likely related to the relatively low level of force impulses, that

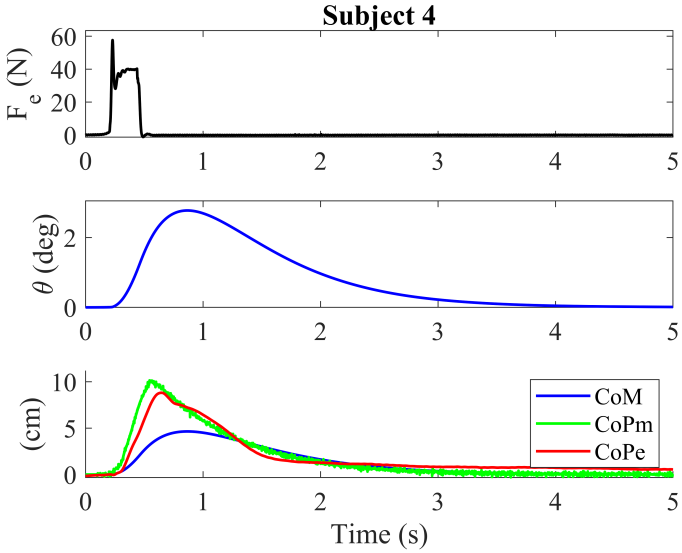

Figure 7.7: Perturbation force (top), sway (middle), CoM/CoP displacement (bottom) for non-linear single link model, subject 4. CoPm and CoPe refer respectively to model and experimental results.

was confirmed by the low values of θ and of CoP displacement. This result was confirmed for all the subjects. Figures 7.8 and 7.9 show the model output data for two more subjects.

Table 7.1 presents the values of k_a and β_a that were selected after minimization of the residuals. Only five subjects were included for sake of simplicity, however the others showed the same quality of fit between model and experimental CoP displacement. The active controller parameters were similar to data reported in the literature [12, 34], showing that the model was able to provide realistic information about postural control stability.

Subject	k_a (N m/rad)	β_a (N m s/rad)	S_{min} (cm^2)
4	342.86	140.00	0.55
7	485.71	121.43	0.33
11	485.71	171.43	0.42
12	550.00	242.86	0.17
15	678.57	214.29	0.40

Table 7.1: Active torque parameters for single link inverted pendulum model. S_{min} is the sum of squares of residuals.

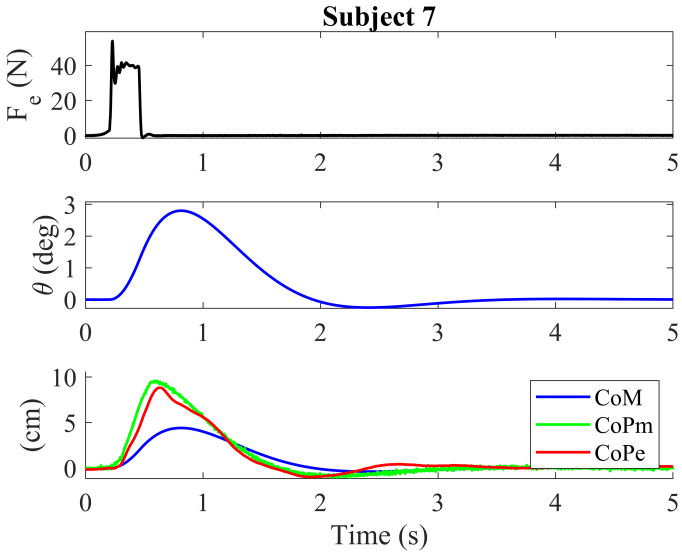

Figure 7.8: Perturbation force (top), sway (middle), CoM/CoP displacement (bottom) for linearized single link model, subject 7. CoPm and CoPe refer respectively to model and experimental results.

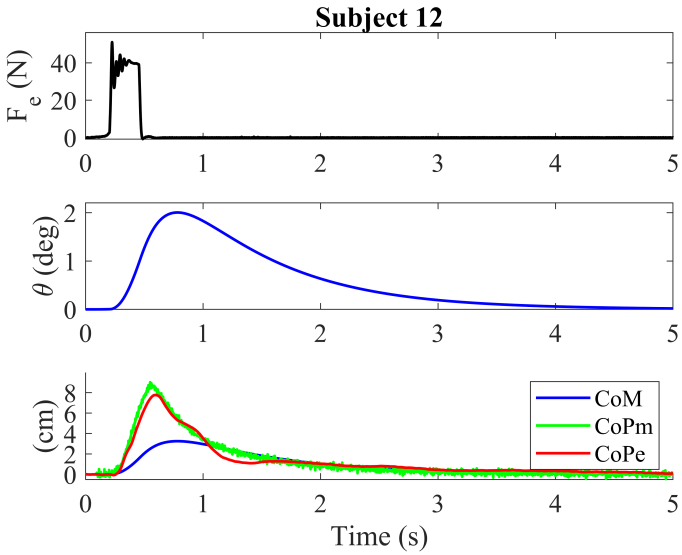

Figure 7.9: Perturbation force (top), sway (middle), CoM/CoP displacement (bottom) for linearized single link model, subject 12. CoPm and CoPe refer respectively to model and experimental results.

The validated model allowed for monitoring physical quantities that could not be directly measured during experimental trials. For instance, Figs. 7.10 and 7.11 show passive, active and total torques at the ankle joint for subjects 4 and 7.

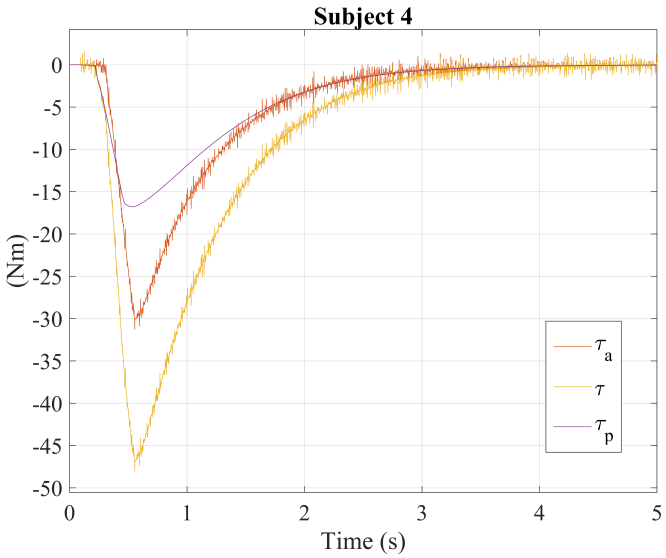

Figure 7.10: Passive τ_p, active τ_a and total torque τ obtained by single link model, subject 4.

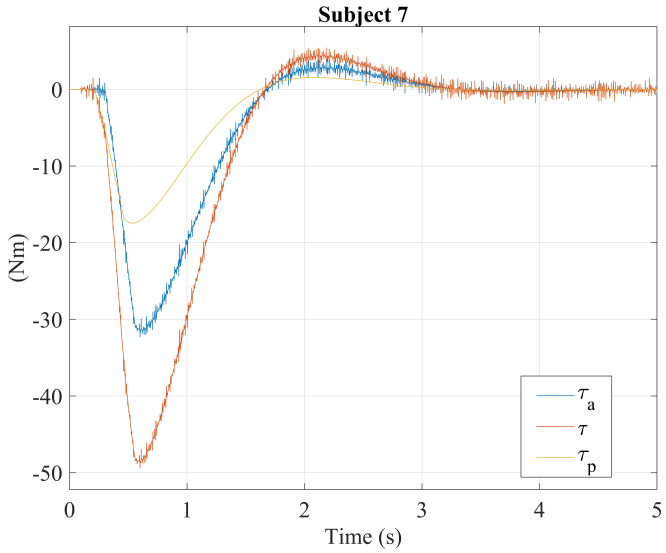

Figure 7.11: Passive τ_p, active τ_a and total torque τ obtained by single link model, subject 7.

Joint torque profiles can be useful to establish the amount of energy required by

the subject to regain balance, e.g. by integral of the torque vs joint rotation. This parameter is related to the ability of a subject to keep balance after an external perturbation. The peak torque value could also represent a likely indicator of such characteristics. However, such simple system does not consider hip joint, that would be also subjected to a passive and an active correcting torques. The results of simulations carried out on double link inverted pendulum are presented in the following section.

Double link model

Double link model was tuned on the same set of trials used for single link model. Since data available to characterize the subjects were still the same (total mass m, trunk + lower limb length l, ankle height h, perturbation level h_F), the parameters related to each segment had to be empirically extracted. For each subject, the mass and length of the lower body were calculated respectively as $m_1 = 0.33m$ and $l_1 = 0.45l$, whereas m_2 and l_2 were equal to the remaining parts. The distance between lower limb's CoM and ankle joint was set to $d_1 = 0.63l_1$, while trunk's CoM was located at a $d_2 = 0.3l_2$ distance from the distal (hip) joint. Those proportions were extracted by [39]. CoM of the whole body was calculated as the weighted sum of CoMs coordinates of both links. Similarly to the single link model, the rotational inertia for each segment was computed as $I = ml^2/12$. The distance between perturbation's point of application and hip joint was calculated as $h_2 = h_F - l_1$.

Regarding passive torque parameters, they were set to $k_{p_1} = 280$ N m/rad, $\beta_{p_1} = 65$ N m s/rad, $k_{p_2} = 150$ N m/rad, $\beta_{p_2} = 80$ N m s/rad. Time delays for active torque generation were set to $t_{d_1} = 60$ ms and to $t_{d_2} = 40$ ms respectively for θ_1 and θ_2. These parameters were obtained by the literature [34, 39]. The simulation was stopped when CoP displacement exceeded the range [-0.1 - 0.2] m. The same residuals iterative minimization described in previous section was implemented to find the optimal active torque parameters. However, the complexity of that process was significantly higher for the double link model, due to the increase of parameters from two to eight (Eq. 7.30, for each segment). Therefore, to reduce such complexity, four parameters were fixed ($k_{a_{12}}$, $\beta_{a_{12}}$, $k_{a_{21}}$, $\beta_{a_{21}}$) to values obtained from the literature [34]. These parameters were related to the cross-interaction between the rotation at one joint and the torque generated at the other joint. Therefore, only $k_{a_{ii}}$ and $\beta_{a_{ii}}$ (i = 1,2) were subjected to the optimization. It was highlighted indeed that the behavior of the model was far more significantly affected by variations of those parameters, whereas the other four controller parameters could be used only to refine the results.

Figures 7.12, 7.13 and 7.14 show the results of the model for three subjects (after tuning). The results for the same subjects are presented respectively in Figs. 7.4, 7.8 and 7.9 with single link model.

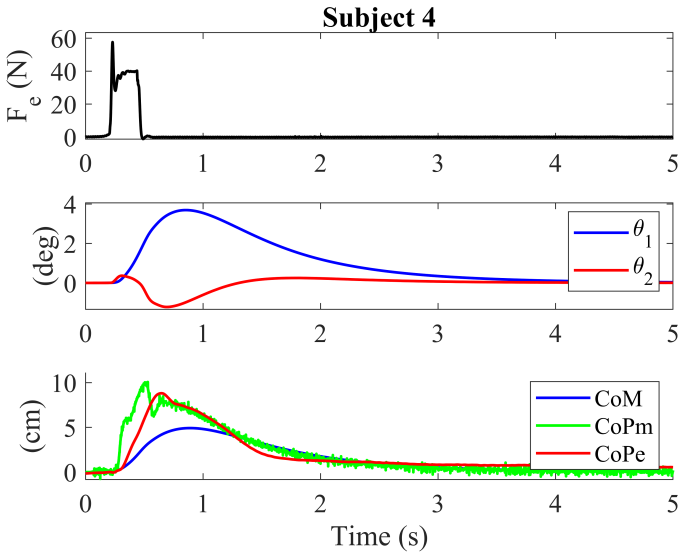

Figure 7.12: Perturbation force (top), sway (middle), CoM/CoP displacement (bottom) for double link model, subject 4. CoPm and CoPe refer respectively to model and experimental results.

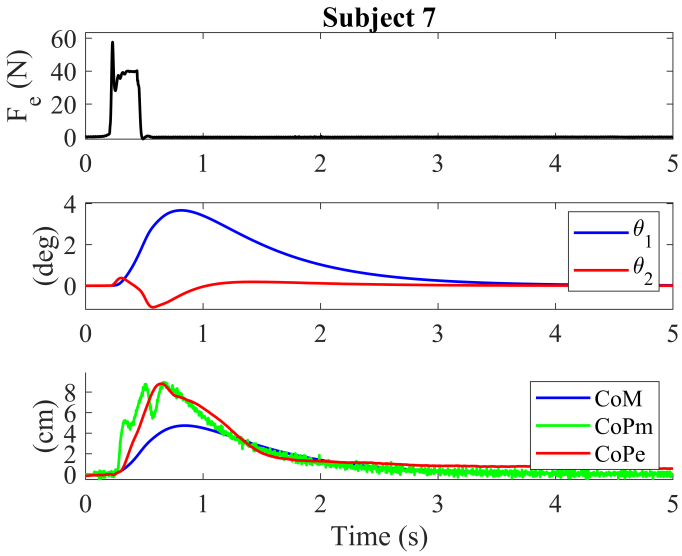

Figure 7.13: Perturbation force (top), sway (middle), CoM/CoP displacement (bottom) for double link model, subject 7. CoPm and CoPe refer respectively to model and experimental results.

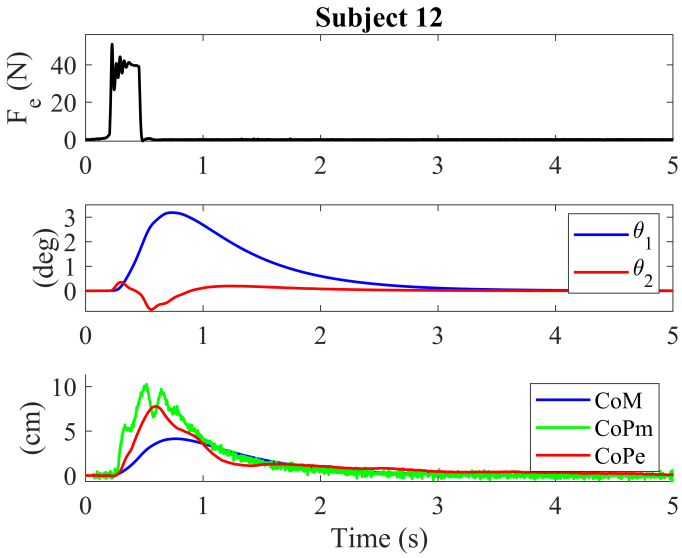

Figure 7.14: Perturbation force (top), sway (middle), CoM/CoP displacement (bottom) for double link model, subject 12. CoPm and CoPe refer respectively to model and experimental results.

Although the double link model could provide more information about postural response with respect to the single link model, it was not possible to achieve the same level of accuracy about CoP displacement. Table 7.2 shows the values of active torque parameters that were selected to minimize the residuals square sum S_{min}. By comparison with Table 7.1, the single link model showed better accuracy as signaled by lower residuals. The controller parameters obtained were comparable with data from the literature [34] and with the one obtained for single link model.

Subject	$k_{a_{11}}$	$\beta_{a_{11}}$	$k_{a_{22}}$	$\beta_{a_{22}}$	S_{min} (cm^2)
4	250	120	300	80	1.03
7	262.5	100	650	80	0.69
11	375	112.5	600	80	0.61
12	312.5	122.5	750	90	0.78
15	550	122.5	1125	90	0.62

Table 7.2: Active torque parameters for double link inverted pendulum model. S_{min} is the sum of squares of residuals. $k_{a_{ii}}$ are expressed in N m/rad, whereas $\beta_{a_{ii}}$ are expressed in N m s/rad.

Figures 7.15 and 7.16 show the total, passive and active torques calculated at ankle and hip joints for two subjects.

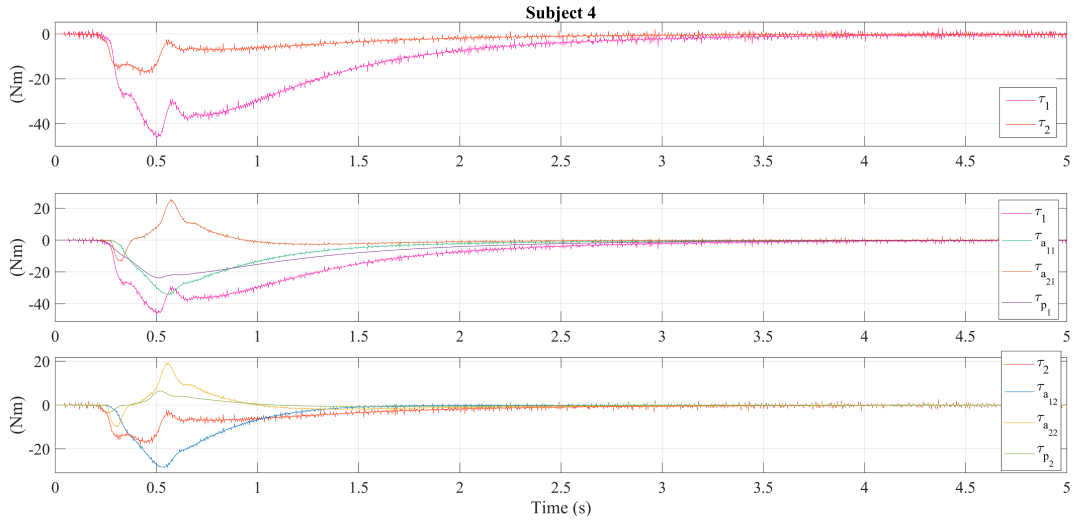

Figure 7.15: Passive τ_p, active τ_a and total torque τ obtained by double link model, subject 4. Subscripts 1 and 2 refer respectively to ankle and hip joints.

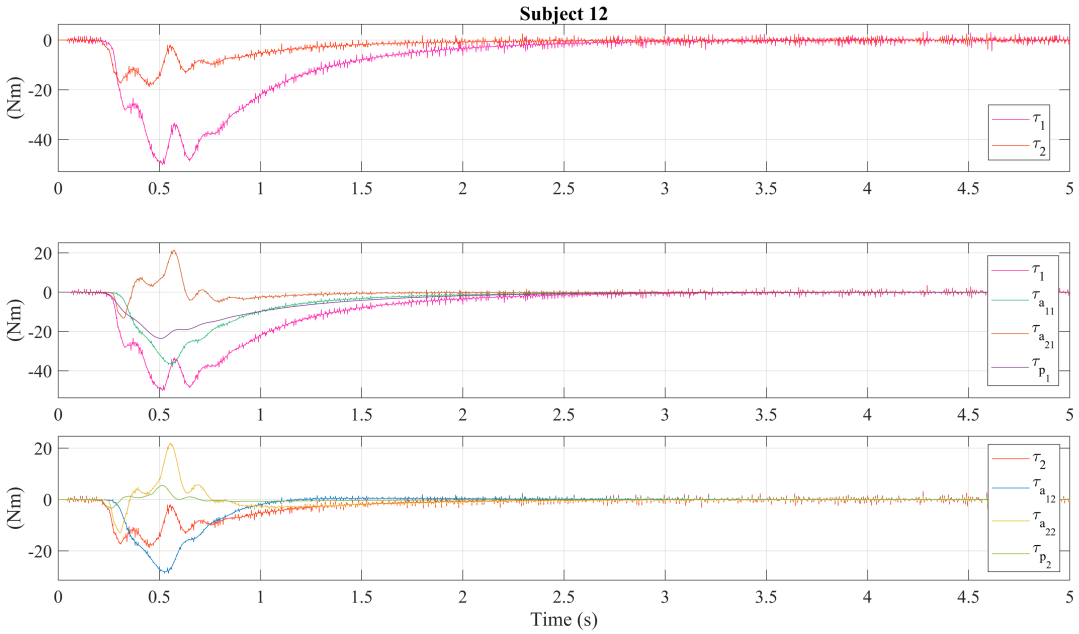

Figure 7.16: Passive τ_p, active τ_a and total torque τ obtained by double link model, subject 12. Subscripts 1 and 2 refer respectively to ankle and hip joints.

With respect to the results presented in Figs. 7.10 and 7.11, double link model can provide a far more complex set of data about the ability of a subject to keep or regain balance after an external perturbation. Similarly to the single link model,

torques estimation allows for calculating the energy required to stabilize the system. In all subjects tested, the ankle was always subjected to an higher torque than the one obtained for the hip joint. Ankle peak torque was similar to the one observed with the single link model.

Discussion

The implementation of two typical models used to describe human postural control showed that, in both cases, the system could show realistic results in terms of CoP displacement.

The difficulty to find optimal controller parameters for double link model can be likely related to the lack of additional measurements from experimental trials. Since the minimization iterative procedure could only use the experimental CoP signal as the target of the optimization, it was not possible to determine effectively the four active torque parameters required to stabilize the system. In order to improve the matching between model and experimentation, it could be necessary to introduce new measurements into the optimization procedure as additional targets. For instance, since the model can evaluate trunk sway in the sagittal plane, it would be feasible to measure (even approximately) such variable during experimental trials, e.g. by means of inertial measurement units, stereophotogrammetry or even manual inspection of videos. Another optimization target could be represented by tangential forces on the base of support: even though they were available during the trials performed (thanks to the force platform used), the quality of those signals was not good enough to perform such process. On the other hand, CoP displacement could be measured more effectively and hence used for model validation.

The worse matching between simulated and experimental data observed for double link model could also be related to the actual stabilization strategy implemented by the subjects. Since a double link model is intrinsically less stiff than a single link inverted pendulum, the introduction of hip joint rotation (θ_2) could irreparably affect the stability of the system and matching with the real experimental data if a predominant ankle joint strategy was used. On the other hand, a single link inverted pendulum model would only be subjected to such strategy and could become eventually more accurate than the double link model. Moreover, it could be also more easily tuned, as shown in the previous paragraph. Since all the subjects were similar in terms of build and age, they likely shared the same stabilizing mechanisms, which is predominantly focused on ankle strategy for young people. To confirm this observation, it will be necessary to test healthy older people or patients with relevant diseases affecting postural control. Since elderly people typically combine ankle and hip strategies, thus evidencing large movements of upper and lower parts of the body to keep their CoM as stable as possible, a double link inverted pendulum could likely provide more realistic results in such condition. However, as stated above, it would be still necessary to improve the optimization procedure, e.g. by

providing additional measurements about the state of the system.

The active torque parameters found by iterative optimization, related to the subject's specific ability to keep balance when an external perturbation is applied, were compatible with data presented in the literature. Although double link inverted pendulum could provide additional insight of the mechanisms adopted by the central nervous system to achieve postural stability, a better matching between the model and experimental data was obtained for the simpler and theoretically less accurate single link inverted pendulum model. This result is likely related to the difficulty to find the many unknown parameters required to characterize active postural response in multi-link models when only CoP measurement is available. Moreover, a more relevant contribution of ankle strategy (with respect to the hip one) could also determine the better correlation with the single link model rather than with the intrinsically more compliant double link model. To improve postural control system identification in those models, alternative techniques based on frequency domain, as the one presented in the following section, can be implemented.

7.2 Analysis of postural control in frequency domain

As shown in previous section, human balance control is a complex process that involves the interaction among several sensory systems and the central nervous system, whose action drives the musculoskeletal system to recover balance after an external perturbation or to stabilize posture in quite standing (Fig. 7.17). As dis-

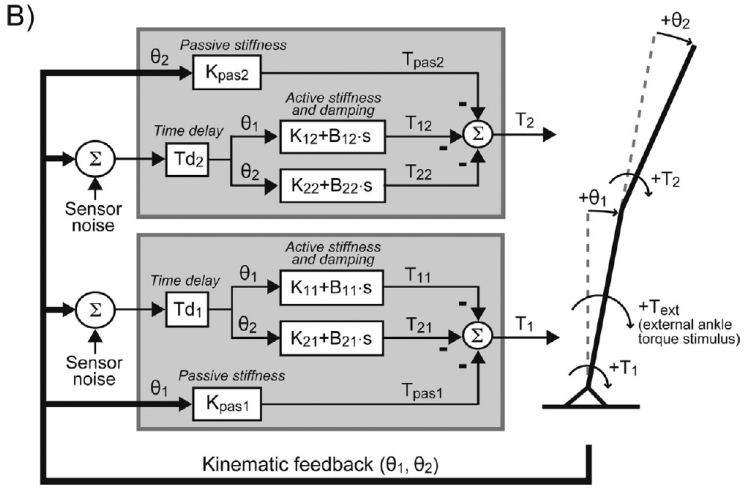

Figure 7.17: Postural control system modeled as a closed-loop system [34].

cussed for the linearized inverted pendulum model (see section 7.1.1), it is possible to describe the behavior of such complex system with the methods of linear systems

analysis, considering the body sway θ as the output and the ankle torque τ as the input. The external perturbation F_e is considered an output disturbance since it affects directly the body sway. In particular, since posture is continuously adjusted by sensory feedback, techniques based on the study of closed-loop systems (CLSs) can be implemented despite the obvious approximation [38].

Since a CLS can be easily described by a transfer function, several methodologies have been developed to study and to identify such systems in the frequency domain. As reported in [19, 38], transfer functions can be studied to evaluate the relationship between response (e.g. CoM, body sway) and the stimulus in terms of gain (ratio of the amplitudes) and phase (relative timing of response with respect to the stimulus) as functions of frequency of the stimulus. Several transfer functions can be evaluated and discussed. In this section, methods for CLS identification and analysis, aimed at the study of postural control, will be presented.

7.2.1 Identification techniques

As presented in [38, 39], CLS identification is generally performed by means of:

- indirect approach;
- joint input-output approach.

A third direct approach has been considered as erroneous for CLS analysis since it considers the system's input (torque) and output (sway) separately, which is typically true for open-loop system analysis. Indirect and joint input-output approaches are instead based on the evaluation of input and output sensitivity to the external disturbance (as functions of stimulus frequency), and allow for the identification of the plant (physical system) and of the (neuromuscular) controller. Both approaches require the application of external perturbations in terms of mechanical disturbances (directly to the body of the subject) or sensory noise in order to perform balance control characterization. Then, the resulting frequency response functions (FRFs) can be used for:

- non-parametric closed-loop identification;
- model parameter identification.

The latter requires modeling of the control action and minimization of the error between the controller FRF obtained in the model and the FRF resulting from non-parametric closed-loop identification on experimental data [19]. In this study, the first approach was chosen since it allows for studying the properties of balance control without the need for additional modeling and processing. However, the same methodology could be extended in the future for parametric identification of models aimed at describing the mechanisms of postural control in details.

In the following sections, the functions and FRFs considered for postural control model identification are presented.

Sensitivity functions

Indirect approach, which has been already used in studies regarding postural control [19], estimates output (S_{out}) and input (S_{in}) sensitivity to external perturbations with the following relations [38]:

$$S_{out}(f) = \frac{CSD(F_{ext}, \theta)}{PSD(F_{ext})} \tag{7.31}$$

$$S_{in}(f) = \frac{CSD(F_{ext}, \tau)}{PSD(F_{ext})} \tag{7.32}$$

CSD and PSD in Eqs. 7.31 and 7.32 are respectively the cross-power spectral density and power spectral density functions, f is the frequency. CSD is the Fourier transform of cross-correlation between perturbation F_{ext} and sway θ (Eq. 7.31) or torque τ (Eq. 7.32), whereas $PSD(F_{ext})$ is the Fourier transform of the autocorrelation of external disturbance. Power spectral density of a signal refers to the energy distribution per unit of time over the spectrum. Numerically, (cross) power spectra can be computed starting from the discrete Fourier transform (DFT) of (cross) correlation time series (details in [19]).

Given the power spectrum of the external perturbation $PSD(F_{ext})$, S_{out} and S_{in} can be evaluated if θ and τ are respectively known. Since body sway is directly related to CoM displacement (see section 7.1.1), the same relation reported in Eq. 7.31 can be extended to evaluate the output sensitivity in terms of CoM displacement rather than sway. Similarly, Eq. 7.32 can be expressed in terms of CoP displacement rather than in terms of torque τ, as demonstrated by rearrangement of Eq. 7.6 by considering that $R_x h$ contribution is typically negligible:

$$CoP = \frac{-\tau - R_x h}{mg} \simeq \frac{-\tau}{mg} \tag{7.33}$$

As reported in [38], expressions in Eqs. 7.31 and 7.32 can be subsequently used to retrieve knowledge about the plant and the controller.

Neuromuscular controller dynamics

Joint input–output identification approach allows for the evaluation of the neuromuscular controller dynamics without any a priori knowledge of the plant and of the controller. It combines input and output sensitivity functions in the following manner:

$$H_{con}(f) = \frac{CSD(F_{ext}, \tau)}{CSD(F_{ext}, \theta)} \tag{7.34}$$

As discussed in [38], this relation is rigorously true only for linear time-invariant (LTI) systems. Since postural control system can only be approximated as a linear

CLS, Eq. 7.34 provides an approximation of the controller FRF H_{con}. The magnitude of the FRF $|H_{con}|$ is often normalized by *gravitational stiffness* term mgd (Eq. 7.3 where m is the mass, g is the gravitational acceleration and d is the distance between the ankle joint and CoM [17, 19, 38]), that should always be lower than the sum of active and passive feedback to achieve stability. This transfer function includes the contributions of active and passive (intrinsic) control strategies. To distinguish between each contribution, EMG measurements are required [38]. To improve FRF estimation, perturbation should have enough power in the spectrum range used for frequency analysis.

To verify the accuracy of linear modeling, a coherence function $C(f)$ can be estimated as [19]:

$$C(f) = \sqrt{\frac{|CSD(F_{ext}, \theta)|^2}{PSD(F_{ext})PSD(\theta)}} \tag{7.35}$$

This function, ranging between 0 and 1, represents a measurement of linearity since $|CSD(F_{ext}, \theta)|^2$ can be directly computed as the product between $PSD(F_{ext})$ and $PSD(\theta)$ for a LTI system ($C(f) = 1$, for any frequency f). Therefore, $C(f)$ is useful to check the spectrum range that corresponds to linear-like behavior of the system.

7.2.2 Step-by-step application of the analysis on experimental data

In this section, some examples of the results given by frequency domain analysis detailed so far are presented. Experimental data were extracted from the 20 subjects set obtained during the trials performed with the first AP prototype (see section 3.5). Each subject was tested in two separate sessions with randomized perturbations (up to 20) at thoracic and lumbar levels. Two different impulses were selected, respectively equal to 12 N s and 18 N s.

Figure 7.18 shows the raw time series of perturbation force F_e, CoP_{AP} (antero-posterior) and CoP_{ML} (medio-lateral) displacements for a subject. Each signal was segmented to get two isolated sets, each one corresponding to a level of impulse. The result of this segmentation for both perturbation and response signals is presented in Fig. 7.19. In this figure, subscript 1 or 2 refers respectively to 12 N s and to 18 N s perturbations. As highlighted in Figs. 7.18 and 7.19, medio-lateral displacement was always significantly lower than antero-posterior one. However, they were combined to obtain the whole CoP displacement (i.e. the response) in order to avoid inaccuracy related to the orientation of the body of the subjects.

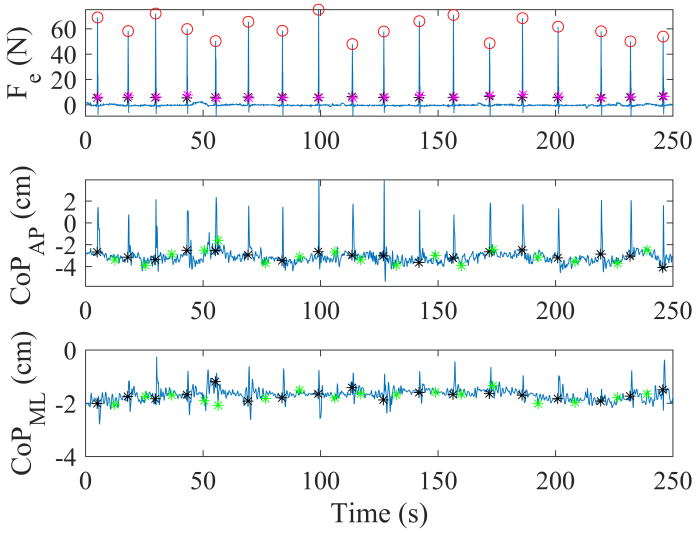

Figure 7.18: Perturbation force F_e (top), CoP_{AP} (antero-posterior, middle) and CoP_{ML} (medio-lateral, bottom) displacements. Red circles are used to highlight each perturbation, black and green symbols in CoP measurements represent respectively the time frames limiting each response.

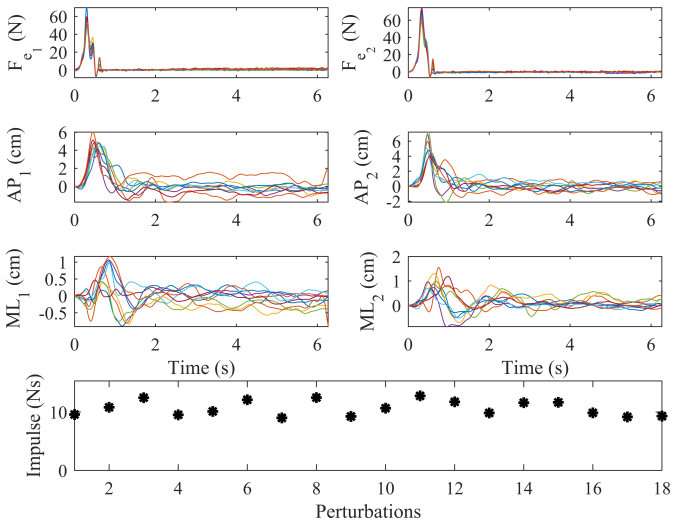

Figure 7.19: Segmented signals of perturbation force F_e, CoP_{AP} (antero-posterior) and CoP_{ML} (medio-lateral) displacements. Subscripts 1 and 2 refer respectively to 12 N s and 18 N s stimuli. Impulse values for each perturbation are shown at the bottom.

Then, discrete Fourier transform of each perturbation and response signal (lasting about 6 s) was performed with the *fft* function in MATLAB. Since the signals were originally sampled at 200 Hz, a significant amount of points (2048) were selected for the DFT to improve spectrum resolution at low frequency. For each level of impulse, maximum, average and minimum values of the spectra were computed at each frequency (see Fig. 7.20). This analysis confirmed that both the perturbation signals and the responses had limited bandwidth, up to 8 - 10 Hz for the former and up to 3 - 5 Hz for the latter. This result is coherent with the literature [19, 39].

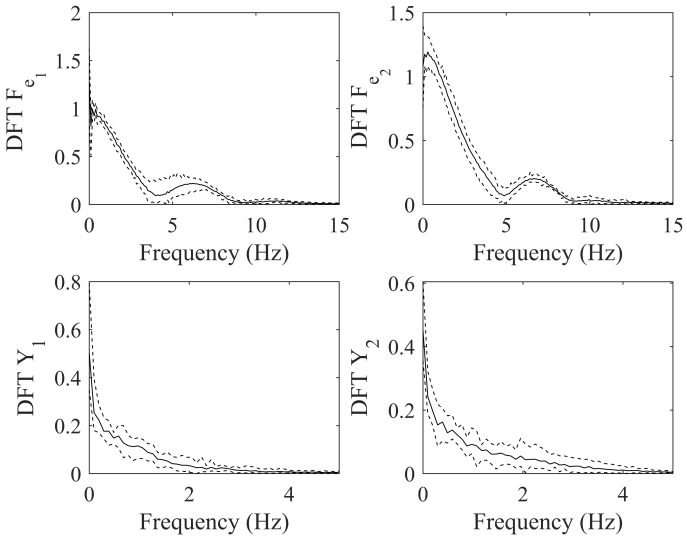

Figure 7.20: Discrete Fourier Transform of perturbation force (top) and of CoP displacement (bottom). Average spectra are shown in solid lines, dashed lines for minimum and maximum spectra. Subscripts 1 and 2 refer respectively to 12 N s and 18 N s stimuli.

Each perturbation and response signal was then processed with the *pwelch* function in MATLAB to calculate PSD. Since CoM (θ) data were not available (only the CoP could be reconstructed by means of force platform), it was not possible to evaluate the output sensitivity (Eq. 7.31) and controller dynamics (Eq. 7.34). On the other hand, the input sensitivity (of CoP displacement with respect to the external perturbation F_e) could be calculated with Eq. 7.32, starting from the CSD of the perturbation and of CoP displacement [38]. Figure 7.21 shows cross-spectral power density for the two levels of impulse tested, whereas the input sensitivity is presented in Fig. 7.22.

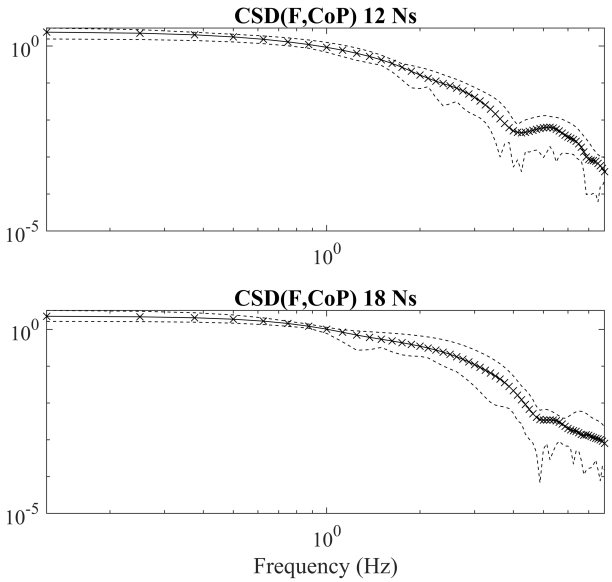

Figure 7.21: Cross-spectral power density of perturbation force and CoP displacement in 12 N s and 18 N s stimuli. Average power spectra are shown in solid lines, dashed lines for minimum and maximum power spectra.

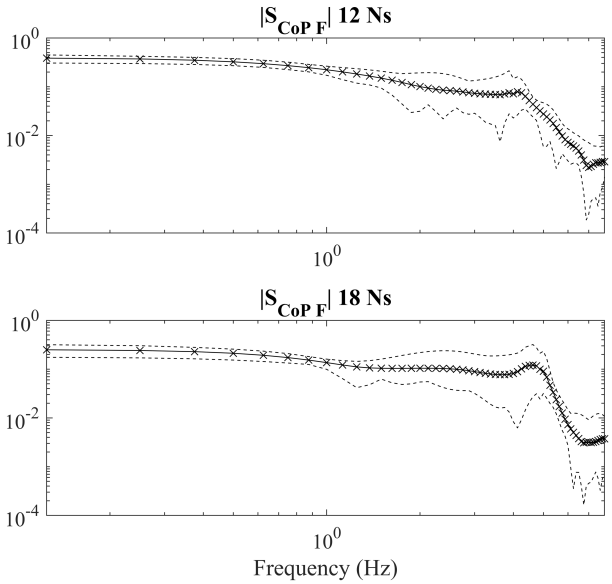

Figure 7.22: Magnitude of input sensitivity functions of CoP displacement with respect to perturbation force for an adult subject, 58 years old, BMI 19.0. Average FRFs for 12 N s and 18 N s stimuli are shown in solid lines, minimum and maximum FRFs are presented with dashed lines.

In both figures, average, maximum and minimum of the FRFs magnitude are represented. The shape of input sensitivity functions was coherent with data reported in the literature [38], exhibiting a *low pass filter*-like behavior. However, the Authors in [38] designed differently the external perturbation, that consisted in a random signal low-pass filtered in order to put significant energy in the system up to 4.5 Hz. For this reason, FRFs shown in [38] were represented within a more limited range with respect to the one considered in this work (up to 10 Hz).

The same trends for perturbations and responses PSD, as well as for the input sensitivity functions, were obtained for the other subjects. Figures 7.23 and 7.24 show the FRFs obtained for two different subjects. With respect to the subject considered in Figs. 7.18 to 7.22, who was an adult, 58 years old, with low BMI (19.0), the subject represented in Fig. 7.23 had similar age (57 y) but significantly higher BMI (27.7), whereas the one in Fig. 7.24 had still low BMI (20.8) but was younger (25 y).

Nonetheless, the results obtained for the three subjects did not allow for extracting significant differences between the FRFs and did not correlate with age and BMI variations. As already discussed in the literature, it is clear that more consistent changes in the response as well as in the information provided by frequency-based analyses are expected in populations consisting of elderly people and of patients with neuromuscular disorders affecting postural control. However, data provided by non-parametric identification techniques as the one shown in this section enables clinicians and researchers to get additional information about postural stability without the need for additional and complex modeling of postural control [19]. Since the methodology has been already validated and used in recent studies (e.g. [34, 39]), it seems reasonable to adopt this technique also for posture analyses based on the direct application of sudden perturbations, as the one presented in this work, that are not commonly covered in the literature. Given that the methodology has been developed for the analysis of closed-loop linear systems based on sensory feedback, it is strictly required to design the perturbation system to be unpredictable in order to rule out feed-forward mechanisms [38]. In the following section, the application of this methodology to the postural control models previously described is presented and discussed.

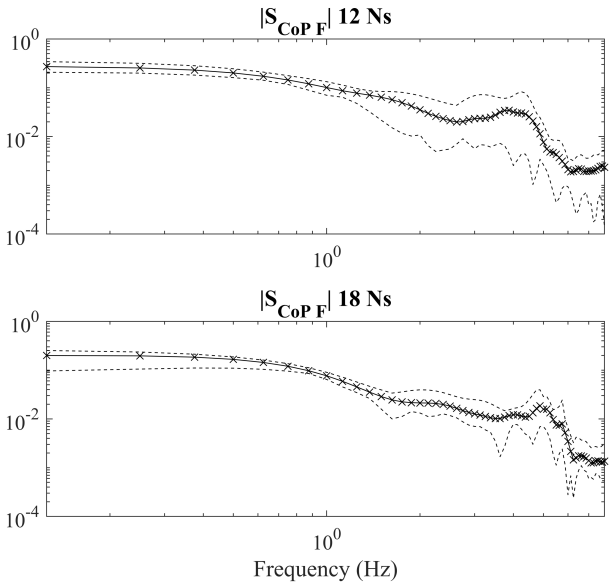

Figure 7.23: Magnitude of input sensitivity functions of CoP displacement with respect to perturbation force for an adult subject, 57 years old, BMI 27.7. Average FRFs for 12 N s and 18 N s stimuli are shown in solid lines, minimum and maximum FRFs are presented with dashed lines.

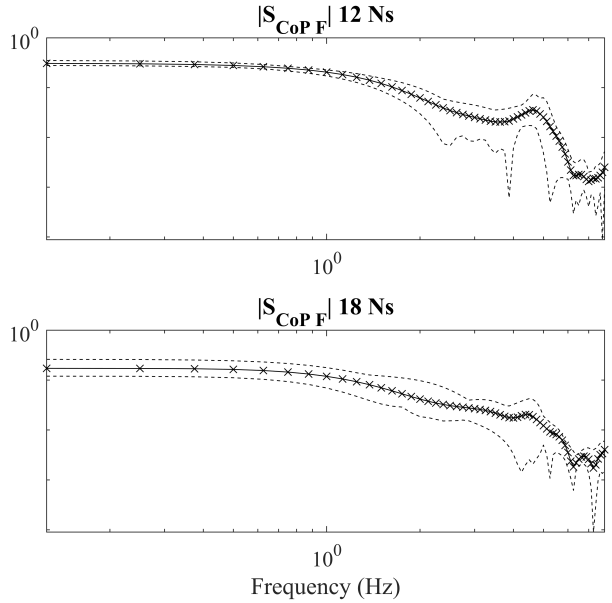

Figure 7.24: Magnitude of input sensitivity functions of CoP displacement with respect to perturbation force for a young subject, 25 years old, BMI 20.8. Average FRFs for 12 N s and 18 N s stimuli are shown in solid lines, minimum and maximum FRFs are presented with dashed lines.

7.2.3 Application of non-parametric identification techniques to postural control models

Frequency domain analysis can be applied to postural control models for tuning or identification purposes. In this study, the first application was considered to support the tuning of models presented in section 7.1, i.e. the single and double link inverted pendulum models. As discussed in section 7.1.3, active controller parameters were tuned to optimize the matching between the model and experimental responses in terms of CoP displacement. However, the models could be similarly tuned by minimization of the residuals between the simulated and measured FRFs, as proposed in [19].

Since only CoP displacement was measured during trials, input sensitivity (CoP displacement to external disturbance, Eq. 7.32) was calculated for both model and experimental data to verify the goodness of fit. Then, the tuned model was used to calculate output sensitivity (of CoM displacement/body sway to external disturbance, Eq. 7.31) and neuromuscular controller dynamics FRFs. The latter could be evaluated both strictly applying Eq. 7.34, hence considering the torque τ calculated by the model as the input, or by choosing CoP displacement, that is directly related to torque as previously discussed (Eq. 7.33). The second approach, also adopted in [38], is preferable since CoP displacement can be directly measured whereas joint torque can only be estimated by modeling.

Coherence function was also calculated to verify the hypothesis of linearity (see Eq. 7.35). This methodology was applied to both single and double link inverted pendulum models for several healthy subjects tested with final AP prototype (section 6.3). Besides for tuning purpose, this methodology was implemented also to compare FRFs resulting from posturographic trials based on the AP, that considered the direct application of impulsive stimuli, with data from the literature, that are typically based on the sliding or tilting of the base of support with pseudorandom acceleration waveforms.

Single link inverted pendulum model

Similarly to the simulations presented in 7.1.3, the behavior of single link nonlinear model was studied by considering the perturbation force measured during experimental trials as input. The active controller parameters were set accordingly to Table 7.1, that were selected by minimization of the residuals evaluated between model and experimental CoP displacement. Figure 7.25 shows DFT of perturbation F_e, modeled CoP displacement $CoPm$, experimental (average) CoP displacement $CoPe$ and (model) CoM displacement. As highlighted in Fig. 7.26, $CoPm$ and $CoPe$ spectra were quite similar and this result was confirmed for all the subjects.

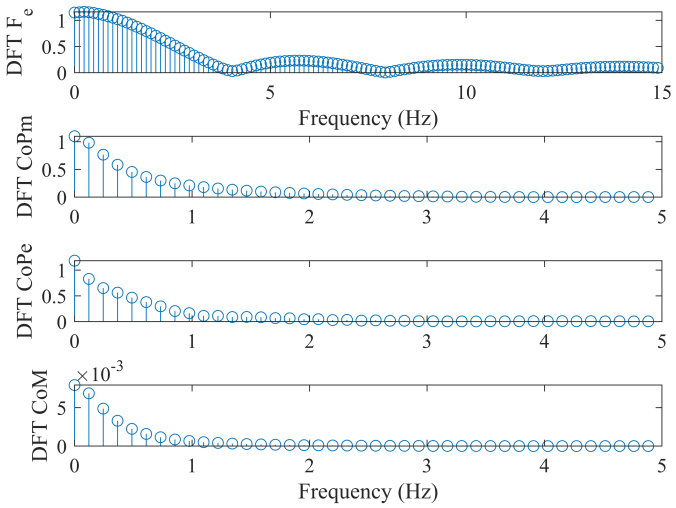

Figure 7.25: Discrete Fourier Transform of signals for single link inverted pendulum model. Top to bottom, spectra of perturbation force, modeled CoP $CoPm$, experimental CoP $CoPe$ and CoM.

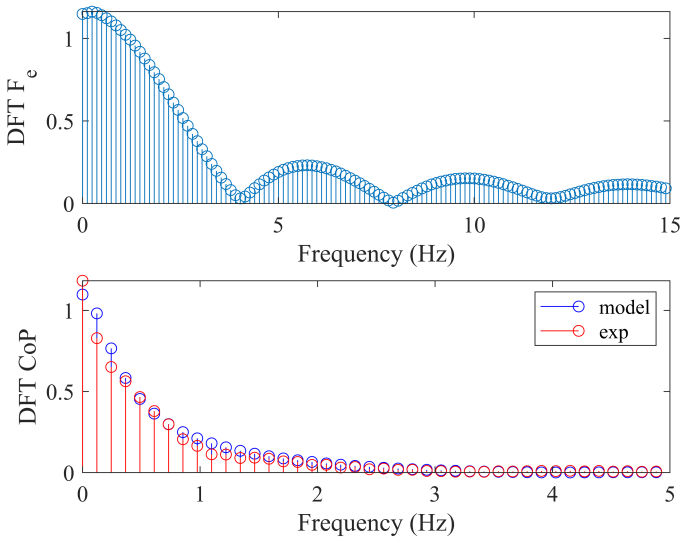

Figure 7.26: Discrete Fourier Transform of force perturbation (top) and of CoP displacement (bottom), single link inverted pendulum model.

Good fit between model and experimentation was confirmed by comparison of the power spectral densities (see Fig. 7.27) up to 5 Hz. As shown in Fig. 7.26, CoP displacement spectrum had significant frequency content up to 2.5 - 3 Hz, therefore

the limited matching between power spectra could be related to *high* frequency noise.

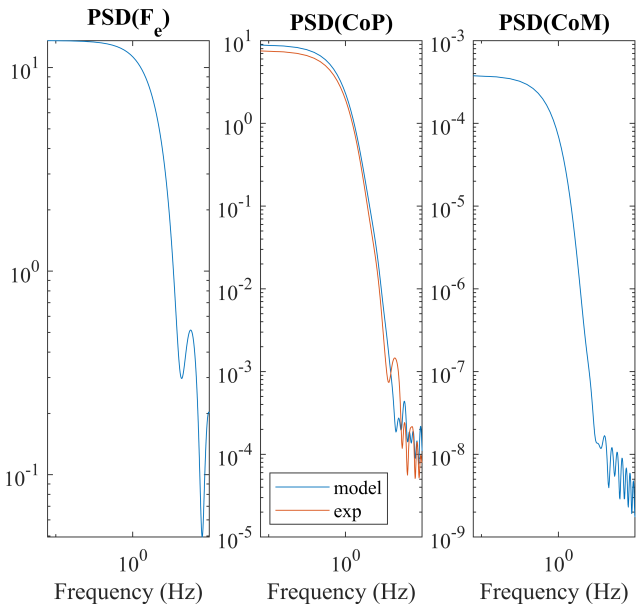

Figure 7.27: Power spectral density of force perturbation (left), CoP displacement (center) and CoM displacement (right), single link inverted pendulum model.

Input S_{in} and output S_{out} sensitivity functions to external perturbation were computed for model and experimental data, and the results are presented in Fig. 7.28 in terms of FRFs magnitude and phase up to 5 Hz. Similarly to Fig. 7.27, good matching between simulated and measured data was evidenced. Moreover, the sensitivity functions showed the same trend presented in the literature [38]. S_{out} was always lower than S_{in}, coherent with CoM displacement being shorter than CoP one (see Fig. 7.4).

Then, neuromuscular controller dynamics H_{con}, normalized by gravitational stiffness, was calculated, as well as coherence function C. Controller dynamics was evaluated by considering CoP displacement rather than torque τ in Eq. 7.34. The results are presented in Fig. 7.29. Controller FRF magnitude, as reported in [19, 38], showed an increasing trend after 1 - 1.5 Hz. Phase lag showed instead a two-phase behavior, coherently with [38]. Figure 7.29 shows controller dynamics calculated by considering experimental as well as modeled CoP displacement. Quite good matching was highlighted between the two curves, especially up to 3 - 3.2 Hz. However, discrepancy between the curves for higher frequency is consistent with the differences among the power spectral densities shown in Fig. 7.27. The coherence function (Fig. 7.29, bottom) showed very high level of linearity ($C > 0.8$) between 1.55 Hz and 2.9 Hz, suggesting to limit the analysis above 1 - 1.5 Hz. With respect to data from literature [19], it should be highlighted that data obtained in this

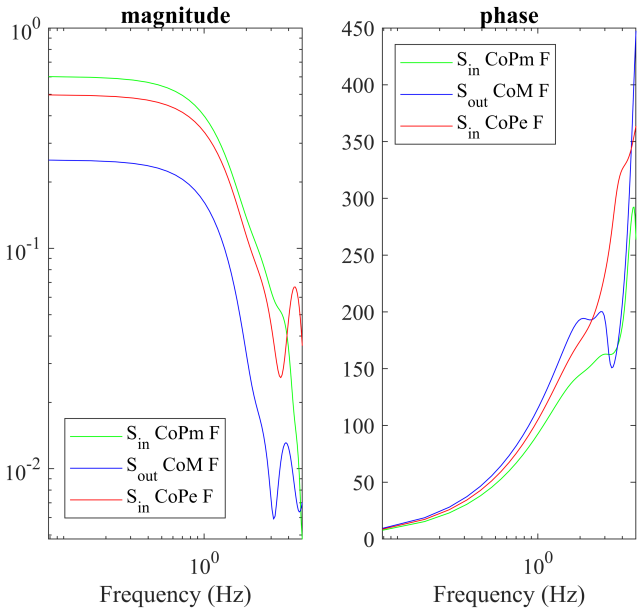

Figure 7.28: Magnitude (left) and phase (right) of input S_{in} and output S_{out} sensitivity functions to external perturbation, single link inverted pendulum model.

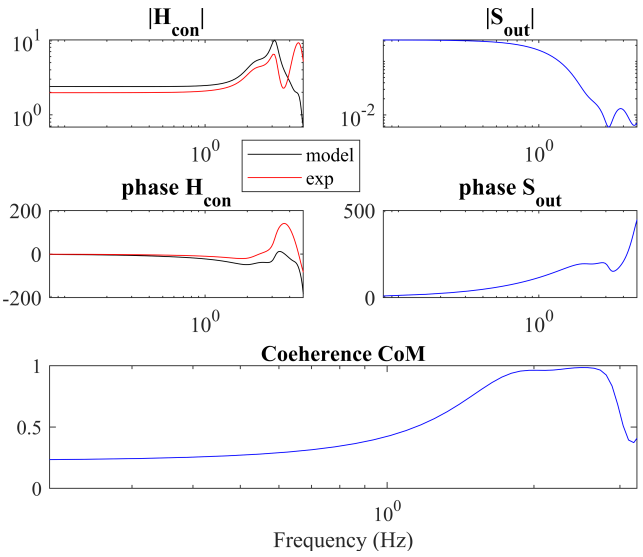

Figure 7.29: Magnitude and phase of controller dynamics H_{con} (left) and of output sensitivity function S_{out} (right) for single link inverted pendulum model by considering CoP displacement as input. Coherence function is shown at bottom.

study were shifted at higher frequency. This could probably depend on the characteristics of the perturbation signal: whereas the one controlled by the AP was

an impulsive force signal lasting 150 - 200 ms, data from literature were typically obtained with pseudorandom waveforms stimuli with almost flat spectrum between 0 and 5 Hz. For this reason, the response evoked and analyzed in this work could have significant power at higher frequency with respect to the bandwidth explored by studies of other researchers.

Finally, controller dynamics calculation was repeated by considering the ankle torque τ rather than CoP displacement as the input. As discussed in previous section, this approach is not commonly chosen since torque cannot be easily measured, whereas CoP can be monitored with a force platform. Thanks to the model, however, joint torque can be computed. The results presented in Fig. 7.30 showed the same trends for FRF magnitude and phase reported in Fig. 7.29 with limited variations. The magnitude $|H_{con}|$ was simply scaled, whereas phase lag started from 180° (rather than 0°) since τ and CoP displacement have opposite sign convention.

The results presented so far for subject 4 were confirmed for all of the other (up to 20) subjects tested. Figures 7.31 to 7.34 show output sensitivity, controller dynamics FRFs and coherence functions for four more subjects among the set of 20 tested with the final AP prototype.

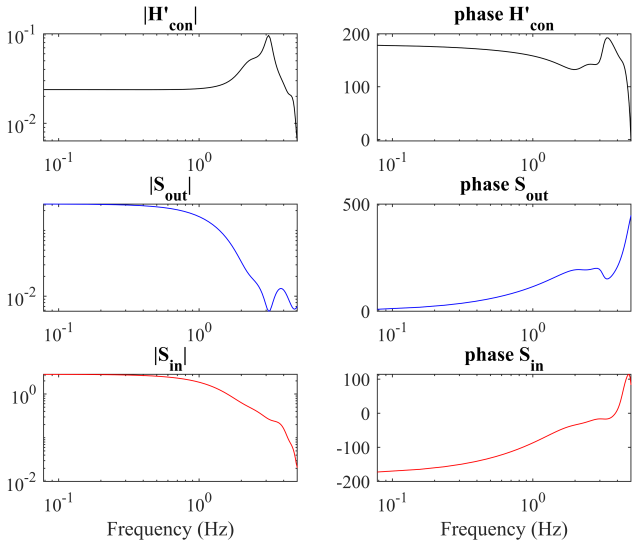

Figure 7.30: Magnitude and phase of controller dynamics H_{con} (left) and of output sensitivity function S_{out} (right) for single link inverted pendulum model by considering τ as input. Coherence function is shown at bottom.

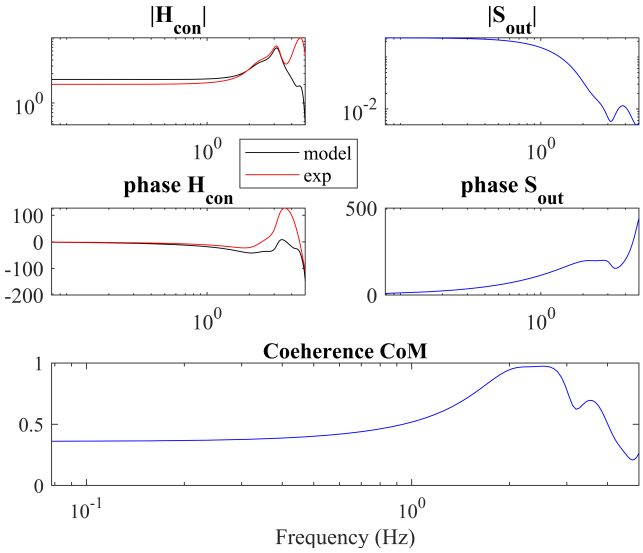

Figure 7.31: Magnitude and phase of controller dynamics H_{con} (left) and of output sensitivity function S_{out} (right) for single link inverted pendulum, subject 7. Coherence function is shown at bottom.

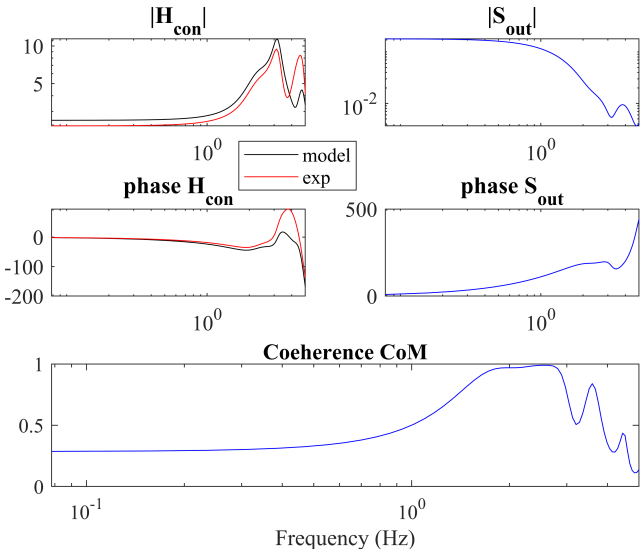

Figure 7.32: Magnitude and phase of controller dynamics H_{con} (left) and of output sensitivity function S_{out} (right) for single link inverted pendulum, subject 11. Coherence function is shown at bottom.

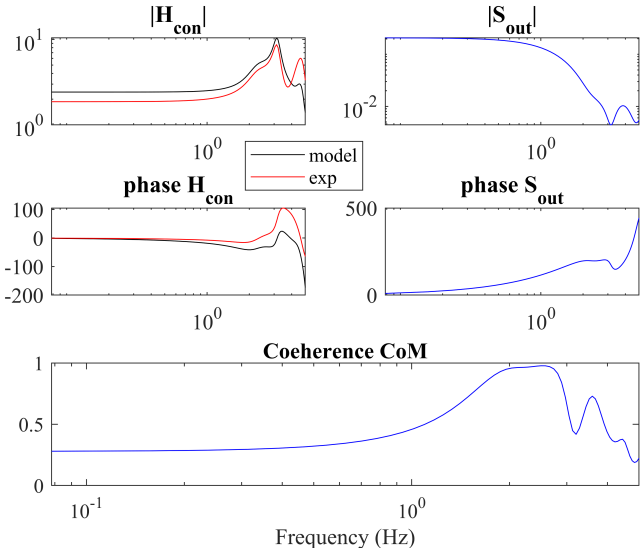

Figure 7.33: Magnitude and phase of controller dynamics H_{con} (left) and of output sensitivity function S_{out} (right) for single link inverted pendulum, subject 12. Coherence function is shown at bottom.

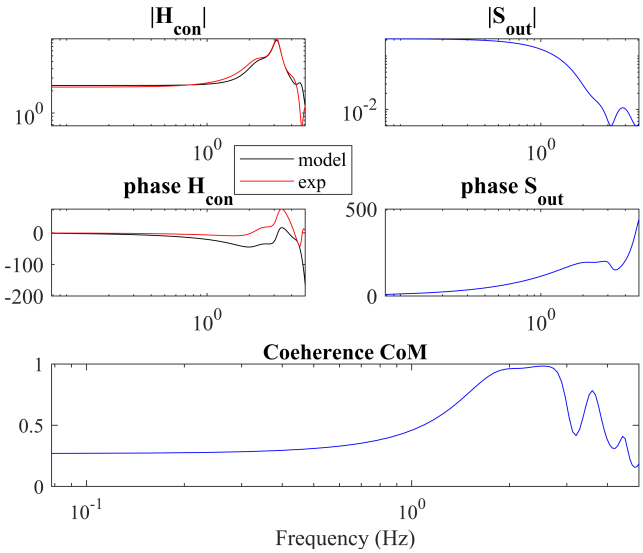

Figure 7.34: Magnitude and phase of controller dynamics H_{con} (left) and of output sensitivity function S_{out} (right) for single link inverted pendulum, subject 15. Coherence function is shown at bottom.

Double link inverted pendulum

The model was firstly tuned with active controller parameters reported in Table 7.2, then the results of simulations and experimental trials were processed by the methodology presented in the previous section. The results for the same subject considered in Figs. 7.25 - 7.29 are reported in Figs. 7.35 to 7.39.

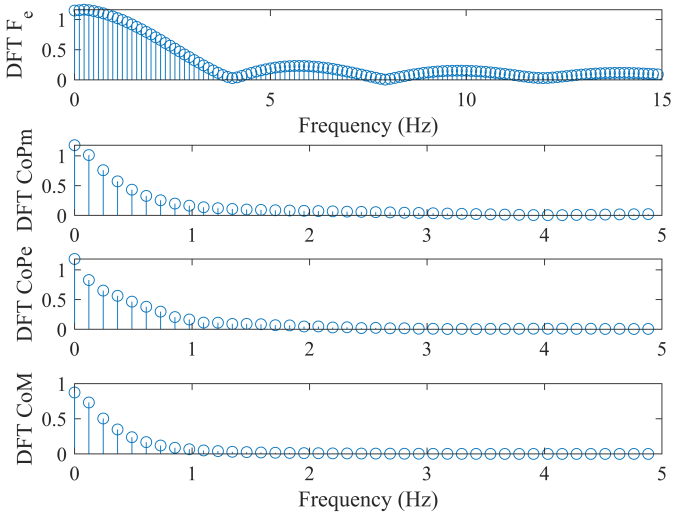

Figure 7.35: Discrete Fourier Transform of signals for double link inverted pendulum model, subject 4. Top to bottom, spectra of perturbation force, modeled CoP $CoPm$, experimental CoP $CoPe$ and CoM.

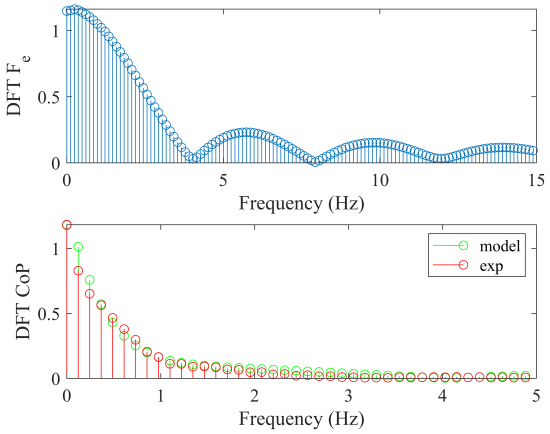

Figure 7.36: Discrete Fourier Transform of force perturbation (top) and of CoP displacement (bottom), double link inverted pendulum model, subject 4.

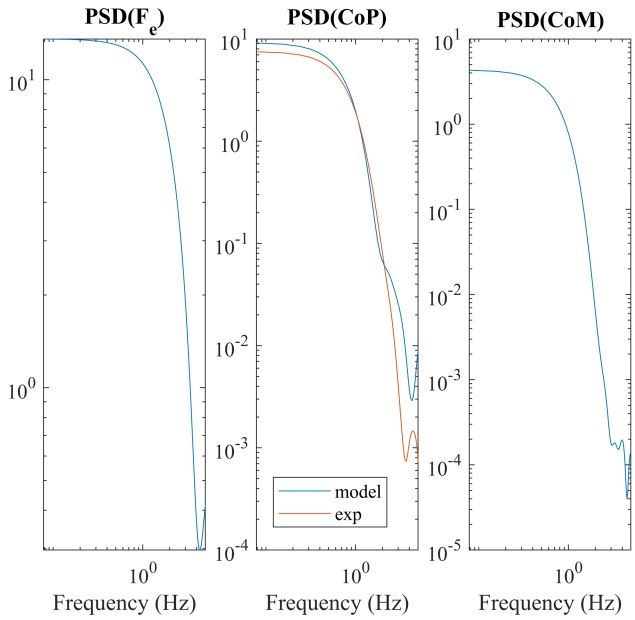

Figure 7.37: Power spectral density of force perturbation (left), CoP displacement (center) and CoM displacement (right), double link inverted pendulum model, subject 4.

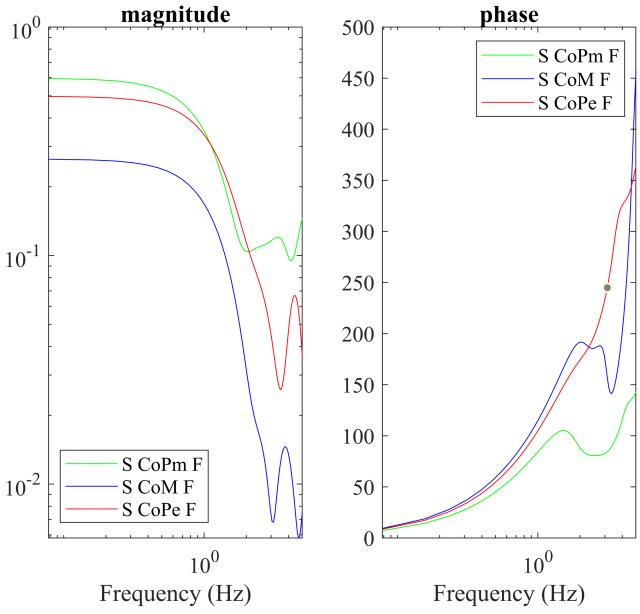

Figure 7.38: Magnitude (left) and phase (right) of input S_{in} and output S_{out} sensitivity functions to external perturbation, double link inverted pendulum model, subject 4.

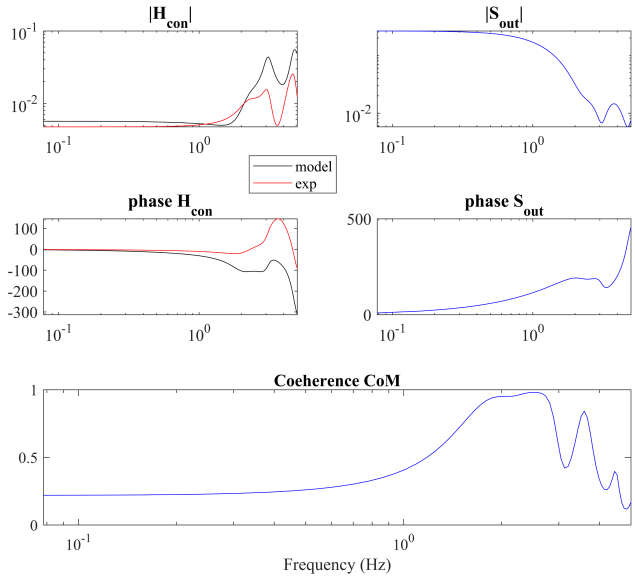

Figure 7.39: Magnitude and phase of controller dynamics H_{con} (left) and of output sensitivity function S_{out} (right) for double link inverted pendulum model, subject 4, by considering CoP displacement as input. Coherence function is shown at bottom.

As highlighted in Figs. 7.38 and 7.39, matching between sensitivity functions, as well control dynamics FRF, obtained from model and experimental data was significantly lower than the one observed for the simpler inverted pendulum model. Same lack of accuracy was anticipated by fit of model CoP displacement to measurement data (see section 7.1.3) that was related to an increase in sum of squares of residuals (Table 7.2) if compared to the single link model (Table 7.1). Similar results were obtained for other subjects (an example in Figs. 7.40 and 7.41). In all situations, the single model fit experimental data with higher accuracy if compared to the double link model.

For the double link model, since two outputs (θ_1 and θ_2) and two inputs (τ_1 and τ_2) are available, different output and input sensitivity functions could be evaluated, as well as neuromuscular controller FRFs [39]. Sensitivity functions' magnitude and phase are presented in Figs. 7.42 and 7.43, whereas Figs. 7.44 and 7.45 show magnitude and phase of controller dynamics FRFs. These functions allow for evaluating individually the sensitivity of rotation or torque at a joint to the external perturbation.

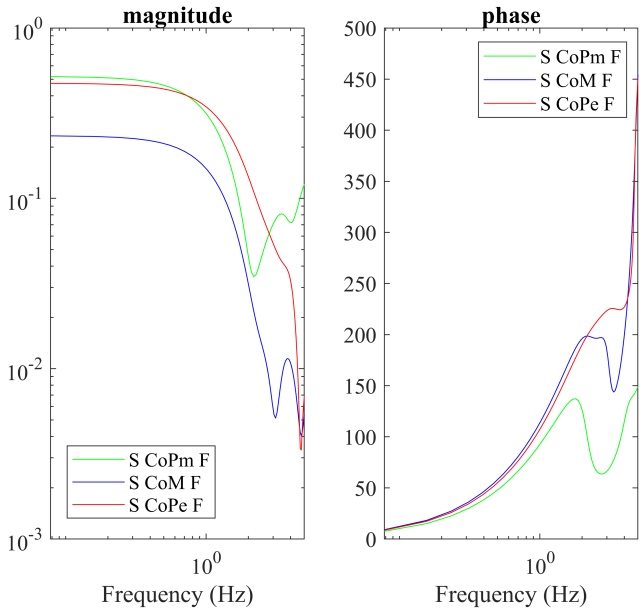

Figure 7.40: Magnitude (left) and phase (right) of input S_{in} and output S_{out} sensitivity functions to external perturbation, double link inverted pendulum model, subject 7.

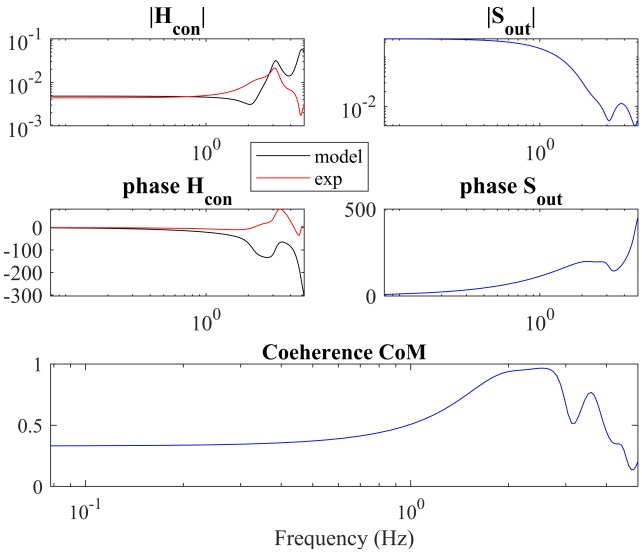

Figure 7.41: Magnitude and phase of controller dynamics H_{con} (left) and of output sensitivity function S_{out} (right) for double link inverted pendulum model, subject 7, by considering CoP displacement as input. Coherence function is shown at bottom.

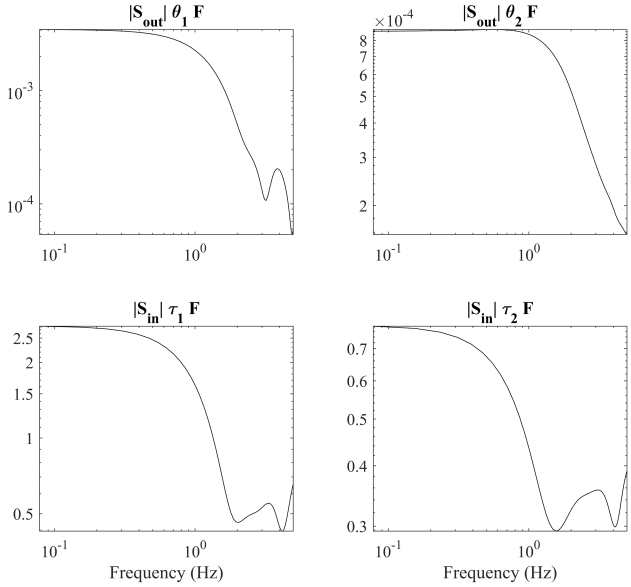

Figure 7.42: Magnitude of individual output (top) and input (bottom) sensitivity functions S_{out} for double link inverted pendulum model.

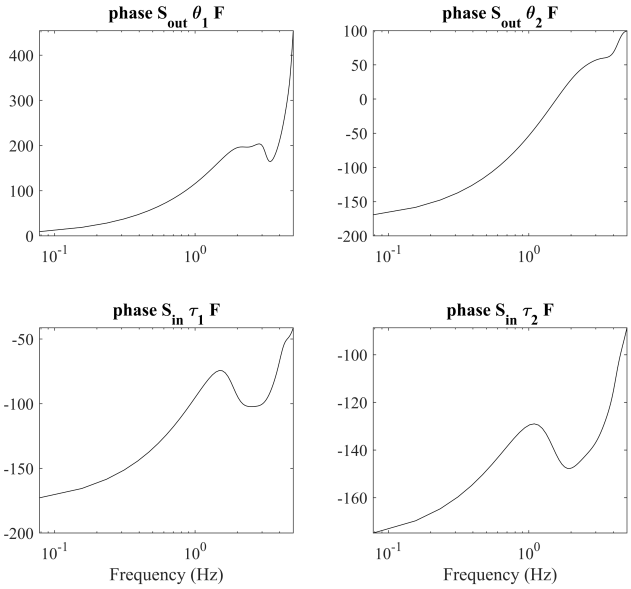

Figure 7.43: Phase of individual output (top) and input (bottom) sensitivity functions S_{out} for double link inverted pendulum model.

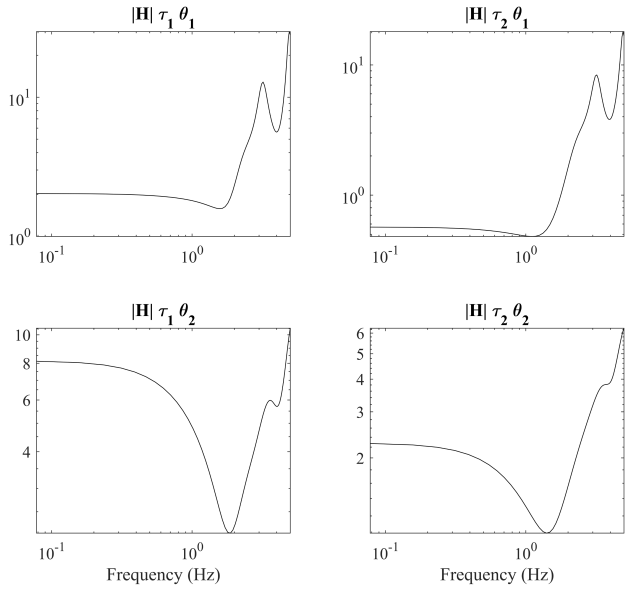

Figure 7.44: Magnitude of individual neuromuscular controller functions H for double link inverted pendulum model.

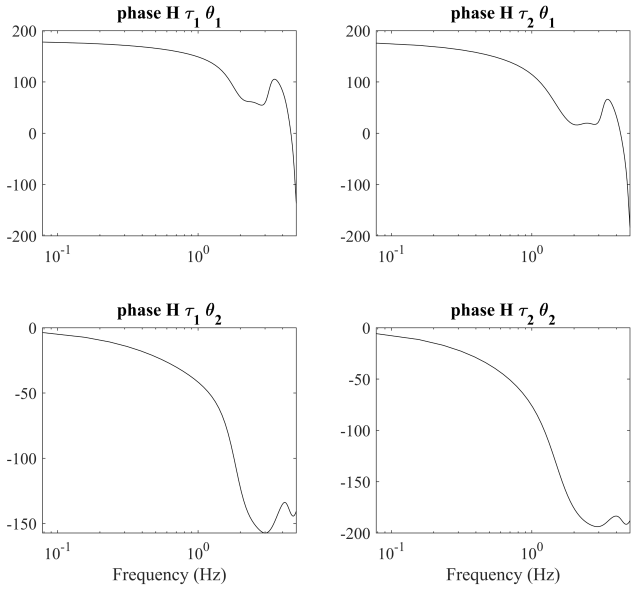

Figure 7.45: Phase of individual neuromuscular controller functions H for double link inverted pendulum model.

Discussion

The simulations confirmed that multi-link models require more refined techniques for system's identification, as pointed out in section 7.1.3. For instance, additional measurements about the state of the system could help in the accurate selection of postural control parameters that are required to run the models. Some Authors discuss the necessity for multiple perturbations in Multiple-Input Multiple-Output (MIMO) systems as a double link inverted pendulum [17, 39] in order to get relevant results. However, other Authors question this observation [34], since it is commonly considered unpractical to exert multiple perturbations at the same time in a clinical environment. Moreover, it should be highlighted that multiple perturbations (e.g. one for each segment considered) are suggested for model identification purposes, that is when experimental FRFs are fitted to models' to find unknown control parameters. In this work, the methodology was instead implemented only to verify model accuracy after tuning, the latter performed directly from CoP displacement data.

Chapter 8

Conclusion

This work focused on the development of an hand-held automatic perturbator (AP) to be implemented in a system for dynamic posturography named PGAS. Posturography is required to objectively assess balance control ability, which is essential to perform any daily activity with efficacy. This clinical evaluation is aimed to elderly people as well as to patients with diseases affecting neuro-muscular control and lower limbs functionality, since both categories of subjects generally suffer from relevant deficiency in postural stability.

In a preliminary analysis carried out with a manual perturbator, an original and significant correlation between the time integral of the impact force (impulse, I) and the entity of the response, in terms of CoP displacement (ΔCoP), was found. This result was confirmed for all the subjects tested, however it was not possible to draw any conclusion with statistical significance due to the difficulty to control the impulse of the force perturbations. For this reason, a first AP prototype based on linear pneumatic actuation was fabricated and tested on healthy subjects to evaluate accuracy and repeatability of the stimuli. In spite of the new architecture based on force feedback, force tracking as well as impulse accuracy were not sufficient for the application. On the other hand, repeatability of the perturbations was significantly improved.

Subsequently, an experimental test-bench that included all the main parts involved in a posturographic task (i.e. the operator, the AP and the patient) was designed in laboratory to evaluate the impact of more refined control techniques on the system's accuracy, as well as to test different pneumatic components with higher performance. This bench was fabricated by means of commercial and custom-made components, and was equipped with appropriate sensors to measure any physical quantity required to the monitoring and control of the system. In addition, a model was developed to support experimental data obtained on the novel test-bench with simulations.

Different control strategies were implemented for both approach (i.e. before impact) and strike (i.e. during impact) phases. As far as the approach phase is

concerned, a closed-loop motion control logic was ultimately chosen, thanks to the implementation of a laser displacement transducer that fed back the actuator's stroke. This solution, that was not available for the first AP prototype due to the lack of a dedicated sensor, increased the repeatability and accuracy of the perturbations regardless of the operator considered to handle the device as well as his or her positioning with respect to the patient. Regarding the strike phase, linear PI and non-linear sliding mode controllers were tested for the regulation of the contact force. Although the latter was theoretically less affected by non-linear phenomena such as friction than the former, PI control allowed for the best performance, especially regarding the responsiveness of the system that was critical for the application (target duration for each stimulus was about 100 - 150 ms). Moreover, the linear controller did not require additional sensors and modeling to provide reliable results that were instead necessary for the sliding mode design.

In addition to the new control logics implemented, different pneumatic components were tested both in the model and experimentally in laboratory. Each combination of the new cylinders and valves was evaluated for stimuli lasting up to 150 ms and with amplitude between 50 and 100 N. Among the several combinations, the architecture based on: (1) an ultra-low friction pneumatic cylinder with metal seals; and (2) fast-responsive and compact flow proportional valves was selected for the development of a final AP prototype. The device has been tested by different operators on a larger sample of healthy subjects (with respect to the preliminary analysis) and showed good impulse accuracy and high repeatability. These trials confirmed the almost linear correlation between CoP displacement and the impulse of the perturbation that was observed in the preliminary study. The ratio between ΔCoP and I, i.e. the normalized CoP displacement ΔCoP_n, should represent an index of postural control stability since it resulted specific for each subject and repeatable among different sessions.

To provide a deeper analysis of balance control system, simple biomechanical models were presented and validated thanks to experimental data obtained during posturographic trials performed with the AP. A methodology for tuning of the models, that is for the identification of unknown parameters related to postural response, was discussed. The results of this analysis, in terms of active (musculoskeletal) response parameters, were comparable with data presented in the literature for similar studies that considered pseudorandom stimuli rather than impulsive ones. Then, techniques for non-parametric identification, based on (closed-loop) linear time-invariant systems theory, were discussed and applied to the study of postural control. In particular, those techniques were implemented to evaluate the conformity in the frequency domain between the simulated postural responses and the ones observed during experimentation. Moreover, they can provide additional insight into such a complex set of mechanisms as the one implemented by Central Nervous System to keep balance.

Limitations and future works

The main limitations of this work consist of: (1) the sub-optimal performance of the final AP prototype in force tracking (during impact); (2) the limited number of subjects tested, hence the difficulty to support the ΔCoP_n parameter as an index of postural control stability with greater statistical and clinical significance; (3) lack of elderly people or real patients tested with the AP.

The accuracy of force tracking during the strike phase was particularly low for the first AP prototype, however it was not optimal even for the final architecture based on high performance valves and actuator. As shown in the previous chapter, this result did not significantly affect the accuracy and repeatability of the impulse, that represented the main focus of the perturbation system given its relationship with the entity of CoP displacement. For this reason, the limited tracking accuracy does not compromise the performance of the perturbation device. Moreover, this study focused in particular on a pneumatic-actuated solution, since it was considered the most appropriate for the application thanks to the limited costs, ease to control and suitability for clean environments. Generally speaking, pneumatic actuation is intrinsically slower than electric or electro-mechanic actuation, and it is also more dependent on non-linear phenomena such as friction, stick-slip effect etc. Future works could investigate new AP architectures based on electric (electro-mechanic) actuation that should theoretically improve the response timing of the system and reduce its bulkiness, since they do not need an external air supply. However, such architectures would require particular attention to the integration of the actuator in an hand-held configuration without exposing the operator to electrical risk. Moreover, the device should always exhibit a good level of maneuverability, hence lightweight actuators must be considered. Finally, the control logic would likely require a redesign since electric servomotors typically control velocity or torque whereas pneumatic linear actuators can regulate the contact force more easily.

Future studies should also focus on the enlargement of the sample of subjects considered, with the aim to improve the understanding of the relationship between the impulse of the perturbations and the entity of the response. In particular, a larger set of subjects would help to find correlations (if any) between ΔCoP_n and characteristics as age, sport habit, anthropometry of the patients. By including elderly people or subjects with neurological disorders, it would be possible to highlight ranges of ΔCoP_n that actually correspond to normal as well as to non-physiological behaviors. Then, the study should aim to find any trend in those parameters to allow for a classification of the level of impairment or to generally assess the ability of a specific subject to keep or to regain balance in perturbed condition.

Bibliography

[1] *Falls*. 2018. URL: https://www.who.int/en/news-room/fact-sheets/detail/falls.

[2] Chen B, Lee YJ, and Aruin AS. "Role of point of application of perturbation in control of vertical posture". In: *Exp Brain Res* 235.11 (2017), pp. 3449–3457.

[3] Colebatch JG, Govender S, and Dennis DL. "Postural responses to anterior and posterior perturbations applied to the upper trunk of standing human subjects". In: *Exp Brain Res* 234 (2016), pp. 367–376.

[4] Diener HC et al. "Stabilization of human posture during induced oscillations of the body". In: *Exp Brain Res* 45.1-2 (1982), pp. 126–132.

[5] Duncan CA et al. "Population Differences in Postural Response Strategy Associated with Exposure to a Novel Continuous Perturbation Stimuli: Would Dancers Have Better Balance on a Boat?" In: *PLoS ONE* 11.11 (2016), e0165735.

[6] Horak FB and Nashner LM. "Central programming of postural movements: adaptation to altered support-surface configurations". In: *J Neurophysiol* 55 (1986), pp. 1369–1381.

[7] van der Kooij H and de Vlugt E. "Postural responses evoked by platform perturbations are dominated by continuous feedback". In: *J Neurophysiol* 98 (2007), pp. 730–743.

[8] Potocanac Z, Golijat R, and Babic J. "A robotic system for delivering novel real-time, movement dependent perturbations". In: *Gait & Posture* 58 (2017), pp. 386–389.

[9] Potocanac Z et al. "Fast online corrections of tripping responses". In: *Exp Brain Res* 232.11 (2014), pp. 3579–3590.

[10] Bieryla KA, Madigan ML, and Nussbaum MA. "Practicing recovery from a simulated trip improves recovery kinematics after an actual trip". In: *Gait & Posture* 26 (2007), pp. 208–213.

[11] Chen B, Lee YJ, and Aruin AS. "Control of grip force and vertical posture while holding an object and being perturbed". In: *Exp Brain Res* 234 (2016), pp. 3193–3201.

[12] Davidson BS et al. "Neural control of posture during small magnitude perturbations: effects of aging and localized muscle fatigue". In: *IEEE Transactions on Biomedical Engineering* 58.6 (2011), pp. 1546–1554.

[13] Ayena JC, Zaibi H, and Ménélas BAJ Otis MJD. "Home-based risk of falling assessment test using a closed-loop balance model". In: *IEEE Transactions on Neural Systems and Rehabilitation Engineering* 24.12 (2016), pp. 1351–1362.

[14] Coelho DB Martinelli AR and et al. "Light touch modulates balance recovery following perturbation: from fast response to stance restabilization". In: *Exp Brain Res* 233.5 (2015), pp. 1399–1408.

[15] Piscitelli D et al. "Anticipatory postural adjustments and anticipatory synergy adjustments: preparing to a postural perturbation with predictable and unpredictable direction". In: *Exp Brain Res* 235.3 (2017), pp. 713–730.

[16] Shahvarpour A et al. "Trunk response to sudden forward perturbations – Effects of preload and sudden load magnitudes, posture and abdominal antagonistic activation". In: *Journal of Electromyography and Kinesiology* 24 (2014), pp. 394–403.

[17] Boonstra TA, Schouten AC, and van der Kooij H. "Identification of the contribution of the ankle and hip joints to multi-segmental balance control". In: *Journal of NeuroEngineering and Rehabilitation* 10:23 (2013).

[18] van der Kooij H and Peterka RJ. "Non-linear stimulus-response behavior of the human stance control system is predicted by optimization of a system with sensory and motor noise". In: *J Comput Neurosci* 30 (2011), pp. 759–778.

[19] Peterka RJ. "Sensorimotor integration in human postural control". In: *J Neurophysiol* 88 (2002), pp. 1097–1118.

[20] Kim j et al. "Human postural control against external force perturbation applied to the high-back". In: *International Journal of Precision Engineering and Manufacturing* 10.4 (2009), pp. 147–151.

[21] Lee YJ, Chen B, and Aruin AS. "Older adults utilize less efficient postural control when performing pushing task". In: *Journal of Electromyography and Kinesiology* 25 (2015), pp. 966–972.

[22] Ruhe A, Fejer R, and Walker B. "The test-retest reliability of centre of pressure measures in bipedal static task conditions - A systematic review of the literature". In: *Gait & Posture* 32 (210), pp. 436–445.

[23] Prieto TE et al. “Measures of postural steadiness: differences between healthy young and elderly adults”. In: *IEEE Transactions on biomedical engineering* 43.9 (1996), pp. 956–966.

[24] Forghani A, Preuss R, and Milner TE. “Short-latency muscle response patterns to multi-directional, unpredictable perturbations to balance applied to the arm are context dependent”. In: *Neuroscience* 352 (2017), pp. 170–179.

[25] Mayagoitia RE et al. “Standing balance evaluation using a triaxial accelerometer”. In: *Gait & Posture* 16 (2002), pp. 55–59.

[26] Kamen G et al. “An accelerometry-based system for the assessment of balance and postural sway”. In: *Gerontology* 44.1 (1998), pp. 40–45.

[27] Moe-Nillsen R and Helbostad JL. “Trunk accelerometry as a measure of balance control during quiet standing”. In: *Gait & Posture* 16 (2002), pp. 60–68.

[28] Henriksen M et al. “Test-retest reliability of trunk accelerometric gait analysis”. In: *Gait & Posture* 19 (2004), pp. 288–297.

[29] Hubble RP et al. “Wearable sensor use for assessing standing balance and walking stability in people with Parkinson’s disease: a systematic review”. In: *PLoS ONE* 10.4 (2015), e0123705.

[30] Winter DA et al. “Stiffness control of balance in quiet standing”. In: *J Neurophysiol* 80.3 (1998), pp. 1211–1221.

[31] Morasso PG et al. “Internal models in the control of posture”. In: *Neural Networks* 12 (1999), pp. 1173–1180.

[32] Park S, Horak FB, and Kuo AD. “Postural feedback responses scale with biomechanical constraints in human standing”. In: *Exp Brain Res* 154 (2004), pp. 417–427.

[33] Koozekanani SH et al. “On the role of dynamics models in quantitative posturography”. In: *IEEE Transactions on Biomedical Engineering* BME-27.10 (1980), pp. 605–609.

[34] Goodworth AD and Peterka RJ. “Identifying mechanisms of stance control: a single stimulus multiple output model-fit approach”. In: *Journal of Neuroscience Methods* 296 (2018), pp. 44–56.

[35] van der Kooij H et al. “A multisensory integration model of human stance control”. In: *Biological Cybernetics* 80 (1999), pp. 299–308.

[36] van der Kooij H et al. “An adaptive model of sensory integration in a dynamic environment applied to human stance control”. In: *Biological Cybernetics* 84 (2001), pp. 103–115.

[37] Pasma JH et al. “Assessment of the underlying systems involved in standing balance: the additional value of electromyography in system identification and parameter estimation”. In: *Journal of NeuroEngineering and Rehabilitation* 14:97 (2017).

[38] van der Kooij H, van Asseldonk E, and van der Helm FCT. “Comparison of different methods to identify and quantify balance control”. In: *Journal of Neuroscience Methods* 145 (2005), pp. 175–203.

[39] Engelhart D et al. “Comparison of closed-loop system identification techniques to quantify multi-joint human balance control”. In: *Annual Reviews in Control* 41 (2016), pp. 58–70.

[40] Visser JE et al. “The clinical utility of posturography”. In: *Clinical Neurophysiology* 119 (2008), pp. 2424–2436.

[41] Haddadin S, Albu-Schäffer A, and Hirzinger G. “Requirements for safe robots: measurements, analysis and new insights”. In: *The International Journal of Robotics Research* 28.11-12 (2009), pp. 1507–1527.

[42] Heinzmann J and Zelinsky A. “Quantitative safety guarantees for physical human-robot interaction”. In: *The International Journal of Robotics Research* 22.7-8 (2003), pp. 479–504.

[43] Haddadin S et al. “An experimental safety study for stab/puncture and incised wounds”. In: *IEEE Robotics & Automation Magazine* 18.4 (2011), pp. 20–34.

[44] Povse B et al. “A tool for the evaluation of human lower arm injury: approach, experimental validation and application to safe robotics”. In: *Robotica* 34 (2016), pp. 2499–2515.

[45] Yamada Y et al. “Human-robot contact in the safeguarding space”. In: *IEEE/ASME Transactions on Mechatronics* 2.4 (1997), pp. 230–236.

[46] Haddadin S et al. “On making robots undestand safety: embedding injury knowledge into control”. In: *The International Journal of Robotics Research* 31.13 (2012), pp. 1578–1602.

[47] Najmaei N and Kermani MR. “Applications of artificial intelligence in safe human-robot interactions”. In: *IEEE Transactions on Systems, Man, and Cybernetics - Part B: Cybernetics* 41.2 (2011), pp. 448–459.

[48] Erden MS and Tomiyama T. “Human-intent detection and physically interactive control of a robot without force sensors”. In: *IEEE Transactions on Robotics* 26.2 (2010), pp. 370–382.

[49] Cherubini A et al. “Collaborative manufacturing with physical human-robot interaction”. In: *Robotics and Computer-Integrated Manufacturing* 40 (2016), pp. 1–13.

[50] Gosselin C et al. “A friendly beast of burden: a human-assistive robot for handling large payloads”. In: *IEEE Robotics & Automation Magazine* 20.4 (2013), pp. 139–147.

[51] Heidingsfeld M et al. “A force-controlled human-assistive robot for laparoscopic surgery”. In: *2014 IEEE International Conference on Systems, Man, and Cybernetics (SMC), San Diego, CA* (2014), pp. 3435–3439.

[52] Tagliamonte NL et al. “Effects of impedance reduction of a robot for wrist rehabilitation on human motor strategies in healthy subjects during pointing tasks”. In: *Advanced Robotics* 25.5 (2011), pp. 537–562.

[53] Riener R, Lünenburger L, and Colombo G. “Human-centered robotics applied to gait training and assessment”. In: *Journal of Rehabilitation Research & Development* 43.5 (2006), pp. 679–694.

[54] Zhang J, Cheah CC, and Collins SH. “Stable human-robot interaction control for upper-limb rehabilitation robotics”. In: *2013 IEEE International Conference on Robotics and Automation, Karlsruhe* (2013), pp. 2201–2206.

[55] Chiaverini S and Sciavicco L. “The parallel approach to force/position control of robotic manipulators”. In: *IEEE Transactions on Robotics and Automation* 9.4 (1993), pp. 361–373.

[56] Madani M and Moallem M. “Hybrid position/force control of a flexible parallel manipulator”. In: *Journal of the Franklin Institute* 348 (2011), pp. 999–1012.

[57] Barjuei ES. “Hybrid position/force control of a spatial compliant mechanism”. In: *International Journal of Automotive and Mechanical Engineering* 14.3 (2017), pp. 4531–4541.

[58] Keemink AQL, van der Kooij H, and Stienen AHA. “Admittance control for physical human-robot interaction”. In: *The International Journal of Robotics Research* 37.11 (2018), pp. 1421–1444.

[59] Richardson R et al. “Impedance control for a pneumatic robot-based around pole-placement, joint space controllers”. In: *Control Engineering Practice* 13 (2005), pp. 291–303.

[60] Guang H et al. “Dynamic modeling and interactive performance of PARM: a parallel upper-limb rehabilitation robot using impedance control for patients after stroke”. In: *J Healthc Eng* 2018:8647591 (2018), pp. 291–303.

[61] Lopes AM and Almeida FG. “Force–impedance control of a six-dof parallel manipulator”. In: *Intelligent Engineering Systems and Computational Cybernetics*. Springer, Dordrecht, 2009.

[62] Anderson RJ and Spong MW. "Hybrid impedance control of robotic manipulators". In: *IEEE Journal of Robotics and Automation* 4.5 (1988), pp. 549–556.

[63] Oh S, Woo H, and Kong K. "Frequency-shaped impedance control for safe human-robot interaction in reference tracking application". In: *IEEE/ASME Transactions on Mechatronics* 19.6 (2014), pp. 1907–1916.

[64] Faudzi AAM, Mustafa ND, and Osman K. "A high performance pneumatic force actuator system: part II - nonlinear controller design". In: *Mathematical Problems in Engineering* 2014, Article ID 261829 (2014).

[65] Slotine JJ and Sastry SS. "Tracking control of non-linear systems using sliding surfaces, with application to robot manipulators". In: *International Journal of Control* 38.2 (1983), pp. 465–492.

[66] Toedtheide A, Lilge T, and Haddadin S. "Antagonistic impedance control for pneumatically actuated robot joints". In: *IEEE Robotics and Automation Letters* 1.1 (2016), pp. 161–168.

[67] Richer E and Hurmuzlu Y. "A high performance pneumatic force actuator system: part II - nonlinear controller design". In: *Journal of Dynamic Systems, Measurement and Control* 122.3 (2000), pp. 426–434.

[68] Zhu Y and Barth EJ. "Impedance control of a pneumatic actuator for contact tasks". In: *Proceedings of the 2005 IEEE International Conference on Robotics and Automation, Barcelona, Spain* (2005), pp. 987–992.

[69] Arbab NH and Najafi F. "Stability and performance of pneumatic actuators in impedance control". In: *Proc IMechE Part I: J Systems and Control Engineering* 228.7 (2014), pp. 476–485.

[70] Driver T and Shen X. "Pressure estimation-based robust force control of pneumatic actuators". In: *International Journal of Fluid Power* 14.1 (2013), pp. 37–45.

[71] Dvir Z et al. "Linearity and repeatability of postural responses in relation to peak force and impulse of manually-delivered perturbations: A preliminary study". In: *European Journal of Applied Physiology* (In press).

[72] Maffiodo D et al. "Pneumo-tronic perturbator for the study of human postural responses". In: *Advances in Intelligent Systems and Computing. Proceedings of the 28th International Conference on Robotics in Alpe-Adria-Danube Region (RAAD 2019)*. Springer Verlag, 2020.

[73] De Benedictis C et al. "L'automazione pneumatica nello studio dell'equilibrio". In: *Oleodinamica Pneumatica* 60.8 (2019), pp. 28–33.

[74] Ferraresi C et al. “Development of an automatic perturbator for dynamic posturographic analysis”. In: *Mechanisms and Machine Science*. Springer Verlag, In press.

[75] Zhivomirov H. *Pink Noise Generation with MATLAB Implementation*. 2013. URL: https://www.mathworks.com/matlabcentral/answers/uploaded%20files/30636/pinknoise.m.

[76] Engelhart D et al. “Assessment of multi-joint coordination and adaptation in standing balance: a novel device and system identification technique”. In: *IEEE Transactions on Neural Systems and Rehabilitation Engineering* 23.6 (2015), pp. 973–982.

This Ph.D. thesis has been typeset by means of the TEX-system facilities. The typesetting engine was pdfLATEX. The document class was `toptesi`, by Claudio Beccari, with option `tipotesi=scudo`. This class is available in every up-to-date and complete TEX-system installation.